Tactile Sensing Based on Capacitive Sensing and Electrical Resistance Tomography

A thesis submitted to The University of Manchester for the degree of

Doctor of Philosophy

in the Faculty of Science and Engineering

2022

Haoyu Zhao

School of Engineering
Department of Electrical and Electronic Engineering

TABLE OF CONTENTS

LIST OF FIGURES

LIST OF TABLES

NOMENCLATURE

Abbreviations and Acronyms

2D	2-Dimentional
3D	3-Dimentional
A	Approximate Coefficient
AD	Average Displacement
ADC	Analogue-to-digital converter
AE	Area error
CC	Correlation Coefficient
CDC	Capacitance-to-Digital Converter
CNC	Computerized Numerical Control
CNT	Carbon Nanotube
DWT	Discrete Wavelet Transform
EIT	Electrical Impedance Tomography
ERT	Electrical Resistance Tomography
FEM	Finite Element Method
FPCB	Flexible Printed Circuit Board
GMR	Giant Magneto Resistive
HD, VD and DD	Horizontal, Vertical and Diagonal Detailed Coefficients
IDE	Inter-Digital Electrode
IE	Image Error
LBP	Linear Back Projection
MCU	Microcontroller Unit

MUX	Multiplexer
NW	Nanowire
PDMS	Polydimethylsiloxane
PE	Position Error
PET	Polyethylene terephthalate
PFOCTS	1H, 1H, 2H, 2H-perfluorooctyltrichlorosilane
PI	Polyimide
PVDF	Polyvinylidene fluoride
PSO	Particle Swarm Optimisation
ROI	Region Of Interest
SMB	Coaxial RF connectors (SubMiniature version B)
SNR	Signal-to-Noise Ratio
SPDT	Single-Pole Double-Throw
SPST	Single-Pole Single-Throw
TENG	Triboelectric Nanogenerator
VCCS	Voltage-Controlled Current Source

Symbols

a	Top side length of the truncated pyramid
b	Bottom side length of the truncated pyramid
C_0	Initial capacitance
C_{full}	Full-scale value of capacitance
$C_{i,j}$	Capacitance of the jth measurement in the ith cycle
$\overline{C}_j$	Average capacitance of the jth measurement

C_m	Measured capacitance
C_p	Parasitic capacitance
ΔC	Capacitance change
d	Distance between parallel electrodes
e_k	Voltage residual
F_s	Shear force
F_z	Normal force
h	Effective detection height
k	Number of clusters
N	Number of electrodes
s	Spacing between adjacent electrodes
S^{-1}	Inverse of sensitivity matrix
S^{dev}	Standard deviation of the sensitivity matrix
$S_{n \times m}$	Sensitivity coefficient matrix
S^T	Transpose of sensitivity matrix
T	Thickness of the substrate
$\Delta U_{n\times 1}$	Boundary voltage change
α	Angle of external force
β	Angle of shear force
δ_r	Repeatability error
δ_H	Hysteresis error
ε_0	Permittivity of vacuum
εr	Relative permittivity
η	Electrode metallisation

θ	Angle between the side and bottom of the truncated pyramid
σ	Real conductivity distribution
$\hat{\sigma}$	Reconstructed conductivity distribution
$\Delta\sigma$	Perturbation of conductivity
$\Delta\sigma_{m\times 1}$	Conductivity change
ϕ_i (x, y)	Electric potential distribution at the position (x, y)
∇	Gradient operator

ABSTRACT

Tactile sensors are necessary for intelligent robots to directly interact with the external environment. Similar to the tactile perception of human skin, tactile sensors enable robots to accurately acquire information such as hardness, texture, and sliding, which cannot be achieved through visual sensing. Through the exploration of different sensing mechanisms, various tactile sensors such as capacitive, resistive, piezoelectric, and triboelectric have been developed.

To simulate human touch, not only single-dimensional tactile sensing but also three-dimensional force sensing and large-area tactile sensing are required. This thesis summarises the research background of tactile sensors and analyses the technical difficulties. Based on the principle of planar capacitance, an innovative flexible tactile sensor with high sensitivity, fast response and wide measurement range is developed. The influence of sensor structure parameters on sensor characteristics is investigated using the finite element method, which provides a theoretical foundation for sensor preparation. On this basis, a novel three-dimensional force tactile sensor is proposed. The optimised dielectric layer structure effectively improves shear force sensitivity. Furthermore, the tactile sensor is expanded to an 8×8 array, and the sensor's tactile sensing and proximity sensing performance is evaluated. To address the issue of poor image quality in ERT tactile sensing, this research improves the imaging algorithm by optimising the sensitivity matrix, which increases the precision of pressure distribution mapping and contact target positioning.

DECLARATION

No portion of the work referred to in this thesis has been submitted in support of an application for another degree of qualification of this or any other university or other institution of learning.

COPYRIGHT STATEMENT

ACKNOWLEDGEMENTS

The last four years have been extraordinary in my life. I would like to express my gratitude to those who supported and guided me during my PhD research.

First and foremost, I am honoured to be a student of Professor Wuqiang Yang. I sincerely appreciate his valuable knowledge, patience, guidance, and encouragement. He is a knowledgeable and well-respected scholar who has mentored me in both research and life.

Thanks to my colleagues and friends for their company and support. I would like to express my gratitude to my colleague Dr. Marco A. Rodriguez for his selfless assistance in carrying out the experiments and simulations. Thank you to everyone at the office E47 in SSB who gave me helpful advice and became personal friends.

Finally, I would like to express my appreciation to my parents, Mr. Guohua Zhao and Mrs. Aifang Wang, for their unwavering love, support, and encouragement. I would also like to thank my dear wife Mrs. Chu Lyu, who supported me and gave me confidence during those difficult times. Thanks to my lovely cat Elan, for bringing so many happy moments to my life.

PUBLICATION

[1] Zhao H, & Yang W (2021), Flexible tactile sensing based on electrical resistance tomography and wavelet image fusion, In *2021 IEEE International Conference on Imaging Systems and Techniques (IST)* (pp. 1-6).

Chapter 1 Introduction

1.1 Tactile sensing

With the rapid advancement of intelligence, robots are becoming increasingly involved in various aspects of daily life. The actuators of traditional industrial robots are embedded with control algorithms that allow them to execute commands based on prior knowledge of the known environment. Robots can only work in specific locations to perform repetitive tasks on well-known objects, and their operations may be disrupted by unexpected events. Therefore, a new generation of intelligent robots is expected to be highly adaptable and capable of actively exploring their surroundings and responding to external stimuli (Yang *et al.*, 2018).

It is undeniable that visual sensing is the primary way for autonomous robots to interact with their surroundings (Bartolozzi *et al.*, 2016). However, ambient lighting conditions have a significant impact on visual sensing. The visual system cannot function normally when it is obscured by obstacles, and only partial information is acquired (Silvera-Tawil *et al.*, 2015). In contrast, tactile sensing is more direct and accurate for feature extraction. Tactile sensors enable accurate estimation of normal and shear forces, as well as vibrations caused by sliding, in tasks involving grasping and manipulating objects (Billard and Kragic, 2019). Furthermore, tactile sensing is more than just a supplement to visual sensing because the tactile information it provides to robots is difficult to obtain via visual sensing, such as material, temperature, humidity, and surface texture (Dahiya *et al.*, 2009). In a word, the introduction of tactile sensors can significantly improve the dexterity, stability and reliability of intelligent robots.

Tactile sensing dates back to the 1970s, but research on tactile sensors was limited to determining whether or not an object was touched and measuring the magnitude of the contact force (Howe, 1993).

Robotics advancements in the 1980s accelerated the development of tactile sensors. Real-time manipulation of robotic hands and tactile sensor arrays capable of object recognition have emerged as research hotspots (Harmon, 1982; Hillis, 1982). Additionally, tactile sensors based on various sensing mechanisms were proposed. For instance, Nelson *et al.* (1986) created a tactile sensor based on magneto-resistive detectors to detect the shear component. Begej (1988) developed a finger-structured sensor using high-density optical fibres, and the contact force distribution was represented by a grayscale image.

From the 1990s to the present, the rise of artificial intelligence has increased demand for tactile sensors (Bauer *et al.*, 2014). Innovative breakthroughs in conductive nanomaterials and elastic polymers, as well as improvements in sensor structures, have greatly improved the flexibility, sensitivity and resolution of tactile sensors (Huang *et al.*, 2019). To design a highly sensitive capacitive pressure sensor, Shuai *et al.* (2017) obtained a wrinkled surface by releasing a stretched polydimethylsiloxane (PDMS) substrate and then depositing silver nanowires as electrodes on it. Zhou *et al.* (2019) mixed carbon-based iron particles in PDMS to create a human cilia-like dielectric layer in the presence of magnetic field. The sensitivity of the sensor is increased by 30 times with the micro-structured dielectric layer, and the minimum detectable pressure is as low as 2 Pa.

1.2 Motivation

In recent years, tactile sensors have evolved towards multi-functionality and high integration. Tactile sensors have been used in other fields such as human-computer interaction, intelligent prosthetics, and medical health monitoring (Wang *et al.*, 2018;

Yang *et al.*, 2019). For example, a scalable tactile glove with 548 sensor units integrated was designed. With the collected tactile information, the weight detection and object recognition are realised through neural network (Sundaram *et al.*, 2019). Tee *et al.* (2015) reported a tactile sensing system integrated with organic transistors for tactile feedback in prosthetics. A prosthetic hand with tactile feedback can alleviate the cognitive burden of monitoring limb movement solely through visual sensing. It can even help the disabled regain lost perception and provide significant psychological benefits (Nghiem *et al.*, 2015). Furthermore, wearable tactile sensors attached to clothing or directly wrapped around the body can be used to track human motion or physiological signals in real time (Kumar and Krishnamoorthi, 2021).

Tactile sensing research has made tremendous progress over the last few decades. It is expected that tactile sensors with skin-like perception abilities will play a crucial role in future innovations in robotics, human-computer interaction, and wearable technology. However, the majority of the research to date has been limited to the demonstration of laboratory prototypes, with only a small amount being commercialised. The reason for this is that the structure of human tactile receptors is far more complex than that of tactile sensors (Abraira and Ginty, 2013). Currently, only a few tactile sensors can simulate the human's full tactile sensory capabilities. Although some reported sensors have attained or even surpassed human tactile perception in some parameters, they are typically designed for specific purposes (such as pressure, strain, vibration, and so on), which has significant practical limitations (Chen *et al.*, 2019). As a result, multifunctional tactile sensors capable of sensing multiple stimuli are desperately needed.

High sensitivity and high spatial resolution are the two most important tactile sensor parameters for obtaining comprehensive tactile information. Microfabrication of micro-structures has proven to be an effective method for realising high-sensitivity tactile

sensors (Saccomandi *et al.*, 2014). High sensitivity tactile sensors, however, rarely have a wide measurement range, which makes the sensor saturated with very little pressure. Additionally, the high cost and complicated manufacturing process for micro-structures limit the mass production of sensors. Therefore, the structural design and fabrication method of the sensor need to be further optimised and improved.

For large-area tactile sensing applications, extending from a single tactile sensor to an array of tactile sensors is not as simple as imagined, because the signal crosstalk between sensing units is unavoidable (Chen *et al.*, 2018). Moreover, numerous connecting wires not only affects the flexibility and reliability of the sensor, but also increases power consumption and maintenance costs. Electrical resistance tomography (ERT) is a novel solution for realising flexible tactile sensing (Silvera-Tawil *et al.*, 2012). It can be a promising option for large-area tactile sensing because it only needs a few electrodes and related wires to gather tactile data. Currently, studies have demonstrated the feasibility of ERT for tactile sensing, but the reconstructed images of tactile distribution are unsatisfactory, and there is a trade-off between image quality and imaging time.

1.3 Aims and objectives

The aim of this research is to adopt new methods and technologies to develop tactile sensors for intelligent robots, human-computer interaction, and other application scenarios, which have significant advantages over traditional methods. The specific research objectives are:

To enhance tactile sensing performance through sensor structure optimisation, and to conduct experiments to confirm the method's applicability and efficacy.

To simplify the fabrication method in accordance with the structural characteristics and application scenarios of the sensor while maintaining sensor performance.

To investigate and demonstrate the performance of planar capacitive sensing in applications such as multi-directional tactile sensing, tactile array sensing, and proximity sensing.

To optimise the ERT imaging algorithm with the goal of accurately locating the target's contact position and improving the spatial resolution of the pressure distribution.

1.4 Novel contributions

The novelty of this thesis can be summarised in the following aspects:

Different from the traditional parallel electrodes structure, a novel design of planar capacitive tactile sensor with inverted pyramid microstructure dielectric layer is proposed. The finite element method is used to quantify the influence of the sensor structure on the sensor performance, which is the basis for the selection of the sensor structure parameters. To achieve adjustable sensitivity and measurement range, microstructures with different sizes are used. In addition to high sensitivity and wide measurement range, the sensor also performs well in dynamic response, stability and durability.

In order to realise multi-directional tactile sensing, the electrode design with three interdigital is proposed for the first time, which is a case of using the minimum number of electrodes. In addition, the micro-structure layout of the dielectric layer has been specifically designed to enhance the sensitivity to shear force.

A Y-shaped contact layer is designed for distributed tactile sensor array, which solves the problem of difficult alignment of each layer. In terms of sensor preparation, the method of combining 3D printing and CNC machining is used to prepare the required mould,

which is more cost-effective, efficient and environmentally friendly than traditional methods (lithography, etching). By simply configuring electrodes, tactile sensing and far/near proximity sensing can be realised on the same sensor.

In order to improve the imaging quality of ERT tactile sensor, a new sensitivity matrix pre-processing method is adopted. Image fusion based on discrete wavelet transform is used to combine the characteristics of different images to obtain more accurate images. In addition, k-means clustering algorithm is used to detect the location of contact targets. In the case of serious distortion of the reconstructed image, this method can still accurately extract the position information of the target. On this basis, edge detection algorithm and particle swarm optimisation algorithm are used to estimate the shape of the target.

1.5 Outline

This chapter introduces the motivation, aims and objectives, and contributions of this research, followed by the thesis outline.

Chapter 2 provides an overview of the relevant background of tactile sensors. The existing mainstream technologies for tactile sensing are reviewed and classified based on different transduction mechanisms. The novelty of ERT-based tactile sensing over traditional techniques, as well as the most recent research, are also presented.

In Chapter 3, a capacitive tactile sensor based on planar electrodes is introduced. Tuneable sensitivity and measurement range are achieved by using different sizes of inverted pyramid micro-structure dielectric layers. Through experiments, the designed sensor's dynamic response, repeatability, and durability are assessed.

Chapter 4 introduces the novel electrode design for multidirectional tactile sensing. The sensitivity in the shear direction is increased by the optimised micro-structure. A general

fabrication process for flexible tactile sensors is provided. Finally, a three-dimensional force loading platform is built to characterise the sensor's performance.

Chapter 5 extends the previous single tactile sensor to an 8×8 array. The quantitative analysis of the relationship between the sensor performance and the geometric parameters is performed using finite element simulation. To solve the problem of difficult alignment of conventional contact layers, a contact layer with a Y-shaped structure is proposed. A multi-channel capacitance measurement system is designed to evaluate the sensor's tactile and proximity sensing performance.

Chapter 6 describes the advantages and challenges of ERT for tactile sensing. To overcome the disadvantage of poor image quality, the combination of sensitivity matrix normalisation and discrete wavelet transform image fusion is used. A new method for estimating the target location and size is proposed, and the applicability of the proposed algorithm to different pressure distributions is demonstrated through simulation and experiments.

Chapter 7 summarises the work accomplished in this research and suggests potential future work.

Chapter 2 Literature review

To improve the performance of tactile sensors, this chapter provides a brief overview of the primary transduction mechanisms of tactile sensors. The characteristics of different types of sensors are compared. As an effective method to improve the sensitivity of the sensor, the microstructure design and fabrication methods of the tactile sensor are emphatically introduced. In addition, the unique advantages of ERT in realising large-area tactile sensing are explained in detail. The factors limiting the practical application and mass production of tactile sensors are analysed. Focusing on the research gap of tactile sensor, the optimisation strategy is proposed from the aspects of sensor structure design, sensor fabrication and imaging algorithm.

2.1 Conventional tactile sensor transduction mechanisms

Taking human skin as an inspiration, researchers have designed various types of tactile sensors. Over the last two decades, tactile sensors have made significant advances in terms of sensitivity, measuring range, and response time (Chi *et al*., 2018; Huang *et al*., 2019). Conventional transduction mechanisms include capacitive, piezoresistive, piezoelectric and triboelectric, while other sensing mechanisms such as optical and electromagnetic are rapidly developing (Pierre-Claver and Zhao, 2021).

2.1.1 Capacitive

Capacitive sensors are one of the commonly used sensors for tactile sensing. A basic capacitive sensor consists of a pair of parallel electrodes with a compressible dielectric material sandwiched between them. The equation for parallel plate capacitance is $C = \frac{\varepsilon_0 \varepsilon_r S}{d}$, where $\boldsymbol{\varepsilon_0}$ is the dielectric constant in the vacuum medium, ε_r is the relative permittivity of the dielectric material, S is the overlapping area of the two electrodes, and d is the

distance between the electrodes. As shown in Figure 2.1, external stimuli applied to the sensor cause changes in d and S, so that the magnitude of normal force and shear force can be obtained according to the change in capacitance. Capacitive sensors are commonly used in consumer electronics due to their simple structure, low power consumption, high sensitivity and large dynamic range (Pierre-Claver and Zhao, 2021). However, capacitive tactile sensors are susceptible to capacitive coupling interference. Therefore, an optimised sensor design and dedicated conditioning circuitry are required to minimise this effect, especially for applications where quantitative and accurate information is desired.

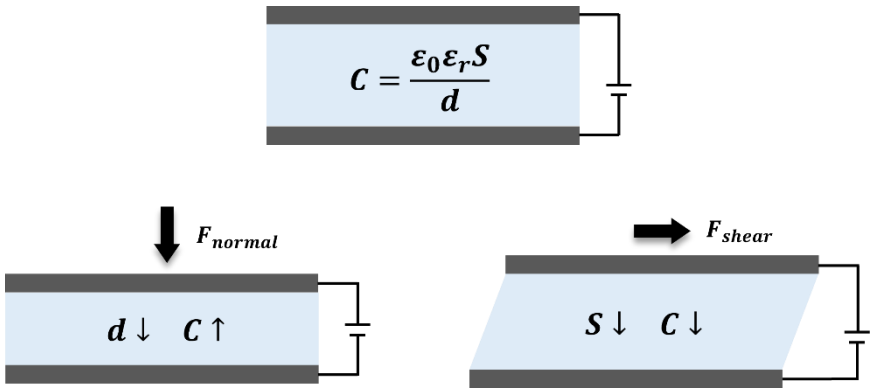

Figure 2.1: Principle of capacitive tactile sensors.

Considerable efforts have been devoted to the modification of dielectric materials to improve the performance of capacitive sensors. Increasing the relative permittivity ε_r of elastomeric composites has been successfully applied to improve the sensitivity (Wang *et al.*, 2015). This can be achieved by doping conductive fillers such as silver nanowires near the percolation threshold (Shi *et al.*, 2018). Qiu *et al.* (2019) dip-coated a mixture of various fillers on polyurethane sponge to obtain a porous dielectric material with both high relative permittivity and excellent elastic properties. The prepared tactile sensor exhibits fast response time (~45 ms) and excellent sensitivity (~0.062 kPa^{-1}).

Optimising the mechanical properties of the dielectric layer is also an effective way to improve sensitivity. In addition to improving the sensitivity of capacitive tactile sensors, micro-structuring the dielectric layer can reduce its viscoelasticity, reducing response and relaxation times (Tee *et al.*, 2014). Pyramids, cylinders, and microporous structures are common microstructures used to improve the mechanical properties of dielectric layers (Hammock *et al.*, 2013). For example, Fang *et al.* (2020) designed a micro-needle structure on the surface of the dielectric layer, which mimics the Merkel cells of human fingertips. The improved dielectric layer greatly increases the sensitivity and detection range of the sensor.

2.1.2 Piezoresistive

Piezoresistive sensors have been widely studied and applied in the fields of tactile sensing and electronic skin due to their simple structure. The piezoresistive tactile sensor is based on the resistance change caused by the deformation of the piezoresistive material (Jason *et al.*, 2017). Piezoresistive materials are prepared by filling elastic polymers (e.g., Ecoflex and PDMS) with conductive particles such as carbon nanotubes (CNTs) (Cai *et al.*, 2020), silver nanowires (Liu *et al.*, 2018), graphene (Liu *et al.*, 2017) and carbon black (Zhai *et al.*, 2020). In addition to composite materials, Gao *et al.* (2017) injected liquid metal into PDMS micro-channels and designed a wearable pressure sensor through integrated Wheatstone circuits. This research provides new insights into the development of ultra-high sensitivity piezoresistive tactile sensors.

Piezoresistive tactile sensors are classified into two types based on the principle of resistance change: those based on the piezoresistive effect of materials and those based on surface contact resistance. The piezoresistive effect of the material results from the reduction of the gap between the conductive particles inside the material when subjected

to external force, forming more conductive paths and lowering the resistivity of the material. Figure 2.1 (a) shows an illustration of this process. The surface contact resistance between the electrodes and the piezoresistive material varies with applied pressure, as shown in Figure 2.1 (b). At low pressure, surface contact resistance is dominant. The piezoresistive effect predominates when the pressure rises to a level at which the contact area between the electrode and the piezoresistive material no longer increases (Weiss and Worn, 2005). As a result, the addition of micro/nanostructures to the surface of piezoresistive materials can significantly improve sensor sensitivity.

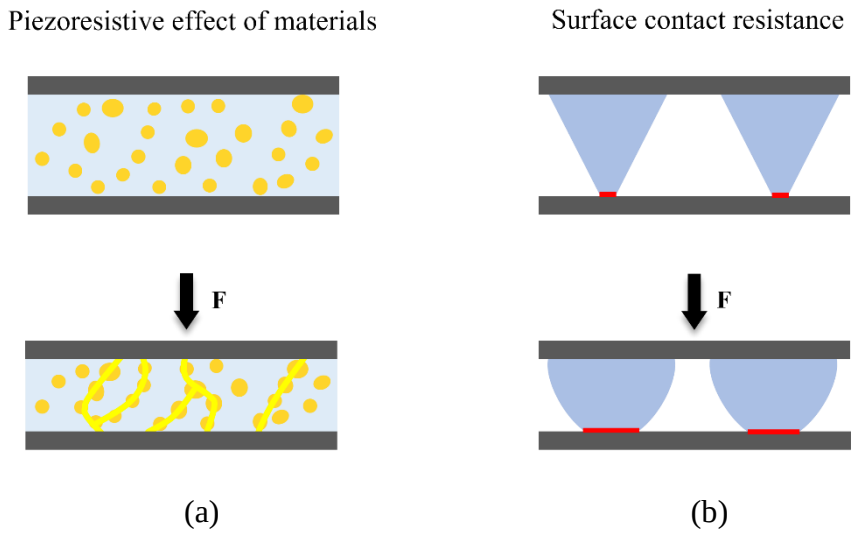

Figure 2.2: Principle of piezoresistive tactile sensors based on (a) piezoresistive effect of materials and (b) surface contact resistance.

Inspired by human skin, Park *et al.* (2014) employ piezoresistive materials with interlocking structures to enhance sensor performance. They prepared two CNT/PDMS films of micro-dome structure arrays using a silicon mould as a template and interlocked the two films. When the sensor is subjected to external pressure, the contact resistance is significantly reduced due to the increased contact area between the interlocking micro-domes, resulting in extremely high sensitivity. Furthermore, the multilayer interlocking structure array was shown to have extremely high sensitivity and linear response over a wide pressure range (Lee *et al.*, 2018). Moreover, nanostructure arrays are also used to

design high-performance tactile sensors. For instance, Ha *et al.* (2015) fabricated hierarchical ZnO Nanowire (NWs) arrays on the surface of PDMS micropillar arrays, and the sensors are capable of detecting extremely small static pressure (0.6 Pa) as well as dynamic stimuli such as tiny vibrations and sound stimuli.

The benefits of the piezoresistive tactile sensor include low fabrication costs, high sensitivity and simple signal conditioning circuit. However, after compression, the material takes a long time to return to its original shape. Piezoresistive sensors are also susceptible to undesired drift and temperature variations.

2.1.3 Piezoelectric

The principle of piezoelectric tactile sensors is based on the intrinsic piezoelectric effect of materials, as shown in Figure 2.3. When the piezoelectric material is mechanically stimulated, polarisation occurs, resulting in opposite charges on the two surfaces. The charge vanishes when the mechanical stimulus is removed. The generated charge is proportional to the force applied to the sensor, and the amount of charge is collected by an external circuit to determine the magnitude of the force.

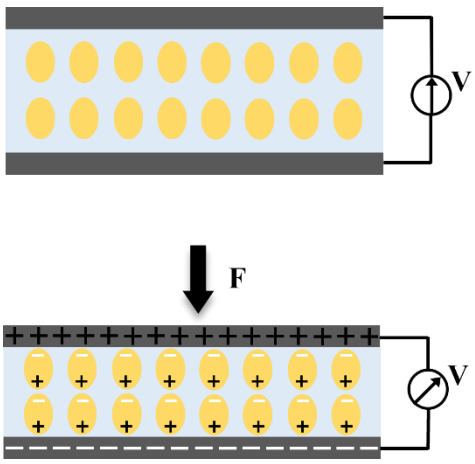

Figure 2.3: Principle of piezoelectric tactile sensors.

As the most used piezoelectric material, polyvinylidene fluoride (PVDF) is widely used due to its flexibility and ease of fabrication compared with piezoceramics (Zhu *et al.*,

2020). To improve the piezoelectric coefficient of PVDF, Jiang *et al.* (2020) added $BaTiO_3$ nanoparticles to the PVDF substrate by electrospinning, and the piezoelectric performance and flexibility of the prepared composite material were greatly improved.

Among these sensing mechanisms, piezoelectric sensors have excellent sensitivity to high-frequency dynamic mechanical stimuli, which have similar transient sensing capabilities to rapidly adapting receptors in human skin (Ramadan *et al.*, 2014). For example, a PVDF sensor embedded in a robotic finger achieves a temporal resolution as high as 2.5 kHz, which is much higher than the limit of human tactile receptors (~400 Hz) (Jamali and Sammut, 2010). Therefore, piezoelectric sensors were used in vibration-related applications such as slip detection (Shirafuji and Hosoda, 2014) and texture recognition (Luo *et al.*, 2017). In addition, piezoelectric sensors are self-powered, i.e. mechanical energy is converted into electrical energy, so no external power supply is required. However, the difficulty in detecting static pressure and the temperature-sensitive properties of piezoelectric materials remain the most significant factors limiting the use of piezoelectric tactile sensors. (Hammock *et al.*, 2013).

2.1.4 Triboelectric

Triboelectric tactile sensors, like piezoelectric sensors, have the advantage of self-powering and are known as triboelectric nanogenerators (TENGs) (Wang, 2020). Triboelectric sensors work on the principles of electrification and electrostatic induction to convert external mechanical stimuli such as pressure and friction into electrical signals (Fan *et al.*, 2014). Figure 2.4 demonstrate the two most common forms of triboelectric sensors, i.e. vertical contact-separation mode and lateral-sliding mode. Note that the red and blue in the figure represent two different materials. Using the former as an example, due to the different electron affinities of the two materials, the two layers absorb equal

amounts of positive and negative charges during friction. Following separation, an induced potential is generated, which converts the mechanical force into an electrical signal (Wu *et al.*, 2019).

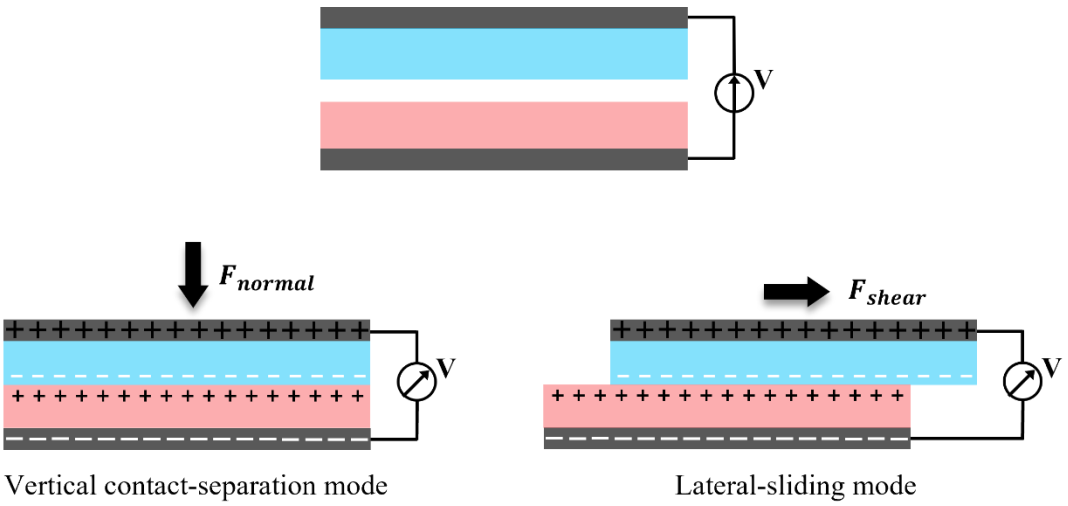

Figure 2.4: Principle of triboelectric tactile sensors.

The generation of TENG has promoted the development of flexible sensors while also providing a new solution for tactile sensing. Lin *et al.* (2013) reported a triboelectric effect-based sensor array for static pressure sensing in addition to dynamic pressure sensing. Furthermore, the sensitivity and measurement range of TENG-based sensors can be enhanced or tuned by modifying the material surface structure. For example, Ren *et al.* (2018) developed a fully elastic tactile sensor with tiny burr arrays that can detect normal force and shear force from different directions. To increase contact friction, Yao *et al.* (2020) created friction layers with interlocking structures by replicating the microstructure of a natural plant surface. When compared to piezoelectric sensors, the materials available for triboelectric sensors are more diverse, because triboelectrification can be generated by different materials or even the same materials with different structures.

2.1.5 Other mechanisms

In addition to the four tactile detecting techniques mentioned above, optical, magnetic, and acoustic tactile sensors have recently been created. In most cases, tactile sensing is accomplished by indirectly assessing changes in physical quantities generated by external forces. For example, Ly *et al.* (2017) designed a surgical grasper with tactile sensing function based on acoustic reflection. The magnitude of the grasping force was obtained by analysing the received synthetic wave. Likewise, optical tactile sensors use light reflected from elastomers to detect touch by determining its angle, wavelength, or brightness (Chen *et al.*, 2017). Furthermore, Yamazaki *et al.* (2016) proposed a photoelectric tactile sensor for object identification that detects external force in the form of light propagation loss in a deformed optical fibre. However, this type of sensor requires both light generator and terminal detector, which consumes a lot of power for large-area tactile sensors. Sferrazza and D'Andrea (2022) proposed a vision-based high-resolution tactile sensor. The movement of particles in the flexible material is captured by the camera integrated inside the sensor, and the contact force information is calculated by visual image processing technology. High resolution and tolerance to electromagnetic interference are two advantages of optical tactile sensors. However, its performance is strongly dependent on elastomer design, and the sensor's production and hardware expenses are rather high.

Magnetic sensors achieve tactile sense by measuring magnetic field changes in response to external force. Using iron nanowires combined with PDMS, Alfadhel and Kosel (2015) created a high-sensitivity ciliary tactile sensor. The magnetic field varies as the cilia bends under external force. Tactile sensing is accomplished by monitoring changes in the magnetic field with a multilayer giant magneto resistive (GMR) sensor. In recent years, tactile sensors based on magnetostrictive inverse effect have also been developed, which

have simple structure and rapid response (Li *et al.*, 2018). The use of such sensors for tactile sensing is however constrained by the peculiarities of magnetic materials.

2.2 Micro-structure design of capacitive sensor

In addition to the innovative development of new materials, high-performance tactile sensors can also be prepared through the design of micro-structures. Micro-structuring the dielectric layer or electrodes of capacitive sensors allows the sensor to be compressed more easily, enhancing the sensor's sensitivity (Zhang *et al.*, 2019). Additionally, adding microstructures to the dielectric layer helps lessen hysteresis brought on by the material's viscoelasticity (Tee *et al.*, 2014). By using a photolithographic template, Luo *et al.* (2019) created a PDMS dielectric layer containing an array of tilted micro-pillars. Tilted micropillars can create greater deformation than vertical micropillars, and the sensitivity of the sensor is increased by more than 600 times. Similar to this, Li *et al.* (2017) developed a bendable and sliding triboelectric sensor with fish-scale-like micro-structures, increasing the device's friction interface area and enhancing the triboelectric effect. It outperforms sensors with vertical micro-structures.

The fabrication of above high-sensitivity sensors usually involves complex processes, including metal deposition, photolithography, etching, *etc*. These traditional technologies are not environmentally friendly and are costly, limiting the mass manufacture and commercialisation of tactile sensors. Moreover, the micro-structures fabricated by photolithography and etching are limited to regular geometries, such as cylinders, pyramids and truncated pyramids (Yang *et al.*, 2019).

Some researchers have been exploring alternative methods of making micro-structures. For example, Kwon *et al.* (2016) mixed sugar particles into Ecoflex and obtained a porous structure dielectric layer by dissolving the sugar particles. Wang *et al.* (2014) fabricated

micropatterned PDMS films using the microscale surface texture of silk as a mould. Many researchers are also employing biomimetic architectures to improve sensor performance. Li *et al.* (2016) used the unique micro-structure on the lotus leaf as an electrode template and polystyrene micro-spheres as a dielectric layer, the sensitivity of the sensor is increased by 20 times. Moreover, the dried rose petals are directly used as the dielectric layer of the capacitive sensor, which provides a new idea for the design of the micro-structure (Wan *et al.*, 2018). Although these strategies greatly reduce the fabrication cost, the consistency of the sensor cannot be guaranteed due to the randomness of the micro-structure.

3D printing allows for the rapid manufacturing of components with high precision and complex geometries, and it is widely employed in industrial and academic applications (Tofail *et al.*, 2018). The use of 3D printing to create flexible sensors has gained popularity in recent years (Liu *et al.*, 2018). For example, a 3D stretchable tactile sensor is directly printed onto an arbitrary curved surface, which can detect pulse and finger motion (Guo *et al.*, 2017). A 3D printing-based mould with regular micro-grooves was used by Zhuo *et al.* (2017) to build dielectric layer micro-structures for capacitive pressure sensors. More applications of 3D printing in flexible sensors are summarised in (Han *et al.*, 2019) and (Khosravani and Reinicke, 2020). Despite the low resolution of existing commercial 3D printers, the low cost and high efficiency of 3D printing technology show tremendous potential in the mass production of sensors.

2.3 3D force tactile sensor

For intelligent robots to complete a variety of complex and delicate tasks, however, the detection of normal force and two-dimensional force distribution is insufficient. This

necessitates tactile sensors with the ability to detect 3D forces in any direction. (Chen *et al*., 2018; Wang *et al*., 2019; Yao *et al*., 2020).

The structural design of the sensor plays a crucial role in realising 3D force detection. Moreover, the majority of the literature employs a sandwich structure with multiple electrode pairs. Lee *et al*. (2011) described a design with four parallel electrodes, in which the normal and shear force components were calculated using the capacitance difference. Zhang *et al*. (2014) proposed a 3D force sensor for fingertips based on quantum tunnelling composites, which consists of four sector-shaped electrodes and a common electrode to achieve dynamic grasping of objects. Liu *et al*. (2017) used the same structure to design a tactile sensor array based on polyvinylidene fluoride (PVDF) for roughness recognition of objects.

For capacitive sensors with parallel electrodes, the detection of 3D force can also be realised by changing the overlapping area of electrodes (Chandra *et al*., 2017). In addition, some studies employed inter-digital electrodes to maximise the variation of the overlapping area, improving the sensitivity of the sensor in the shear direction (Surapaneni *et al*., 2011; Dobrzynska and Gijs, 2012). However, in the case of complex electrode structures, this brings significant challenges to electrode alignment.

Despite its simple structure, this sandwich-structured capacitive tactile sensor is not suitable for applications with high surface curvature or large deformation. A capacitive tactile sensor with planar electrodes was proposed by Huang *et al*. (2017). The sensor consists of one common electrode and four sensing electrodes. 3D force detection is realised by changing the relative permittivity above electrodes. Because all electrical connections are on the same layer, sensor fabrication complexity is reduced, making sensor arrays more feasible.

2.4 Large area tactile sensing based on ERT

A lot of research has been devoted to the design of distributed tactile sensing array in the fields of robotic electronic skin, wearable devices and healthcare monitoring (Wang *et al.*, 2015; Wang *et al.*, 2018; Ramalingame *et al.*, 2019). Those sensor arrays can distinguish the location of multiple contact points and recognise the shape of the object (Hammock *et al.*, 2013). The sensitivity and spatial resolution of the sensors even surpass that of human fingertip skin (Mannsfeld *et al.*, 2010). However, the utilisation of tactile sensor arrays on a big scale is a difficult task. This is because the hardware required to process the signal becomes more sophisticated as the number of sensor units grows. Furthermore, a large number of wires not only introduces electromagnetic noise but also reduces the sensor's durability and flexibility. Therefore, some researchers suggested that human-computer interaction and robot skin may be realised using non-destructive and non-invasive methods.

2.4.1 Working principle

Electrical resistance tomography (ERT) is a simplified form of electrical impedance tomography (EIT). Since only the conductivity distribution in sensitive materials is considered, tactile sensors using this method are generally referred to as ERT tactile sensors. Figure 2.5 shows the ERT-based tactile sensing system. Electric current flows from electrodes on the boundary of variable conductive material (conductive fibre or conductive rubber, etc.). Deformations caused by mechanical forces applied to flexible materials will alter the conductivity distribution. Tactile sensing can be realized in large-area and arbitrary-shaped areas based on boundary electrical signals and image reconstruction algorithms. With unique imaging methods and innovations in flexible conductive materials, ERT sensors have quickly become a promising technology in the

field of tactile sensing.

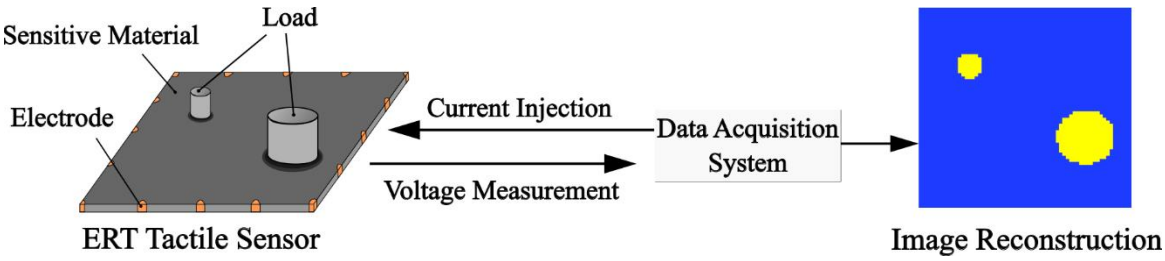

Figure 2.5: Tactile sensing system based on ERT.

ERT can be modelled mathematically in the following discrete form:

$$\Delta U_{n \times 1} = S_{n \times m} \Delta \sigma_{m \times 1} \tag{2.1}$$

where n is the number of independent boundary voltages, and m is the number of pixels in the reconstructed image. $\Delta U_{n\times 1}$ is the change in the voltage before and after the external force is applied. $S_{n\times m}$ is the sensitivity coefficient matrix. $\Delta\sigma_{m\times 1}$ is the change in conductivity.

For an ERT sensor with N electrodes, N(N-3)/2 independent voltages are obtained by adopting the adjacent excitation and measurement strategy. In this work, a 16-electrode square sensor is used, and so a total of 104 boundary voltages are obtained.

The sensitivity matrix $S_{n\times m}$ reflects the sensitivity of the voltage to changes in conductivity of each pixel. The sensitivity between the ith and jth electrode pair at position (x, y) can be calculated by

$$S_{i,j}(x, y) = -\int_{p(x, y)} \frac{\nabla \phi_i(x, y)}{I_i} \cdot \frac{\nabla \phi_j(x, y)}{I_j} \, d\,x\, d\,y \tag{2.2}$$

where ϕ_i (x, y) and ϕ_j(x, y) are the electric potential distribution at the position (x, y) when the ith and jth injection currents are I_i and I_j, respectively. p(x, y)is the finite element to be solved.

The inverse process of ERT is to find conductivity distribution when the sensitivity matrix and boundary voltage are known.

$$\sigma = S^{-1} U \tag{2.3}$$

Unfortunately, the inverse of S does not exist. Thus, the task of image reconstruction is to find an approximate solution of S^{-1}.

The linear back projection (LBP) algorithm is the simplest and the most widely used image reconstruction algorithm (Barber and Seagar, 1987). The idea is to use S^T to approximately replace S^{-1}, as follows.

$$\sigma = S^T U \tag{2.4}$$

The LBP algorithm is often used in real-time applications. However, due to the serious distortion of the reconstructed image, it can only be used for qualitative analysis.

Landweber algorithm is the most representative iterative algorithm (Yang and Peng, 2002). The principle is based on the least squares method, which uses an iterative method to approximate the optimal solution of S^{-1}, which has higher accuracy than S^T. Generally, the LBP algorithm is used to obtain the conductivity distribution σ_0 as the initial value, and the iterative equation is:

$$\hat{\sigma}_{k+1} = \hat{\sigma}_k - \alpha S^T (S \hat{\sigma}_k - U) \tag{2.5}$$

where k is the number of iterations and α is the step length.

To accelerate the convergence of iterations, the step length is updated in each iteration:

$$\hat{\alpha}_k = \frac{\| S^T \hat{e}_{k-1} \|^2}{\| S S^T \hat{e}_{k-1} \|^2} \tag{2.6}$$

Where e_k is the voltage residual, which represents the difference between the actual

$$e_k = S\,\hat{\sigma}_k - U \tag{2.7}$$

voltage and the estimated voltage:

Compared with the LBP algorithm, the image reconstructed by Landweber algorithm has higher quality and clearer contours. However, the pursuit of high resolution comes at the expense of real time performance.

Correlation coefficient and image error are introduced to evaluate the quality of the image (Cui *et al.*, 2016):

$$\text{Correlation coefficient} = \frac{\sum_{i=1}^{N} (\hat{\sigma}_i - \bar{\hat{\sigma}})(\sigma_i - \bar{\sigma})}{\sqrt{\sum_{i=1}^{N} (\hat{\sigma}_i - \bar{\hat{\sigma}})^2 \sum_{i=1}^{N} (\sigma_i - \bar{\sigma})^2}} \tag{2.8}$$

$$\text{Image error} = \frac{\|\hat{\sigma} - \sigma\|}{\|\sigma\|} \times 100\% \tag{2.9}$$

where σ is the real conductivity distribution, $\hat{\sigma}$ is the reconstructed conductivity distribution, $\bar{\sigma}$ and $\bar{\hat{\sigma}}$ are the mean values of σ and $\hat{\sigma}$ respectively. The closer the correlation coefficient of the image is to 1, the stronger the correlation between the reconstructed image and the real distribution, and the higher the quality of the reconstructed image. Basically, the lower image error, the better image quality.

2.4.2 Flexible conductive material

The original idea of applying ERT to tactile sensing was proposed by Fulton and Lipczynski (1993), however, this research was not pursued due to failure to find suitable conductive materials. Kato *et al.* (2007) proposed an ERT sensor based on an easily fabricated conductive rubber and reconstructed the image of the pressure distribution by using the least square method. Nagakubo *et al.* (2007) sprayed a conductive solution on the surface of the fabric as a stretchable conductive material to cover complex faces and movable elbow joints. Compared with conductive rubber, conductive fabric has a wider deformation range and lower time delay, but the large conductivity change in the sensing area leads to poor stability. On this basis, they designed a conductive fabric sensor with a double-layer mesh structure (Alirezaei *et al.*, 2009). Conductivity is varied by contact between conductive fabrics with different conductivity. This reduces the response time and enables the sensor to perform stable pressure measurements even under large stretches. Later, Silvera-Tawil *et al.* (2012) improved the sensor design by adding a layer of polyurethane foam to the bottom layer and covering the top layer with soft suede fabric to make it closer to the touch of human skin. Furthermore, a method using ionic liquids as sensing materials to realise ERT tactile sensing was proposed (Chossat *et al.*, 2015). The microchannel restricts the direction of the injected current with a certain geometric shape, which solves the nonlinear problem to some extent.

2.4.3 Technical difficulties

The poor imaging quality of ERT is the main reason limiting its application. The imaging quality can be improved by increasing the number of electrodes to obtain more measurement data (Tang *et al.*, 2002). Huang *et al.* (2007) reported the method of augmenting the measurement data with rotatable electrodes. However, these methods come at the cost of increasing hardware cost and sacrificing real-time performance.

Optimising electrode excitation and measurement modes is another strategy for improving image quality. Combining different excitation and measurement modes can improve the uniformity of the electric field and obtain diverse measurement data. Adler *et al.* (2011) further improved the adjacent excitation pattern by adjusting the electrode position. Tawil *et al.* (2011) suggested configuring internal electrodes to improve the imaging quality of the central region. However, how to place the internal electrodes and their lead wires needs to be discussed, which also affects the overall flexibility of the sensor.

2.5 Summary

This chapter reviews the recent development of tactile sensors and their applications in different fields. In view of the structure optimisation of capacitive sensor and the application of ERT in tactile sensor, several aspects still need to be improved to promote the practical application of tactile sensor and facilitate mass production.

(1) Although capacitive tactile sensors with micro-structured dielectric layers have high sensitivity and fast response time, the limited measurement range and long recovery time are trade-offs. Quantifying the relation between sensor structure and sensor performance enables the tactile sensor to meet the requirements of practical applications. Finite element method (FEM) has been used to model the shape, size and spacing of dielectric layer micro-structures. However, these relations have been verified by few experiments.

(2) Another consideration for capacitive tactile sensors is that the double-layered structure may result in poor electrical connections when it is deformed, reducing the flexibility of the sensor. Moreover, for high-resolution applications involving multiple sensing units, ensuring the alignment of the upper and lower electrodes is a challenge.

These problems can be avoided by using a single-layer electrode structure. Thus, a robust electrical connection can be established, and the overall flexibility of the sensor can be improved.

(3) To improve the sensitivity of the tactile sensor array, Liang *et al.* (2015) configured a contact structure for each sensing unit to concentrate stress. However, precision instrument is required to assist in the alignment and assembly, which undoubtedly reduces the production efficiency. Therefore, to promote the practical application of the tactile sensor array, the structural design of the sensor should be further improved and optimised.

(4) Due to the limitations of the reconstruction algorithm and the sensitivity of the sensor to hardware noise, the tactile distribution obtained by ERT is severely distorted, specifically manifested by blurred image edges and imprecise position estimation. Therefore, how to improve the quality of reconstructed images is a challenging problem. However, high-precision image reconstruction algorithms inevitably affect the real-time performance, so the combination of image post-processing methods may be able to meet the requirements with a small amount of computation.

Chapter 3 Design and optimisation of planar capacitive tactile sensor

In this chapter, a capacitive tactile sensor with planar electrodes is proposed. To improve the sensitivity of the sensor, the structure of each layer of the sensor is optimised and verified by finite element simulation and experiments. In addition to high sensitivity and high measurement range, the sensor exhibits excellent performance in terms of dynamic response, stability and durability.

3.1 Sensor design

The proposed tactile sensor is made up of three layers: (1) a contact layer, (2) a dielectric layer, and (3) an electrode layer. Figure 3.1 shows the sensor structure.

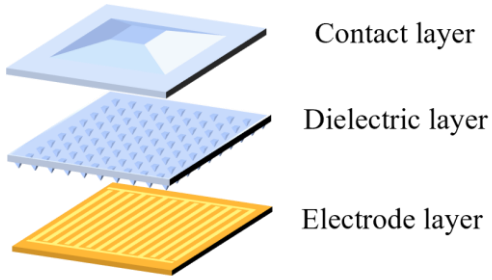

Figure 3.1: Hierarchical structure of planar capacitive tactile sensor.

The contact layer is an insulating layer composed of flexible elastic material. The centre of the contact layer is a truncated pyramid that transmits and concentrates stress. On one hand, it induces larger deformation on the dielectric layer, which improves sensor sensitivity. On the other hand, the surface of the sensor can be protected from damage when it is in touch with sharp objects.

As a link between a mechanical force and an electrical signal, the dielectric layer is the core part of a capacitive tactile sensor. Sensors using flat dielectric layers exhibit very

low sensitivity, and the deformation under weak pressure is not sufficient to obtain detectable changes in capacitance (Zhang *et al*., 2019). To solve this problem and increase sensitivity further, Bao *et al*. proposed using a dielectric layer with pyramid structure, which allows larger deformation under the same applied pressure, resulting in higher sensitivity and faster response (Tee *et al*., 2014). Here, inverted pyramid micro-structure is introduced in the dielectric layer.

The electrode layers are used to collect electrical signals and establish connections to the measurement system. Inter-digital electrode (IDE) is a typical planar electrode composed of two separate comb-like electrodes, which are widely used in biological and chemical fields (Mazlan *et al*., 2017). Compared with dual coplanar electrodes, IDE has a larger initial capacitance as well as a uniform sensitivity distribution.

Figure 3.2 is a cross-sectional view of the sensor. For ease of illustration, it is assumed that the sensitivity field of the sensor is uniformly distributed and does not vary with the dielectric, as shown by the shading in the figure.

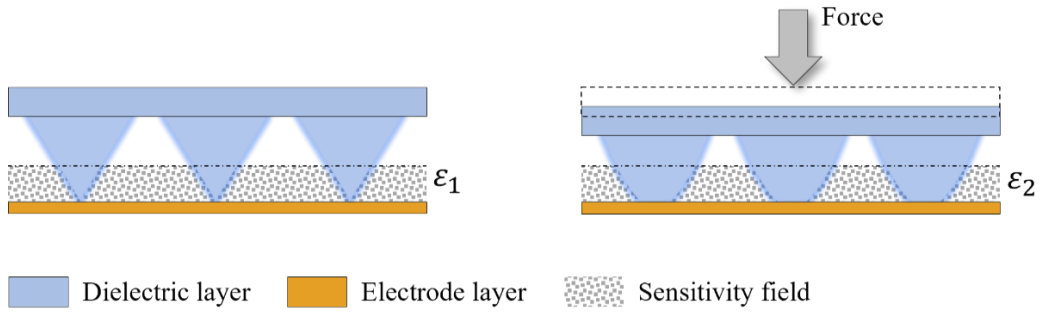

Figure 3.2: Working principle of a planar capacitive tactile sensor.

When no force is applied to the sensor, the sensitivity field is filled with air and inverted pyramids with an equivalent permittivity of ε_1. When an external force is applied, the air is squeezed out. Thus, the equivalent permittivity increases, i.e. $\varepsilon_2 > \varepsilon_1$. Because capacitance is related to permittivity, capacitance varies with an applied force. Therefore, an external pressure can be inferred by measuring the capacitance of the sensor. In

addition, the micro-structure on the surface of the dielectric layer enables the sensor to obtain greater deformation when it is subjected to external forces, improving the sensitivity of the sensor.

3.2 Optimisation of sensor structure based on finite element simulation

The performance of planar capacitive sensors depends on the design of each layer structure. In this section, the influence factors of the geometrical parameters of electrode layer and contact layer on the sensor are systematically studied.

3.2.1 Design of electrode layer

The structure and geometric parameters of IDE are shown in Figure 3.3, where w is the width of each electrode finger and s is the spacing between adjacent electrode fingers. The electric field lines formed by the electrodes are concentrated in a region within a certain height h. This region is called the sensitive region of the electrode, h is the effective detection height of the electrode and satisfies $h = s + w$ (Igreja *et al.*, 2004).

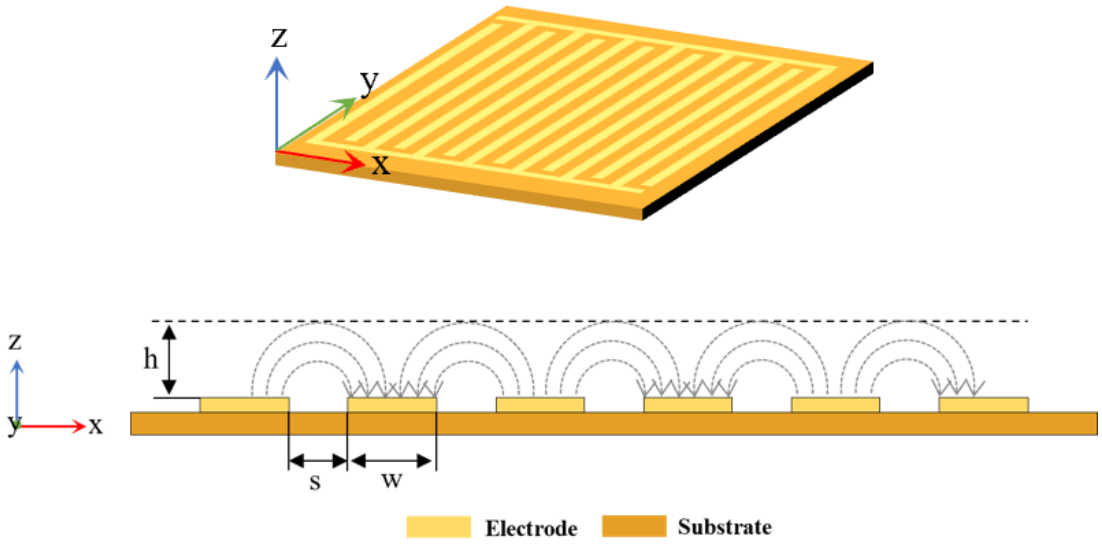

Figure 3.3: 3D (top) and 2D (bottom) geometrical structure of IDE.

To reduce the influence of parasitic capacitance on the sensor and reduce the complexity of a capacitance measurement system, the initial capacitance of the sensor should be as large as possible. Planar capacitive sensors are inherently based on fringing electric field. The theoretical model based on conformal mapping techniques was developed by Igreja and Dias (2004). With a known sensor size, regardless of the effect of the permittivity, the capacitance depends primarily on the number of fingers N and the metallisation η of the electrodes. While analytical methods can provide accurate solutions for sensors with simple geometries, an accurate method is to use the finite element method. For example, Hu and Yang (2010) used FEM to analyse the key issues in the design of planar electrodes and evaluate the performance of electrodes with different shapes.

In this section, COMSOL is used to numerically analyse the influence of the number of fingers N and metallisation rate η on the initial capacitance and sensitivity distribution of IDE. Because the length of the fingers is much larger than the spatial wavelength ($\lambda = 2(\mathrm{s} + \mathrm{w})$), the IDE model can be simplified to 2D to reduce the computational complexity. The specific parameters of the model are shown in Table 3.1.

Table 3.1: Parameters of inter-digital electrode of COMSOL simulation.

Parameters	**Value**	**Description**
L	10 mm	Length (width) of the sensor
N	10:10:50	Number of electrode fingers
η	0.2:0.1:0.9	Metallisation ratio of electrodes
w	$L \cdot \eta / N$	The width of finger
s	$L \cdot (1 - \eta)/N$	Spacing between fingers
D_e	0.05 mm	Electrode thickness (Material: Cu)
D_s	0.1 mm	Substrate thickness (Material: PI)

Figure 3.4 show that the initial capacitance is positively related to η and N, which is consistent with the literature (Igreja *et al*., 2004). In addition, under the same metallisation rate, the initial capacitance increases linearly with the increase in the number of fingers.

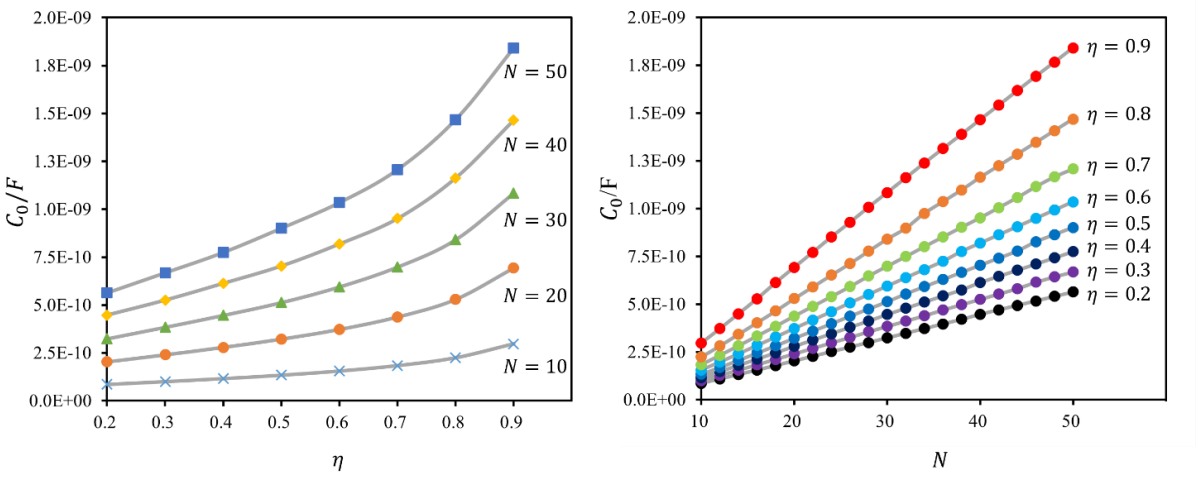

Figure 3.4: Capacitance as a function of the parameter η and N.

The spatial distribution of the electric field formed by the planar electrodes is not uniform, which is the main reason for the poor linearity of the sensor output. The sensitivity matrix S reflects the sensitivity of the capacitance to changes in permittivity of each pixel, which is calculated by (Wajman *et al*., 2004):

$$S(\mathrm{x},\mathrm{y}) = -\int_{\mathrm{p(x,y)}} \frac{\nabla \emptyset_1(\mathrm{x},\mathrm{y})}{\mathrm{V}_1} \cdot \frac{\nabla \emptyset_2(\mathrm{x},\mathrm{y})}{\mathrm{V}_2} \mathrm{dxdy} \tag{3.1}$$

where $\emptyset_1(\mathrm{x},\mathrm{y})$ and $\emptyset_2(\mathrm{x},\mathrm{y})$ are the electric potential distribution at (x, y) when V_1 and V_2 are set to two terminals, respectively. Figure 3.5 shows the sensitivity distribution of inter-digital electrodes with different metallisation ratios when N is 40. The sensitivity is high near the electrodes and decreases in the direction away from the electrodes.

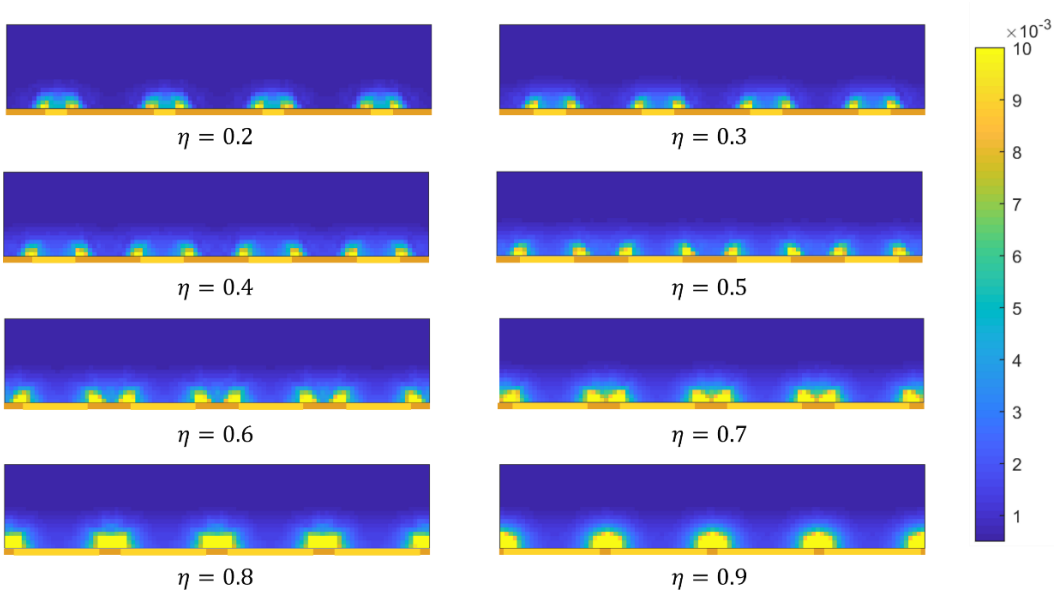

Figure 3.5: Sensitivity distribution of IDE with different metallisation ratios (N=40).

The standard deviation of the sensitivity matrix S^{dev} is used to evaluate the sensitivity distribution. The smaller S^{dev} is, the more uniform the sensitivity distribution is. Considering the electric field distribution of the inter-digital electrodes, S^{dev} is calculated only for the sensitivity within the height h. As shown in Figure 3.6, under the same metallisation ratio, the uniformity of sensitivity decreases with the increase in the number of fingers. Regardless of the number of fingers, the metallisation ratio of 0.4 to 0.6 has the best uniformity.

Both large initial capacitance and uniform sensitivity distribution are desirable for inter-digital electrodes. Therefore, C_0/S^{dev} is defined as an index γ for evaluating the overall performance of the electrodes, as shown in Figure 3.7. It can be seen that γ reaches the maximum value when η = 0.7. Therefore, the metallisation ratio of the designed inter-digital electrodes is preferably 0.7.

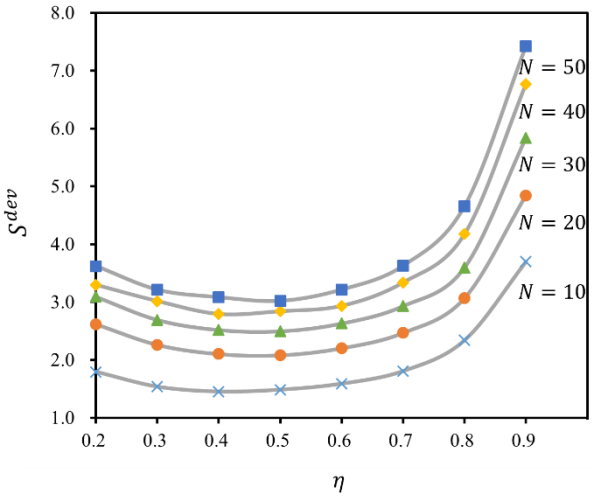

Figure 3.6: S^{dev} against metallisation ratio.

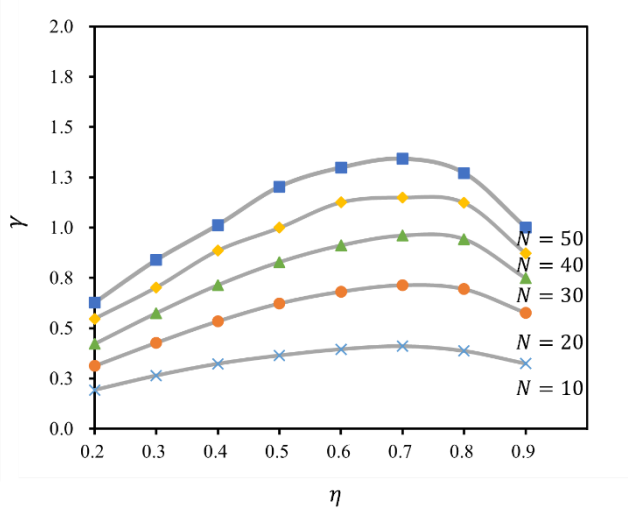

Figure 3.7: γ against metallisation ratio.

3.2.2 Design of contact layer

The centre of the contact layer is a truncated pyramid, whose bottom is a substrate with a side length of 10 mm. The cross-sectional structure of the contact layer is shown in Figure 3.8, where θ is the angle between the side and bottom of the truncated pyramid, a and b are the side length of the top and bottom of the truncated pyramid, respectively. h is the height of the truncated pyramid, and t is the thickness of the substrate.

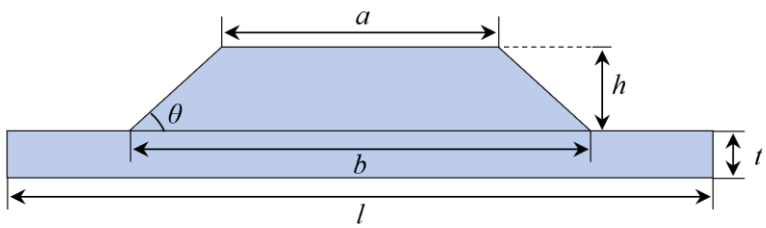

Figure 3.8: Cross-sectional structure of the contact layer.

The sensor capacitance change is essentially caused by the pressure-induced displacement of the dielectric layer, and so only the displacement change on the upper surface of the dielectric layer is simulated. Figure 3.9 (a) shows the overall displacement change of the contact layer simulated by COMSOL when the normal force is 5 N. Majority of the displacement caused by an external force exists at the top of the truncated pyramid. The

external force generates stress on the upper surface of the dielectric layer and the stress is mainly distributed in the central area of the dielectric layer. Figure 3.9 (b) is the total displacement of the dielectric layer, including the stress deformation in all directions.

Because IDE is more sensitive to the displacement change in the normal direction, the component of the displacement in the z-axis is extracted, as shown in Figure 3.9 (c), where the red area indicates the displacement direction is the same as the force direction and the blue area displacement direction is opposite to the force direction. The centre area of the dielectric layer is compressed, while the surrounding area is pulled up by the tensile force. The displacement curve of the dielectric layer in the XZ plane is shown in Figure 3.9 (d).

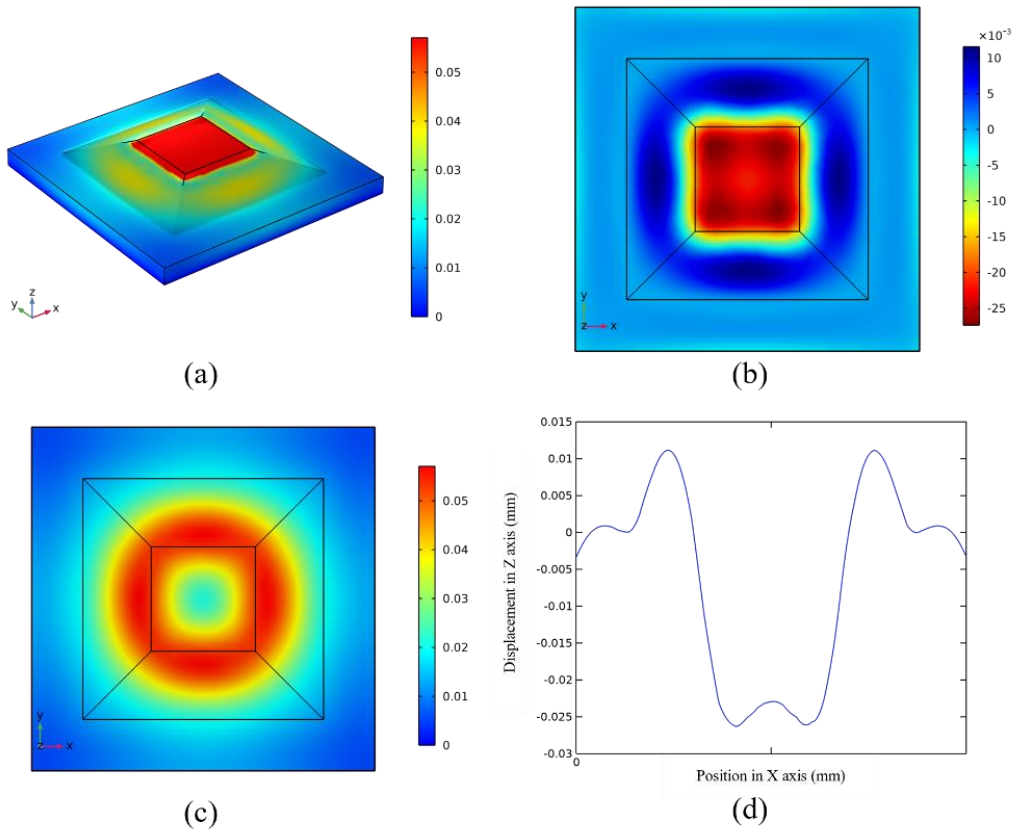

Figure 3.9: Displacement of the contact layer and the dielectric layer. (a) The overall displacement of the contact layer, (b) The top view of the total displacement of the dielectric layer, (c) The top view of the z-axis displacement of the dielectric layer, (d) The displacement curve of the XZ plane.

Because the surrounding reverse displacement is small in comparison to the displacement in the centre region, its influence on capacitance is negligible.

To investigate the effect of structure parameters on the displacement of the dielectric layer, the normal displacement is calculated with a and b as variables. h and t are set to 0.8 mm and 0.2 mm, respectively, and other parameters are listed in Table 3.2.

Table 3.2: Structure parameters of contact layer.

θ	**a=2**	**a=3**	**a=4**	**a=5**	**a=6**	**a=7**
b=6	21.8°	28.1°	38.7°	58°	-	-
b=7	17.7°	21.8°	28.1°	38.7°	58°	-
b=8	14.9°	17.7°	21.8°	28.1°	38.7°	58°

Figure 3.10 shows the normal displacement of the dielectric layer when the contact layer is subjected to a normal force of 5 N with b = 8 mm. As a increases, the normal displacement of the dielectric layer gradually decreases, while the deformed area expands. Figures 3.11 are XZ plane views of the displacements of the dielectric layers with b = 6 mm, 7 mm, and 8 mm, respectively. The comparison shows that, for a fixed a, the value of b changes little to the magnitude of the displacement. In addition, the increase of b can enlarge the displacement area. Nevertheless, the change in displacement of b is negligible compared to a. Considering the performance and manufacturing difficulty of the sensor, the truncated pyramids with a = 3 mm and b = 7 mm is selected.

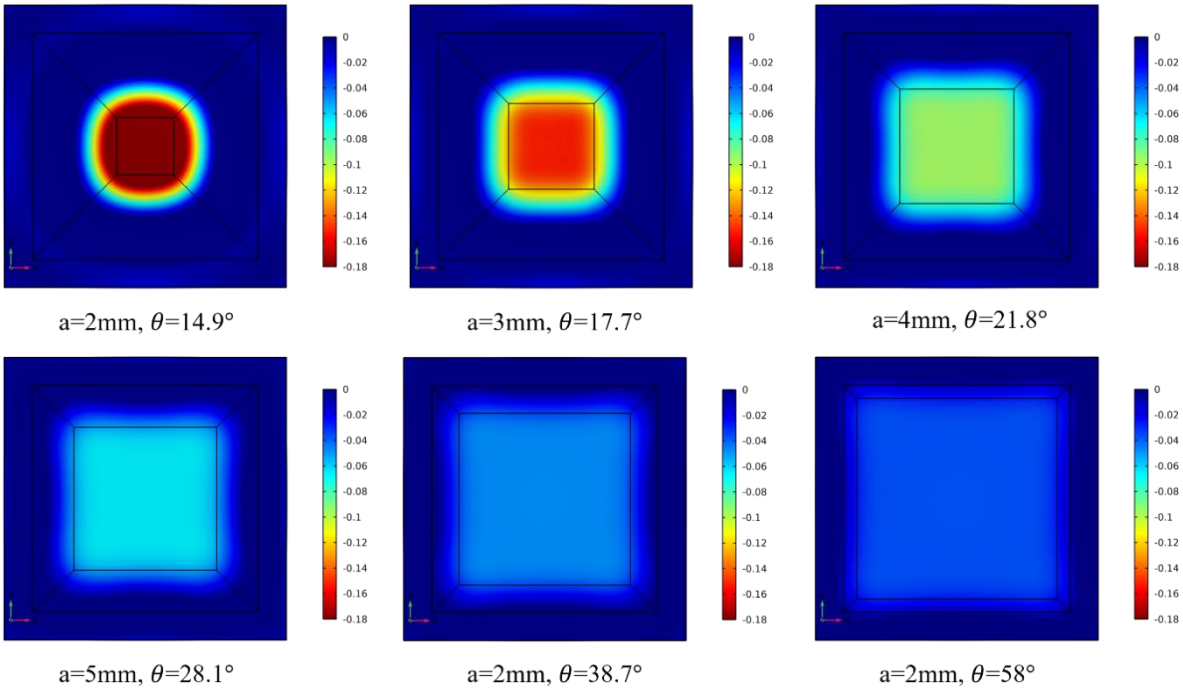

Figure 3.10: Top view of normal displacement of the dielectric layer with b = 8 mm.

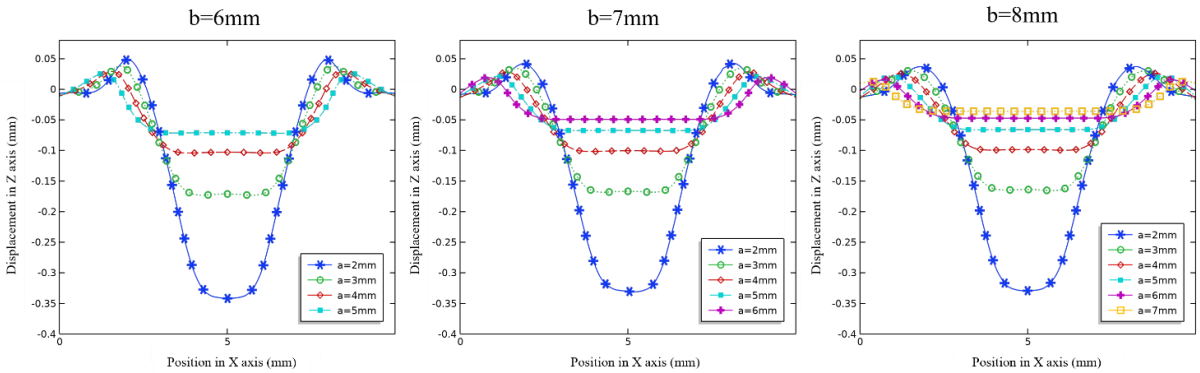

Figure 3.11: Displacement curves of XZ plane with b = 6 mm, 7 mm and 8 mm.

The influence of h and t on the stress of the dielectric layer is also investigated. The simulation results are shown in Figure 3.12. The smaller h and t, the greater the deformation of the dielectric layer. This result is in line with the actual situation. The force applied to the dielectric layer is subsequently attenuated by the contact layer, and the attenuated force increases with the thickness of the contact layer.

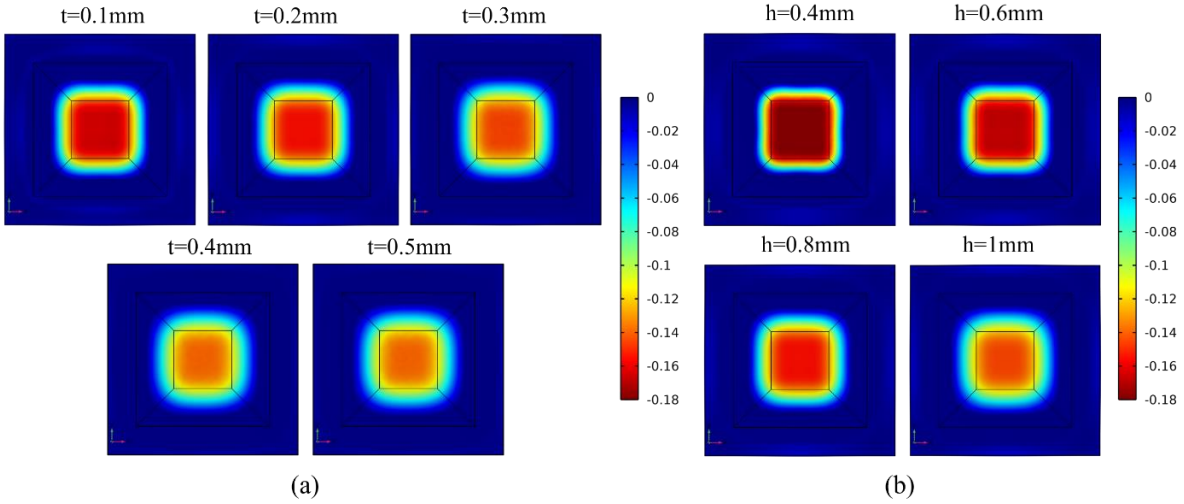

Figure 3.12: Top view of normal displacement of the dielectric layer with different (a) t and (b) h.

This is further confirmed by the displacement shown in Figure 3.13. As can be seen, the reverse deformation is proportional to the forward deformation. Reverse displacement should be avoided as it causes a reduction in capacitance change. Ultimately, h and t of the designed contact layer are selected as 0.8 mm and 0.2 mm, respectively.

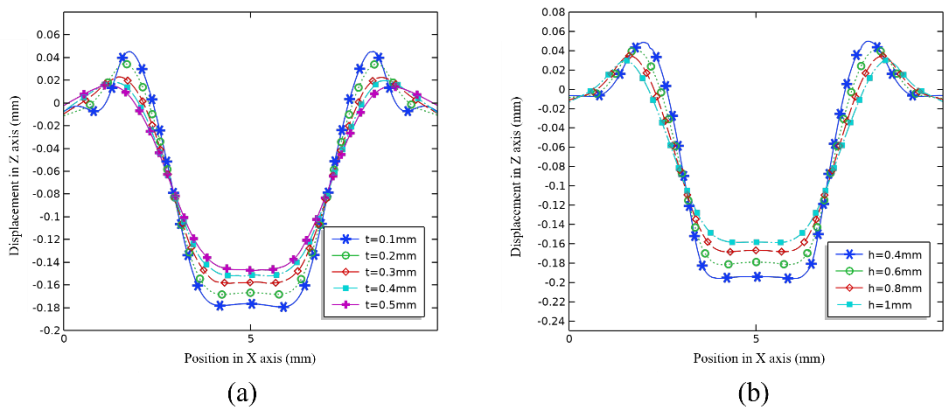

Figure 3.13: Displacement curves of the XZ plane with different (a) t and (b) h.

3.3 Optimisation and static characterisation of micro-structured dielectric layer

Finite element analysis can only be used as a reference for design verification. The influence of the electrode configuration and the design of the micro-structured dielectric layer on the static characteristics of the sensor are analysed experimentally.

3.3.1 Sensor fabrication and experiment setup

The fabricated tactile sensor needs to have good flexibility. Therefore, the electrode layer of the sensor is made of flexible PCB. The contact layer and the dielectric layer are made of polydimethylsiloxane (PDMS) by using prefabricated moulds. The detailed sensor fabrication steps and analysis will be given in Chapter 4. Figure 3.14 shows the prepared tactile sensor with dimensions of 10 mm×10 mm×1.5 mm.

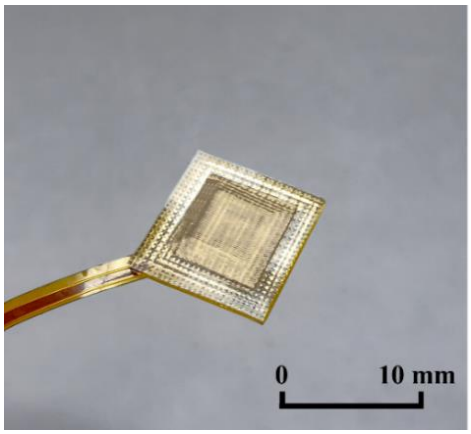

Figure 3.14: Prepared tactile sensor.

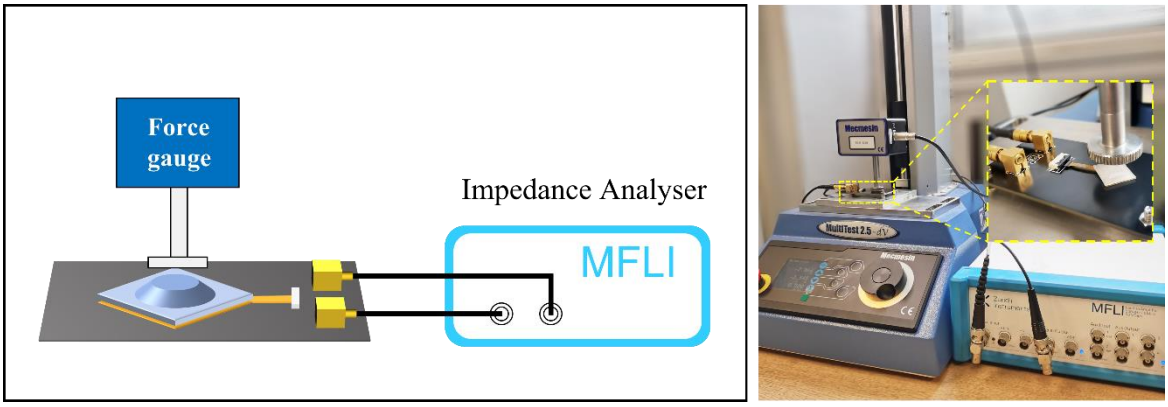

Figure 3.15: Experimental setup for testing tactile sensor.

Figure 3.15 shows the test platform used to evaluate the performance of the prepared tactile sensor, which includes a motorised test stand (MultiTest-dV(u), Mecmesin), a high-precision load sensor (ELS 50N, Mecmesin), and an impedance analyser (MFLI 500 kHz Lock-in Amplifier, Zurich Instruments). The accuracy of the load sensor is ±0.5% of reading from 5-100% of the capacity and the resolution of displacement is 0.001 mm.

Capacitive sensors are highly susceptible to interference from the environment. Therefore, the prepared tactile sensor is connected to an SMB adapter and subsequently to the impedance analyser through a coaxial shielded cable, as shown in Figure 3.15. The probe of the load sensor is located above the tactile sensor and is driven by the motorised lifting system to exert pressure on it. VectorPro MT software (Mecmesin) allows the user to set parameters like pressure magnitude, pressure application speed, and number of load cycle. The impedance analyser collects the capacitance from the tactile sensor, which is subsequently recorded and visualised by a computer.

3.3.2 Influence of electrode structure on sensor sensitivity

The electrode structure of the planar capacitive sensor has a great influence on the initial capacitance value and sensitivity distribution. Among the planar electrodes with different patterns, the square spiral electrodes have a more uniform sensitivity distribution than the inter-digital electrodes (Hu and Yang, 2010). Three square spiral electrodes with varying number of turns are fabricated by using flexible PCB, which are denoted as E1, E2 and E3, respectively, as shown in Figure 3.16. The dielectric layer and the contact layer are made of PDMS with the same structure. In the absence of pressure, the capacitances of the three sensors are 2.324 pF, 3.705 pF and 7.965 pF, respectively, measured by the impedance analyser at 100 kHz.

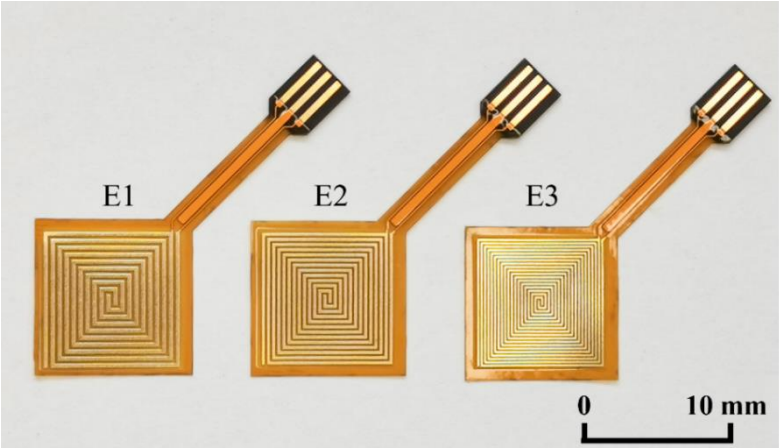

Figure 3.16: Square spiral FPCB electrodes with varying number of turns.

For capacitive sensors, grounded shield is usually used to reduce stray capacitance and noise, and confine the sensitive field to the region of interest (Li *et al.*, 2006). The effect of shielding on the sensor should be considered. The shield in this case is a solid square copper plate, which is placed on the opposite side of the electrodes. Compared to the sensor without the shield, the initial capacitance values of the sensor with the shield are significantly reduced to 0.551 pF, 0.915 pF and 1.951 pF.

A normal force of 0-10N is applied to the sensor through the load cell. Because the contact area between the load sensor and the contact layer is 0.16 cm^2, the corresponding pressure is 0-625 kPa. The relative change in capacitance as a function of pressure is measured as shown in Figure 3.17, where ΔC is the difference between the measured capacitance value and the initial capacitance value. As shown, the sensor with the shield has a larger change in capacitance than the sensor without the shield at the same pressure.

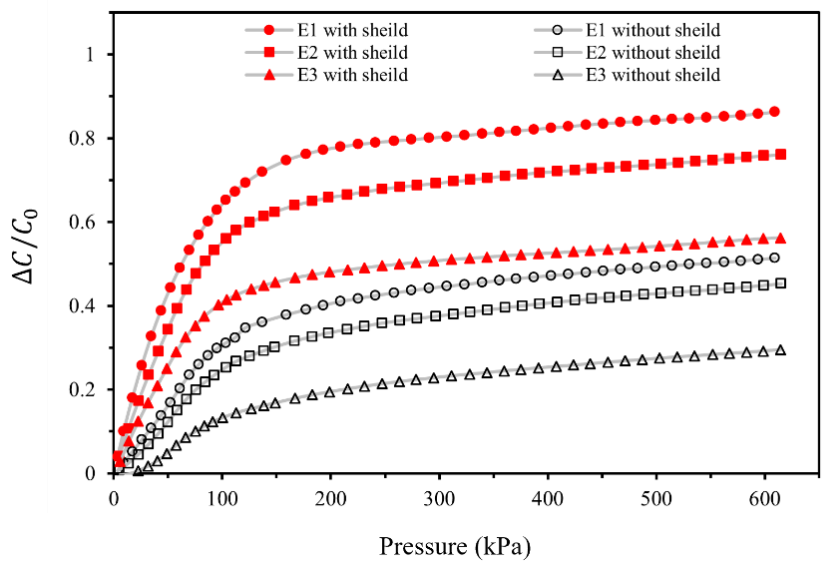

Figure 3.17: Relative capacitance changes of the sensor with different electrode structures.

Sensitivity describes the change in capacitance relative to its initial value over a specific pressure range. High sensitivity means a high signal-to-noise ratio (SNR), enabling the sensor to distinguish subtle changes in pressure. Mathematically, sensitivity S is defined

as the slope of the curve (Yang *et al*., 2017). As shown in Figure 3.18, the sensitivity of the sensor decreases as the number of electrode turns increases. According to the previous simulation, the sensitivity increases with the decrease in the electrode spacing, and so E3 should have the greatest capacitance change. Nonetheless, the changes in capacitance value are minimal compared to the initial capacitance. In contrast, E1 has higher sensitivity. As a result, E1 with shield is chosen to carry out the following experiments.

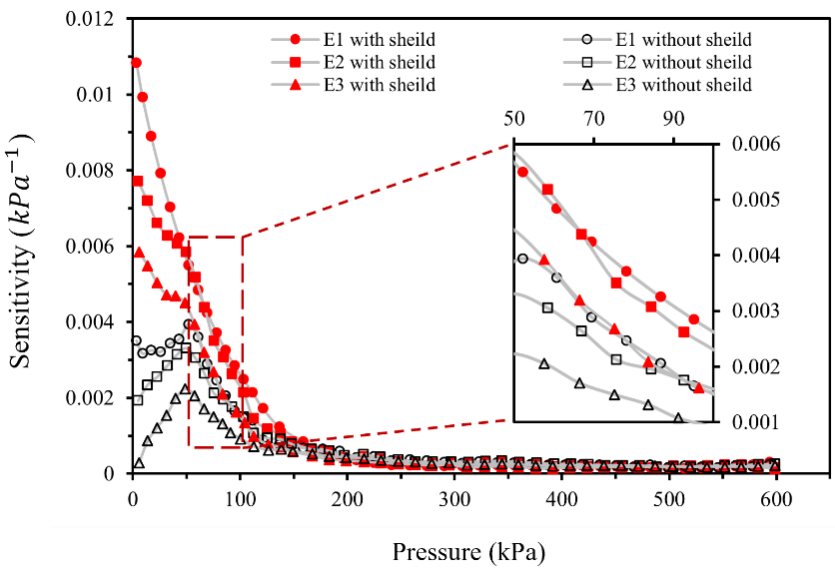

Figure 3.18: Sensitivity changes of the sensor with different electrode structures.

3.3.3 Optimisation of micro-structured dielectric layer

As mentioned, the pyramid array in the dielectric layer can improve the sensitivity of the sensor, which can be attributed to two aspects: (1) The air gap between the pyramids reduces the equivalent Yang's modulus of the dielectric layer. (2) The compression induces an additional change in the relative permittivity.

Luo *et al*. (2018) demonstrated the improvement of sensor sensitivity by increasing the pyramid spacing through simulation and experiments. The micro-structured dielectric layer enables high sensitivity. However, the trade-off is the resulting hysteresis error, i.e. the difference in capacitance between loading and unloading of the same pressure is large

(Bergstrom and Boyce, 2001; Luo *et al.*, 2016). Cheng *et al.* (2017) modified the structure with pyramids of various sizes, which enabled the sensor to maintain high sensitivity while hysteresis is significantly reduced. The following section explores the effect of the size and spacing of the pyramids on the sensor in terms of sensitivity and hysteresis.

Pyramids with different size

As shown in Figure 3.19, pyramid dielectric layers with equal spacing of 400 μm and bottom lengths of 150 μm, 225 μm and 300 μm are prepared. Spacing refers to the distance between the tips of adjacent pyramids. The slope angle of the pyramid is 54.7°, so the heights of the pyramids are 212 μm, 159 μm and 106 μm. The initial capacitances of the three sensors are 0.886 pF, 0.724 pF and 0.63 pF, respectively. The sensor with the smallest pyramid has the largest initial capacitance due to the largest proportion of the dielectric layer in the sensitive area, resulting in the largest equivalent permittivity.

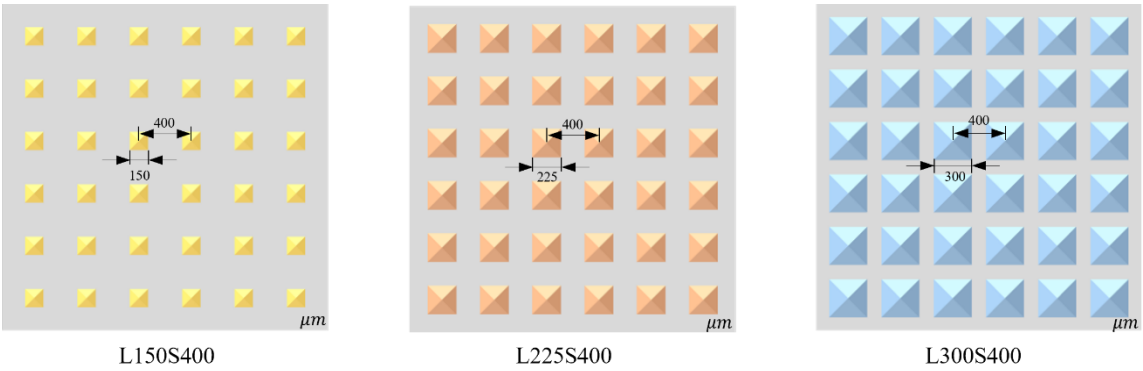

Figure 3.19: Pyramids with same spacing but different size.

The capacitance-pressure characteristics of the above three sensors are shown in Figure 3.20. Because the contact area of the pyramid tips with the electrodes is only related to the spacing of the pyramids, these three sensors have similar stress-strain relations in the initial stage. The difference between the curves is because the sensitivity is greatest near the electrodes, and the dielectric layer with the small pyramids is closer to the electrodes, so the relative change in capacitance is greater under the same pressure. However, with a

further increase in pressure, the pyramids are completely compressed, causing a sharp drop in sensitivity. Specifically, the sensor L150S400 has the highest sensitivity within 100 kPa but the lowest sensitivity within 100 kPa-600 kPa. The sensor L300S400 has the highest sensitivity and linearity in the range of 100 kPa-600 kPa.

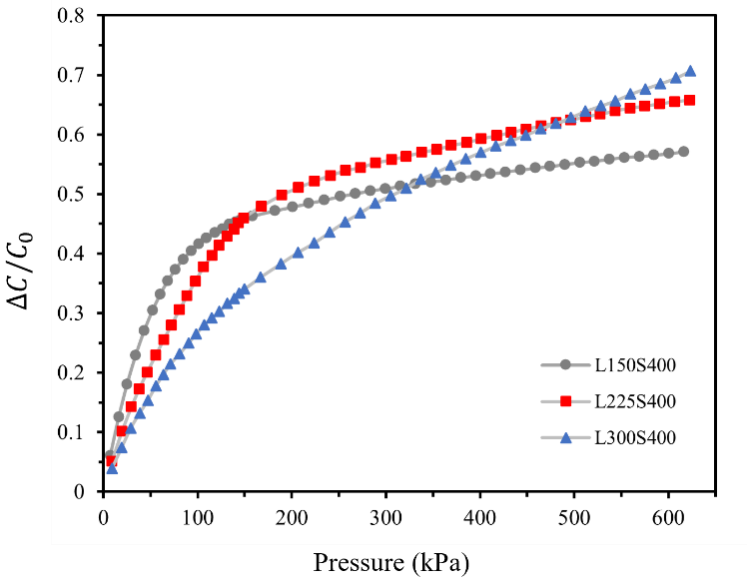

Figure 3.20: Capacitance-pressure characterisation of sensors with pyramids of different sizes.

It can be concluded that the small pyramid enables the sensor to obtain high sensitivity in the low-pressure region. Although the large pyramid sacrifices the sensitivity of the sensor in the low-pressure region, a larger measurement range and higher linearity can be obtained.

Pyramids with different spacing

Figure 3.21 shows three pyramid structures with the bottom side lengths of 300 um and the spacing of 400 um, 500 um and 600 um, respectively. The capacitance change of the sensor against the pressure is shown in Figure 3.22.

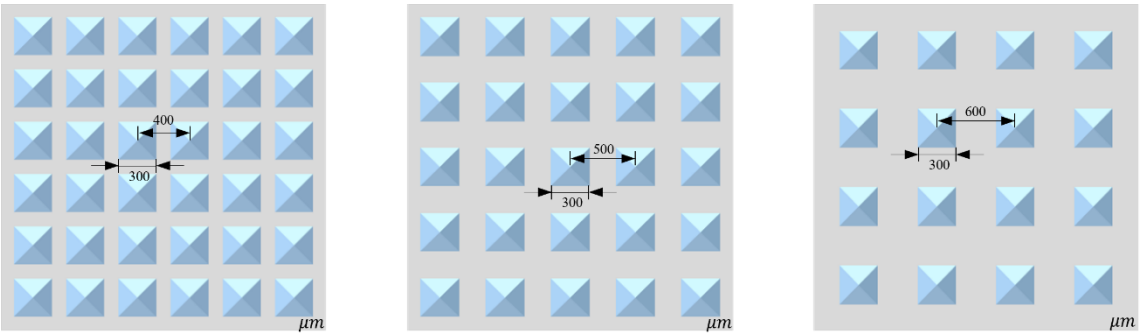

L300S400 L300S500 L300S600

Figure 3.21: Pyramids with same size but different spacing.

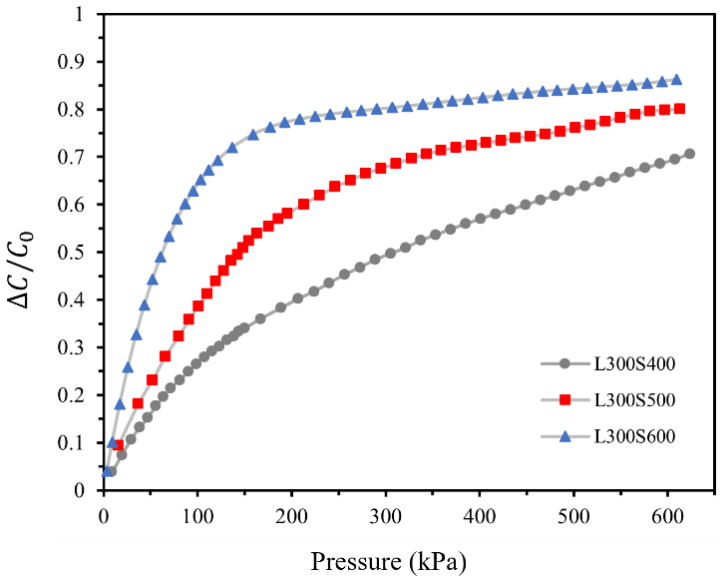

Figure 3.22: Capacitance-pressure characterisation of sensors with pyramids of different spacing.

The smaller the spacing, the higher the equivalent permittivity, and therefore the larger the initial capacitance. Larger pyramid spacing means less pyramids are used to share external forces and the smaller the equivalent Young's modulus of the dielectric layer. Therefore, under the same pressure, a dielectric layer with a large spacing will undergo greater deformation, and a higher sensitivity can be achieved. However, the measuring range of the sensor decreases as the spacing increases. Note that closely spaced pyramids induce larger dielectric constant changes subjected to stress than sparsely spaced pyramids. However, this is negligible relative to the change in capacitance caused by changing the elastic modulus.

Modified pyramid

Based on the above experimental results and analysis, the sensitivity and measuring range are trade-offs. The spacing and size of the pyramids need to be adjusted to obtain the desired sensitivity and measuring range according to the practical application.

Combining the characteristics of these two aspects, the pyramid structure in the dielectric layer is modified as shown in Figure 3.23. The three modified dielectric layers consist of pyramids of various sizes arranged with the same spacing, named M1, M2 and M3, respectively.

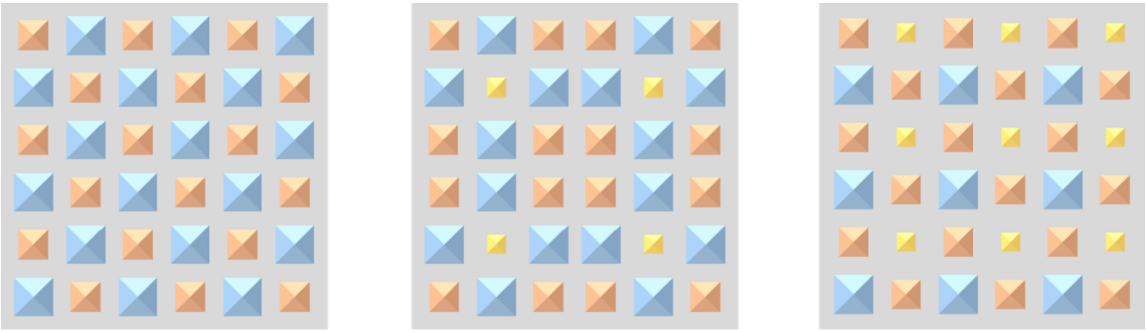

M1 M2 M3

Figure 3.23: Modified pyramids with various sizes arranged with the same spacing.

The characteristic curve is shown in Figure 3.25. Comparing with Figure 3.20 and Figure 3.22, the sensitivity of the sensor with the modified dielectric layer is significantly improved with the full range. Furthermore, in the high-pressure range (> 100 kPa), the capacitance change still increases linearly. This is attributed to the difference in the contact area of the dielectric layer with the electrode layer in the low-pressure and the high-pressure regions. As shown in Figure 3.24, the sensor has a high sensitivity during the initial stage of applying pressure because only the largest pyramid is subjected to pressure. As the pressure rises, the small pyramids contact the electrode layers, taking up part of the pressure. The modified pyramid dielectric layer allows the sensor not to be fully compressed as quickly in high pressure region while maintaining high sensitivity.

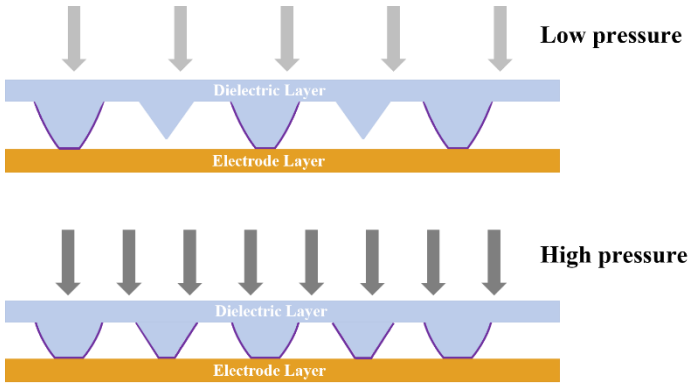

Figure 3.24: Deformation of the modified pyramids.

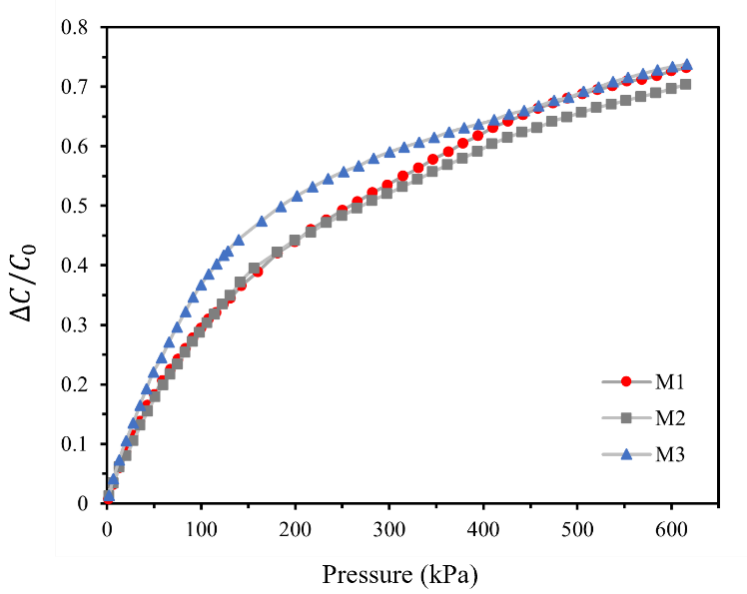

Figure 3.25: Capacitance-pressure characterisation of sensors with modified pyramids.

Comparison of sensitivity and hysteresis errors

Through the above analysis, in general, the sensitivity of the sensor decreases with the increase in pressure. The capacitance change over the full pressure range can be roughly divided into two linear regions. Taking Sensor L150S400 as an example, as shown in Figure 3.26, the sensitivity in the low-pressure region ($S_{low} = 0.0058$ kPa^{-1}) is much higher than the sensitivity of the high-pressure region ($S_{high} = 0.00018$ kPa^{-1}), because in the low-pressure region, the stress is mainly concentrated on the top of the pyramid, which is easily compressed. In the high-pressure region, the dielectric layer is almost

compressed into a planar structure. Therefore, the capacitance hardly changes, and the sensitivity is greatly reduced.

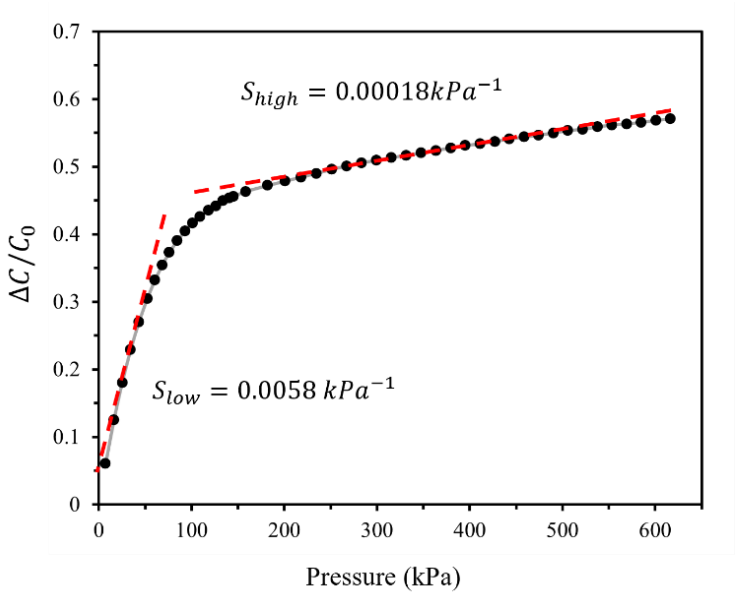

Figure 3.26: Sensitivity of Sensor L150S400.

The sensitivity can be effectively improved by reducing the density of the pyramids. However, this results in high hysteresis. This is most likely caused by the viscoelastic properties of flexible materials (Lee *et al.*, 2015; Li *et al.*, 2016). In addition, the increase in spacing causes interfacial adhesion, which is also an important factor in sensor hysteresis (Cheng *et al.*, 2017). The evaluation of hysteresis is done by sequentially applying loading and unloading pressure to the sensor. Figure 3.27 shows the hysteresis characteristic of the Sensor L150S400.

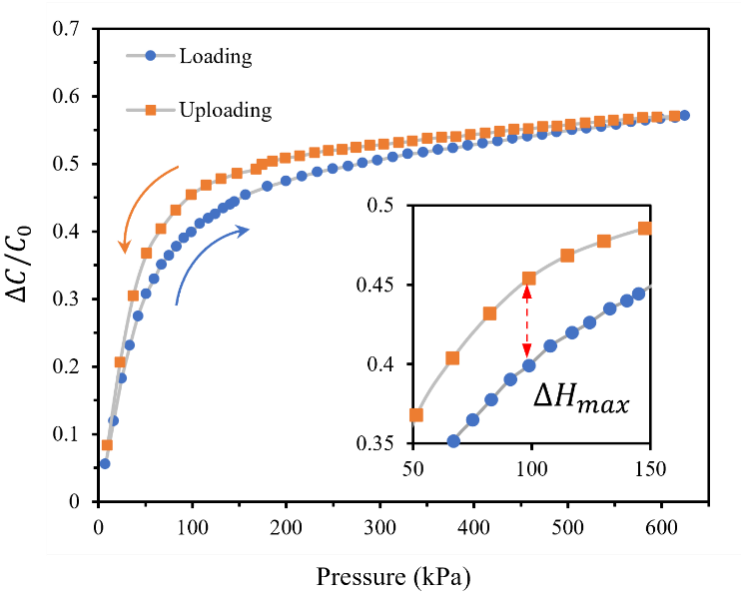

Figure 3.27: Hysteresis of Sensor L150S400.

The formula for calculating the hysteresis error δ_H is:

$$\delta_H = \frac{\Delta H_{max}}{C_{full}} \times 100\% \tag{3.2}$$

where ΔH_{max} is the maximum deviation of the capacitance in the forward and reverse directions under the same pressure, and C_{full} is the full-scale value of the measurement capacitance.

Table 3.3 shows the sensitivity and hysteresis error of sensors based on the above eight dielectric layer structures. As can be seen, there is a clear trade-off between sensitivity and hysteresis. Both the sensitivity and the hysteresis error increase significantly as the pyramid spacing increases. Among them, the sensor L300S600 has the highest sensitivity in the low-pressure area, but the lowest sensitivity in the high-pressure region and the hysteresis error is as high as 8.05%. The modified dielectric layer structure enables the sensor to have high sensitivity in both low-pressure and high-pressure regions. The hysteresis error of M1 is as low as 4.23%. This experiment has verified the effectiveness

of improving sensor sensitivity and hysteresis error by adopting multi-sized pyramidal dielectric layers.

Table 3.3: Comparison of sensitivity and hysteresis error of sensors with different dielectric layers.

Parameters	L150S400	L225S400	L300S400	L300S500	L300S600	M1	M2	M3
Sensitivity(low)	0.58%	0.40%	0.30%	0.38%	0.92%	0.36%	0.34%	0.44%
Sensitivity(High)	0.02%	0.03%	0.06%	0.03%	0.02%	0.05%	0.05%	0.05%
Hysteresis error	8.51%	4.88%	3.89%	6.02%	8.05%	4.23%	4.51%	6.00%

3.4 Dynamic performance of the sensor

3.4.1 Response and relaxation time

Response time is defined as the time it takes for a sensor to reach its stable value under applied pressure, which is critical for real-time tactile sensing applications. Relaxation time is the opposite of response time, which refers to the time it takes for the sensor to return to its initial value when pressure is removed. To measure the response time, a constant pressure is applied to the sensor and unloaded after 1 s, the whole process should be fast and stable.

The response curve is shown in Figure 3.28, the inset is a magnification of the instantaneous capacitive response to loading and unloading pressure. Because the sampling frequency of the impedance analyser is 13.39 kHz, the time interval between adjacent data points is 74.7 μs. Therefore, the response time of the tactile sensor is estimated to be 6.9 ms and the relaxation time is 34.7 ms.

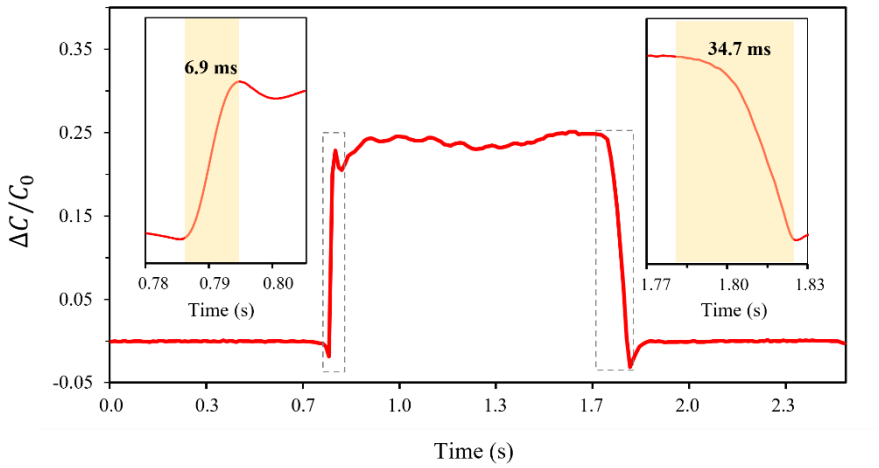

Figure 3.28: Characterisation of response time and recovery time.

The relaxation time is slightly larger than the response time, owing to the viscoelasticity of PDMS (Lü *et al.*, 2017). After several experiments, the response time and relaxation time of the sensor are maintained within 6.5-8.3 ms and 30.2-37.4 ms, respectively, indicating that the response speed of the sensor remained at a high level. Note that the response time of this sensor is higher than that of human skin, which is 30-50 ms (Chortos and Bao, 2014). This demonstrates that this tactile sensor has great prospects in human tactile detection applications.

3.4.2 Stability and reliability

Tactile sensors need to be stable and reliable under continuous pressure. Thus, the sensor is subjected to a pressure cycling test. Specifically, a pressure of 30-150 kPa is sequentially applied to the tactile sensor, and the pressure is released after holding for 1 s. The applied pressure is shown in the upper curve of Figure 3.29. It can be observed that the changes of pressure and capacitance are offset. This phenomenon is caused by the elastic hysteresis of PDMS. The shape of PDMS changes sharply under pressure. However, long polymer chain networks need time to relax. Therefore, the shape of PDMS changes with time, resulting in the reduction of pressure and capacitance. Furthermore,

the sensor can accurately measure the capacitance under different pressures, so the approximate range of pressure can be determined from the capacitance. The above tests show that the prepared capacitive sensor has good stability and reliability under continuous load application.

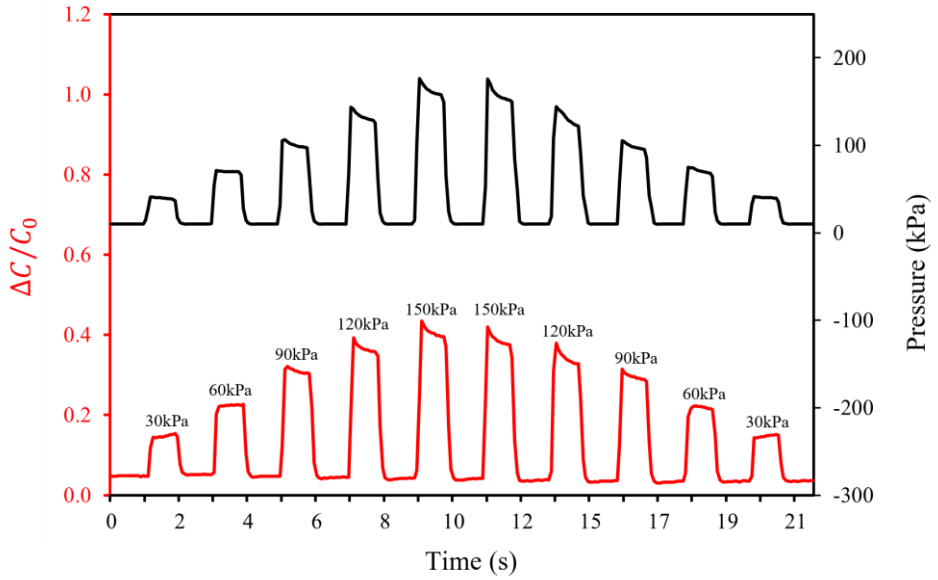

Figure 3.29: Stability and reliability test of the sensor.

3.4.3 Repeatability and durability

Good repeatability and durability guarantee the practical application of the sensor. The repeatability of the sensor refers to the misalignment of the capacitance-pressure curves when the sensor is loaded with pressure in the same direction for many times. The repeatability error δ_r is defined as:

$$\delta_r = \frac{\delta_{max}}{C_{full}} \times 100\% \tag{3.3}$$

where C_{full} is the full-scale capacitance, and δ_{max} is the maximum value of the standard deviation of the measured capacitance under the same pressure. The calculation equation is as follows:

$$\delta_i = \sqrt{\frac{1}{M-1}\sum_{j=1}^{M}(C_{i,j} - \bar{C}_j)^2} \tag{3.4}$$

where M is the number of measurement points, N is the number of cycles, $C_{i,j}$ is the capacitance value of the jth measurement point in the ith cycle, $\bar{C}_j$ is the average capacitance value of the jth measurement point in all cycles.

The tactile sensor is subjected to 100 cyclic loadings from 0 to 550 kPa under the same conditions. The characteristic curves of the 1st, 30th, 60th and 90th cycles are selected for comparison. As shown in Figure 3.30, the curves of the four cycles basically coincide without large deviation, indicating good repeatability.

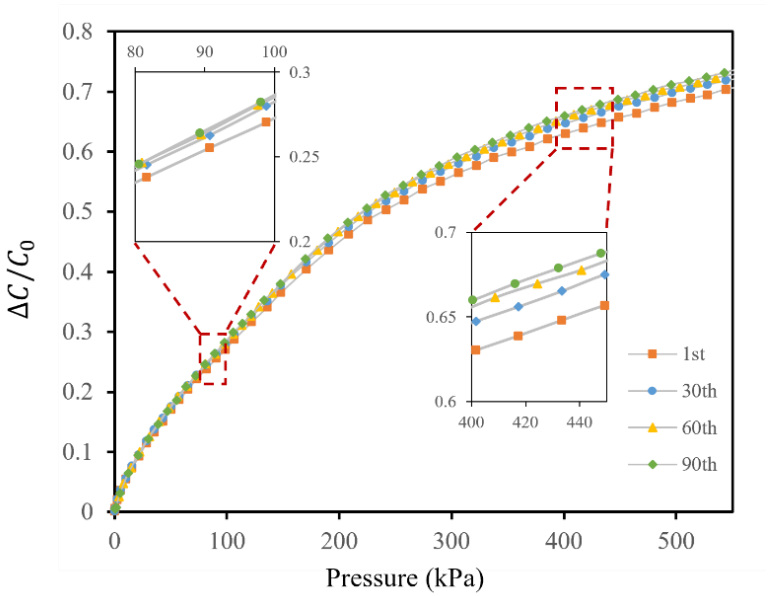

Figure 3.30: Repeatability test of the sensor.

The repeatability error differs between high- and low-pressure regions. Within 0-100 kPa, the repeatability error is 2.2%, while within 0-550 kPa, the repeatability error is 4.9%. The main reason is the non-uniform distribution of the sensitivity of the planar electrode, i.e., the closer to the electrode, the greater the sensitivity. As a result, the error is more obvious under high pressure than under low pressure.

The repeatability errors of the 1st to 10th, 31st to 40th, 61st to 70th and 91st to 100th measurements are calculated respectively, as listed in Table 3.4. The repeatability error decreases as the number of cycles increases. The capacitance value is not stable in the first few cycles due to the presence of air gaps between the sensor layers. Repeatedly applying pressure to the sensor, the interlayer interface and the pyramidal structure of the dielectric layer gradually reach a stable state, resulting in a decrease in error.

Table 3.4: Comparison of repeatability errors at different cycle stages.

Test Cycles	**1st-10th**	**31st-40th**	**61st-70th**	**91st-100th**
Repeatability error	3.1%	2.3%	1.9%	1.8%

The sensor should maintain a stable output under long-term pressure loading and unloading in practical applications. The durability of the sensor is tested by loading and unloading a pressure of 60 kPa at the same time interval for a total of 1000 cycles. Figure 3.31 (a) and Figure 3.31 (b) show the capacitance responses for the first and last 200 test cycles, respectively. During the first 100 cycles, the overall baseline of capacitance drifts slightly. After 100 cycles, the capacitance of the sensor under pressure is almost unchanged. Figure 3.32 shows the sensor response extracted from the 901st to 910th cycles. It can be seen that the applied pressure and measured capacitance have a high consistency. The maximum difference in capacitance under pressure is only 1.4%, which reveals that the sensor has good durability.

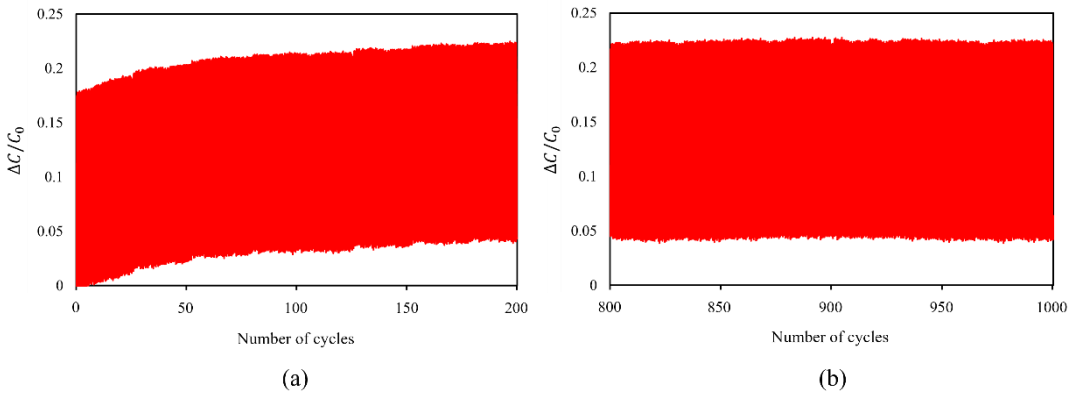

Figure 3.31: Durability test for (a) the first 200 cycles and (b) the last 200 cycles.

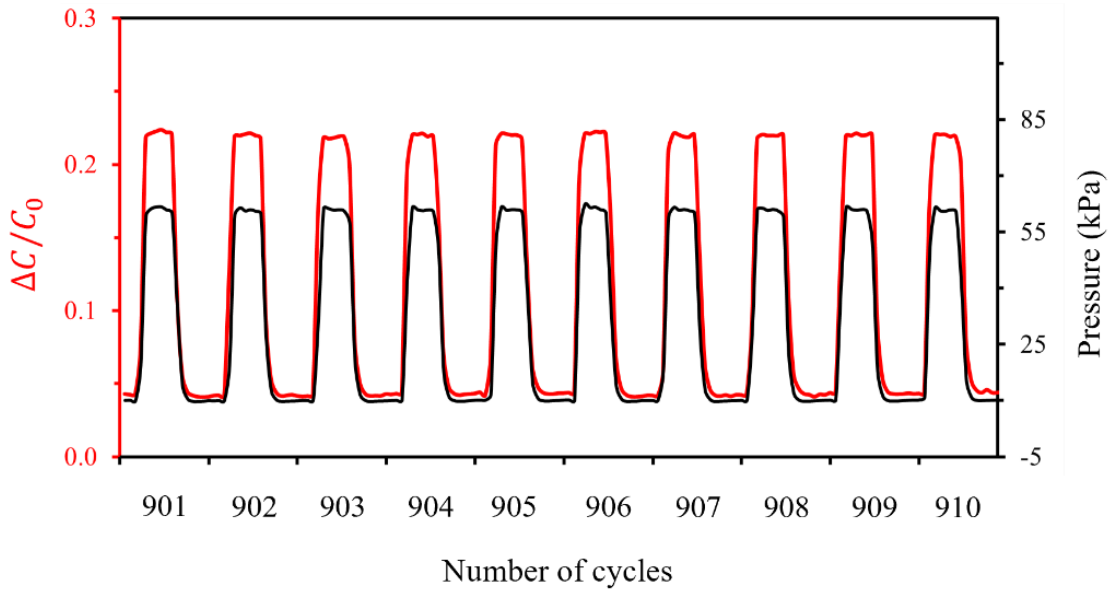

Figure 3.32: Extracted 10-cycle durability test.

3.4.4 Detection limit

The detection limit is used to assess whether the minimum pressure that a sensor can detect is sufficient for a specific application. To test the limit of the pressure detection of the sensor, a minimum pressure is applied to the sensor via the load cell. The accuracy of the load cell is 1 mN, and experiments show that the pressure is stable above 10 mN. Furthermore, the contact layer is removed in the experiment to reduce pressure by increasing contact area. Thus, a force of 10 mN corresponds to a pressure of 100 Pa for a sensor with dimensions of 10 mm × 10 mm.

Figure 3.33 shows the test results of gradually adding a pressure of 100 Pa. The sensor can detect observable changes in capacitance even at 100 Pa. During the loading process, the capacitance of the sensor exhibits a distinct step change. Moreover, once the pressure is released, the capacitance returns to its initial value. The capacitance is fluctuated, which may be caused by the vibration from the operation of the test bench and noise from the measurement system. Note that the assessment of the minimum detected pressure is often limited by the accuracy of the load cells and measuring instruments, and so the actual detection limit of the sensor is lower than 100 Pa.

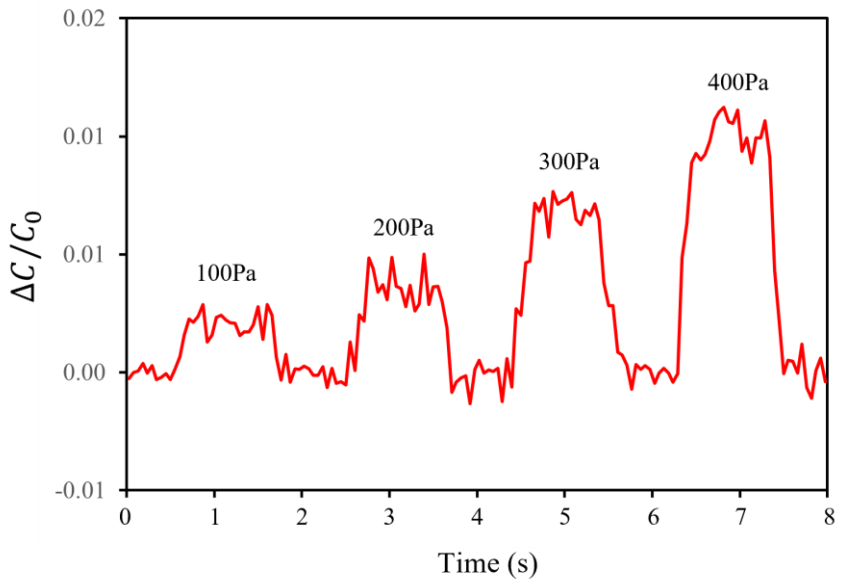

Figure 3.33: Pressure detection limit test.

3.5 Summary

In this work, a new design of a planar capacitive-based tactile sensor is presented as an alternative to conventional parallel-plate capacitive sensors. A simple sensor model is developed that provides a quantitative relation between the sensor structure and the initial capacitance and sensitivity. The optimisation strategy of the contact layer and electrode layer of the sensor is described in detail, which provides suitable parameters for the fabrication of the sensor. A tactile sensor with tuneable sensitivity and measurement range

is achieved by using an inverted pyramid micro-structured dielectric layer. The effect of the arrangement of the pyramids on the sensor performance is experimentally investigated. The dynamic response, repeatability and durability of the improved sensor are also evaluated. This work validates the efficacy of planar capacitive sensors for tactile sensing and provides a rational and effective design basis for future sensor applications.

Chapter 4 Design and fabrication of a novel capacitive tactile sensor for multi-directional force detection

In this chapter, a novel flexible tactile sensor based on planar capacitance is proposed to measure multi-directional force. The sensor is made up of three inter-digital electrodes with a 120° included angle, forming three capacitors. With a truncated cone-structured contact layer above the electrodes, the three-dimensional (3D) force is decomposed into normal and shear components, resulting in different capacitance changes. The dielectric layer is optimised with an improved pyramid micro-structure array, which improves the measurement sensitivity in the shear direction. Furthermore, a general and efficient fabrication process for this sensor is presented, with the key steps described and analysed. To characterise the performance of the sensor, a 3D force loading platform and a capacitance measurement system are built. The results show that the fabricated sensor can discriminate in any direction with only three capacitances.

4.1 Structure design and operating principle

4.1.1 Sensor design

Figure 4.1 (a) shows the three-layer structure of the sensor, from bottom to top are electrode layer, dielectric layer and contact layer. The electrode layer consists of three comb-shaped electrodes with a 120° included angle. The electrode pattern and its equivalent circuit are shown in Figure 4.1 (b) and (c). Three capacitors are formed by adjacent electrodes, defined as C_{12}, C_{13} and C_{23}. 3D force can be inferred from the changes in these three capacitances. The micro-structured dielectric layer is used to improve the sensitivity of the sensor, and the truncated cone structure above it acts as the

contact layer, which is the key to decompose the external force into normal and shear forces.

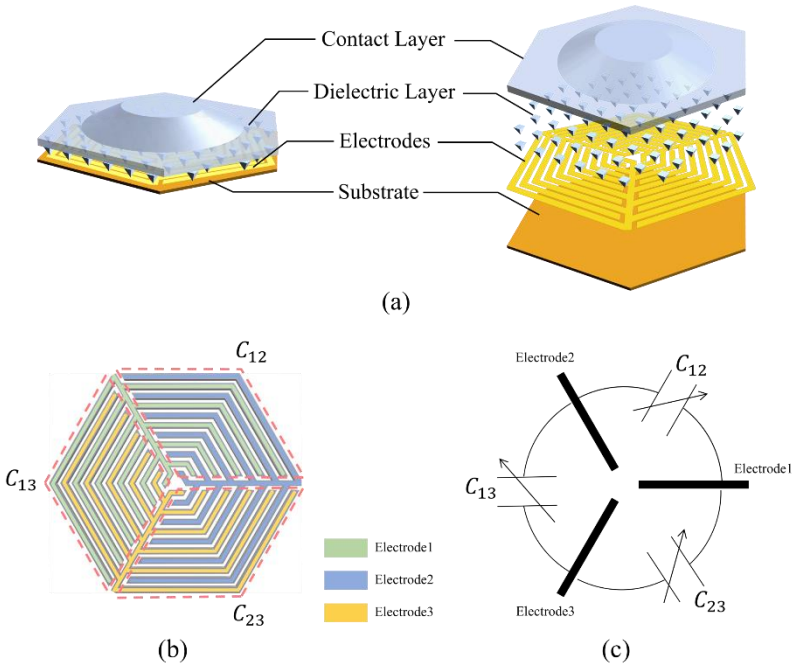

Figure 4.1: Conceptual diagram of the proposed sensor. (a) Structure of the sensor. (b) Electrode pattern. (c) Equivalent circuit of electrodes.

4.1.2 Working principle

The simplified 2D diagram in Figure 4.2 explains the working principle of this sensor. Assume the sensor has two planar capacitors in the X-axis direction, C_1 and C_2. When a normal force is applied to the surface of the truncated cone, the dielectric layer above the two capacitors is compressed, resulting in an increase in C_1 and C_2, as shown in Figure 4.2 (a). When a shear force is applied to the sensor, the dielectric layer in the same direction as the shear force experiences compression, and the dielectric layer in the opposite direction experiences tension. As a result, the capacitance of C_2 increases, while the capacitance of C_1 decreases, as shown in Figure 4.2 (b).

Theoretically, only three capacitors are sufficient for 3D force detection. Figure 4.3 shows the capacitance change under four typical forces, where red and green represent capacitance increases and capacitance decreases. When a normal force F_z (in the direction of the -z axis) is applied to the surface of the truncated cone, the force is transmitted uniformly to the three inter-digital capacitors, resulting in dielectric layer compression. Due to the symmetry of the structure, the changes of the three capacitances are theoretically the same, as shown in Figure 4.3 (a).

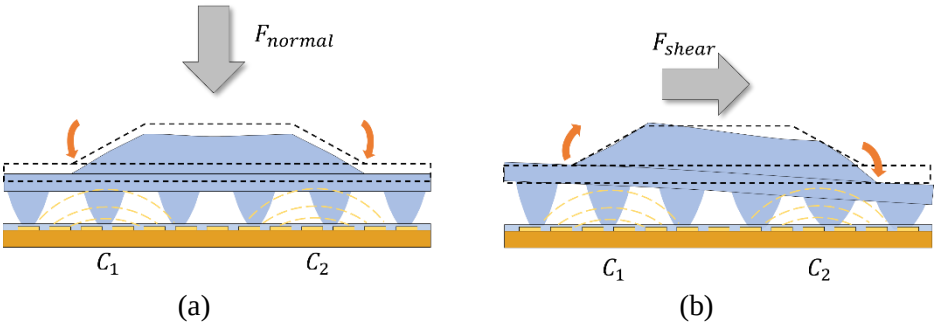

Figure 4.2: Working principle of the detection of (a) normal force and (b) shear force.

When a shear force F_s is applied to the surface of the truncated cone, a torque perpendicular to F_s is generated, causing the dielectric layers on either side in compression and tension, respectively. As shown in Figure 4.3 (b), when the direction of Fs is 60° from the x-axis, C_{12} increases while C_{13} and C_{23} decrease. Similarly, when the shear force is applied in the direction of 180° and 300°, the changes in the three capacitances are illustrated in Figure 4.3 (c) and (d), respectively.

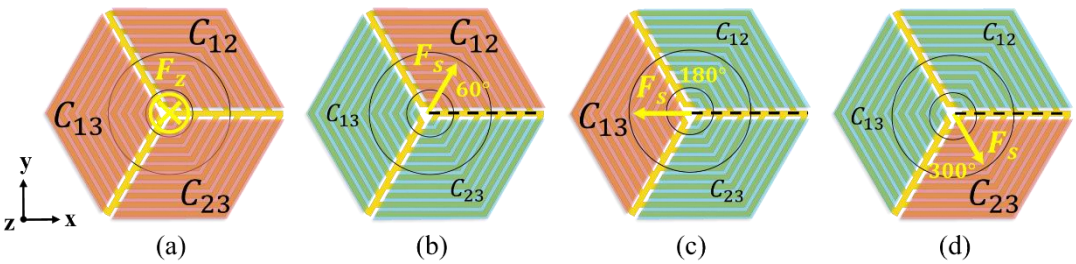

Figure 4.3: Capacitance change under force in different directions. (a) Normal force. (b) Shear force with 60° angle. (c) Shear force with 180° angle. (d) Shear force with 300° angle.

Table 4.1 summarises the changes in the three capacitances under different forces. The symbols '+' and '-' represent capacitance increases and decreases, respectively. Therefore, the force in any direction can be inferred from the changes of C_{12}, C_{13} and C_{23}.

Table 4.1: Capacitance change under different force.

Force	F_z	F_{s60}	F_{s180}	F_{s300}
C_{12}	$+$	$+$	$-$	$-$
C_{13}	$+$	$-$	$+$	$-$
C_{23}	$+$	$-$	$-$	$+$

4.2 Finite element analysis by COMSOL

4.2.1 Modelling and simulation of sensor

This section validates the sensor structure design using the finite element software COMSOL. The structural parameters and material parameters of the sensor are shown in Figure 4.4. Polydimethylsiloxane (PDMS) is used for both the contact layer and the dielectric layer. A linear elastic model is used because the stress-strain curve of PDMS is essentially linear within small strains (Osullivan *et al.*, 2003). To further simplify the model, the dielectric layer adopts a planar structure with low Young's modulus and dielectric constant to approximate the pyramid structure. In addition, the bottom of the

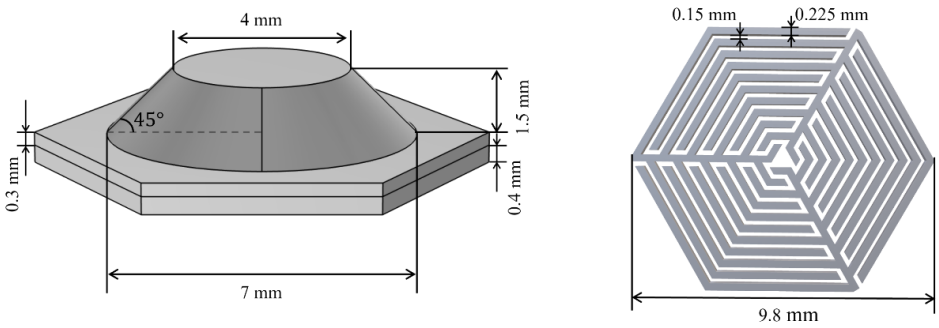

Parameters	**Contact layer**	**Dielectric layer**
Relative permittivity	10	3
Young's modulus	3e6 Pa	1e6 Pa
Poisson's ratio	0.49	0.49

Figure 4.4: Sensor dimensions and material parameters.

sensor is set as a fixed constraint, and the load is applied to the upper surface of the truncated cone in the form of three axial forces (F_x, F_y and F_z).

Due to the thinness of the electrode layer, the displacement changes of the contact layer and dielectric layer when subjected to external force are of interest. Figure 4.5 (a) is the displacement distribution of the sensor contact layer in the z-axis direction when the normal force is loaded ($F_x = 0$, $F_y = 0$, $F_z = -2N$). The cross-sectional view of the contact layer and the displacement distribution of the upper surface of the dielectric layer are shown in Figure 4.5 (b) and (c), respectively. The three inter-digital capacitors are indicated by the dotted box. As can be seen, the displacement distribution of the upper surface of the dielectric layer is centre-symmetric under normal force, implying that the three capacitor units are subjected to equal pressure.

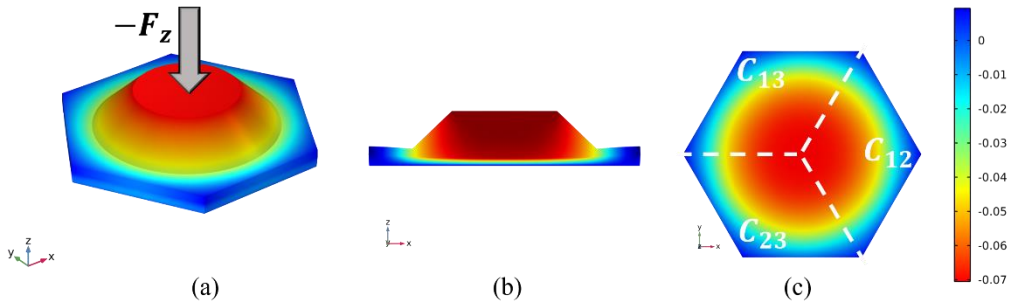

Figure 4.5: Displacement distribution under normal force. (a) 3D view. (b) Cross-sectional view of the contact layer. (c) Top view of the dielectric layer.

Figure 4.6 (a-c) depict the displacement distribution of the sensor contact layer and dielectric layer after loading shear force ($F_x = 10$, $F_y = 0$, $F_z = -2N$). Under shear force, the area in the shear direction is compressed and the opposite direction is tensed.

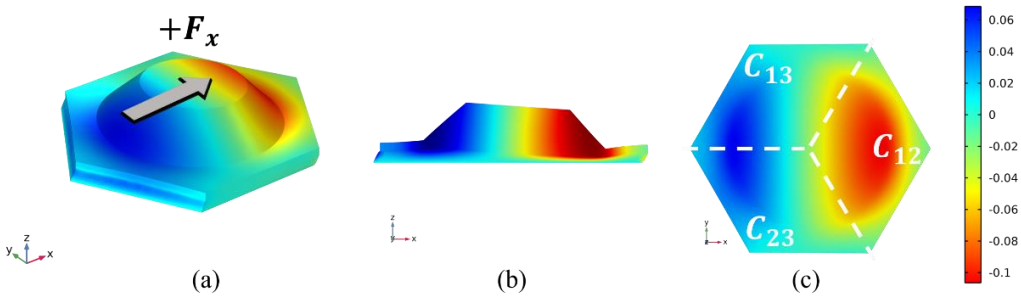

Figure 4.6: Displacement distribution under shear force. (a) 3D view. (b) Cross-sectional view of the contact layer. (c) Top view of the dielectric layer.

Figure 4.7 shows the capacitance changes of C_{12}, C_{13} and C_{23} under different forces. C_0 is the initial capacitance, ΔC is the capacitance change relative to C_0. The three capacitors exhibit the same change as the normal force increases. As aforementioned, the shear force alters the displacement of the dielectric layer in the opposite direction of the shear force. Therefore, the difference between C_{12} and C_{13} (C_{23}) is obvious, whereas C_{13} and C_{23} have similar changes because they are symmetrical about x-axis. It is worth noting that when the shear force is applied in the +x direction, a portion of C_{13} and C_{23} are also under pressure. This causes a slight increase in capacitance, but it is still significantly different from C_{12}.

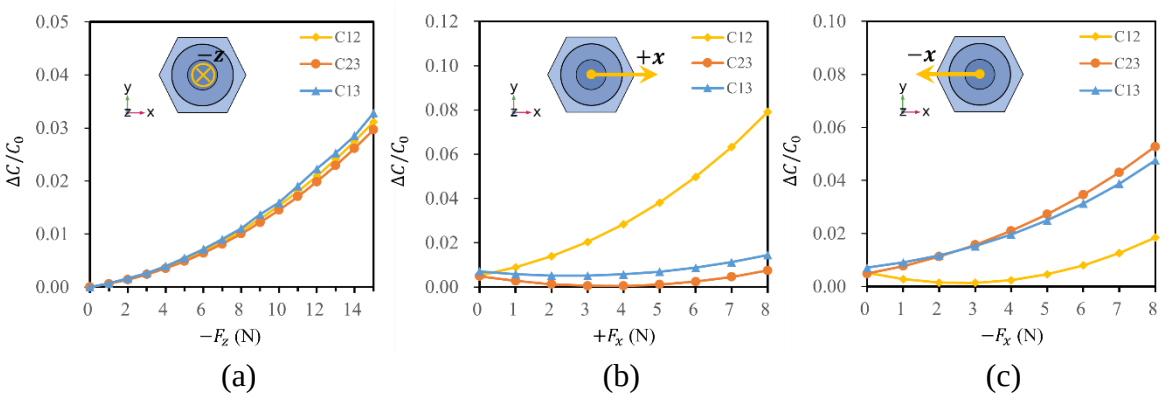

Figure 4.7: Simulation results of the capacitance change under different directional forces. (a) Normal force along the -z axis. (b) Shear force along the +x axis. (c) Shear force along the -x axis.

4.2.2 Determination of the structural parameters of the contact layer

The contact layer can transmit normal forces to the dielectric layer. Also, it can generate torque when subjected to shearing force, causing compressive and tensile deformation of the dielectric layers on both sides. Hemispheres (Huang *et al.*, 2017) and truncated pyramids (Yu *et al.*, 2016; Zhu *et al.*, 2018) are two common contact layer structures used in the literature. The truncated cone is used in this work, so that the same stress can be loaded in any direction.

The torque generated by the shear force is affected by the structure of the truncated cone. To select appropriate parameters, the influence of the height and inclination angle of the truncated cone on the shear force detection is investigated.

The normal force (F_z = -5N) and the shear force (F_x = 8N) are simultaneously applied to the surface of the truncated cone. As shown in Figure 4.7 (b), the variation of C_{12} is significantly higher than that of C_{23} and C_{13}. Here, the capacitance difference is used as the objective function to qualitatively characterise the effect of the truncated cone on shear force detection, which is defined as:

$$F_{diff}=C_{12}-\frac{(C_{23}+C_{13})}{2} \tag{4.1}$$

Under the same load, the larger the capacitance difference, the higher the sensitivity of the sensor to shear force. The objective function values are calculated with the inclination angle increasing from 30° to 65° (the height of the truncated cone is fixed at 1.5 mm). Similarly, set the inclination angle of the truncated cone at 45°, and calculate the objective function values when the heights are 1, 1.2, 1.4, 1.6, 1.8 and 2 mm, respectively. As shown in Figure 4.8, increasing the height and decreasing the inclination angle of the truncated

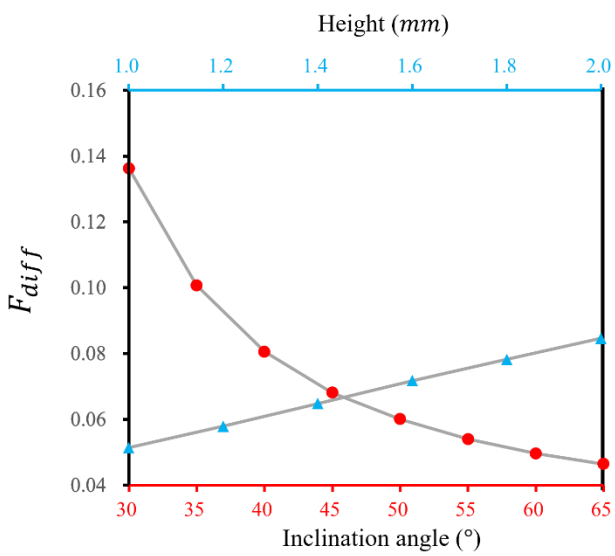

Figure 4.8: Objective function value as a function of the angle and height of the truncated cone.

cone can improve the sensitivity of shear force detection. In comparison, the angle of inclination has a greater influence than height.

In addition, the followings should be considered when the parameters of the contact layer are selected:

(1) According to the conclusion of Chapter 3 on the influence of the contact layer structure, the increase in the thickness and the inclination angle leads to a decrease in the normal force sensitivity of the sensor.

(2) Excessive contact layer thickness increases elastomer recovery time, resulting in a larger hysteresis error.

(3) Increasing the height of the truncated cone while maintaining the same inclination angle reduces the contact area, affecting sensor stability and increasing fabrication difficulty.

Finally, the truncated cone height, inclination angle and substrate thickness are chosen to be 1.2 mm, 30° and 0.3 mm, respectively.

4.2.3 Structural optimisation of the dielectric layer

To further improve the sensitivity of shear force detection, Lee *et al*. (2008) reported an air dielectric layer with a pillar in the middle, which can generate a large capacitance difference. Later, the pillar was replaced by a wall spacer to provide mechanical support and reduce the response time of the sensor (Lee *et al*., 2011). The air dielectric layer with spacers can significantly improve the sensitivity of the sensor to shear force and is a common structure for 3D force sensors (Chen *et al*., 2013; Chuang *et al*., 2016). However, when an excessive shear force is applied, the dielectric layer with a planar structure may

cause adhesion of the upper and lower layers, which affects the recovery time of the sensor.

Benefiting from the development of micro-nano-fabrication, the sensitivity of capacitive tactile sensors can be greatly improved by introducing micro-structure arrays in the dielectric layer. In addition to improving the sensitivity, the hysteresis and response time of the sensor can also be effectively tuned by changing the size and spacing of the micro-structures (Fan *et al.*, 2012; Luo *et al.*, 2018).

Inspired by this, the dielectric layer is optimised by varying the size and spacing of the inverted pyramid micro-structure. Figure 4.9 shows a cross-sectional view of the modified four dielectric layers, namely D1, D2, D3 and D4. This is for illustration of the structure only. The essence of optimisation is to change the equivalent Young's modulus of the dielectric layer above the electrode, so that a larger deformation occurs when it is subjected to shear force. As shown, the centre and surrounding areas of the dielectric layer are large and dense pyramids to provide mechanical support. Small-sized and sparse pyramids are used to implement the dielectric layers above the electrodes of D1 and D2. D3 and D4 are a combination of using small and sparsely arranged pyramids, with the

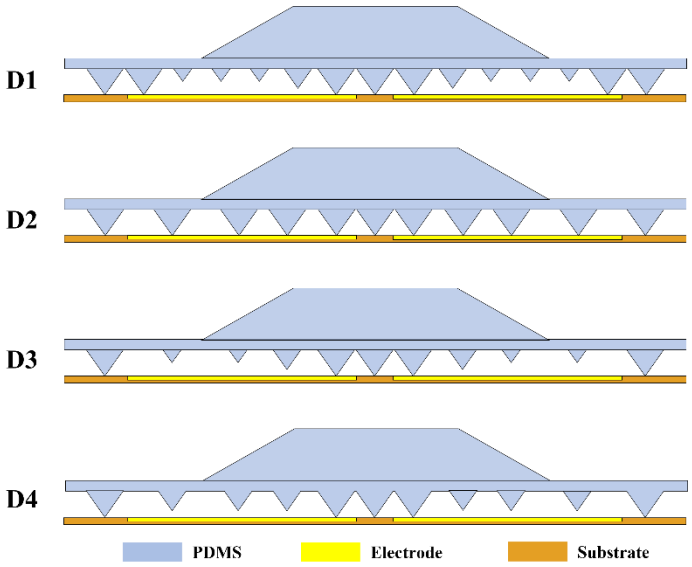

Figure 4.9: Schematic diagram of the modified dielectric layer structure.

difference being the size of the pyramid. A comparison of these four modified dielectric layers is given in the experimental section.

4.3 Sensor fabrication

For this sensor with hierarchical structure, this section studies and improves the layer-by-layer fabrication process as well as the assembly method. The specific processes involved in each step are described and discussed below.

4.3.1 Preparation of PDMS solution

Among flexible materials, PDMS has become the preferred substrate material for flexible electronic devices due to its low Young's modulus and excellent chemical stability (Xiang *et al*., 2012). The contact layer and dielectric layer of the designed sensor are prepared by using PDMS through mould casting.

The PDMS solution is usually prepared from resin and curing agent in a mass ratio of 10:1 to 20:1. The Young's modulus of cured PDMS decreases with the increase in resin ratio (Wang *et al*., 2015). As mentioned before, the main role of the contact layer is to transmit and concentrate external forces to increase the deformation of the dielectric layer. However, a highly flexible contact layer causes the consumption of external force, and only a small part of the external force is transmitted to the dielectric layer, resulting in a small change in the capacitance of the sensor. Therefore, the contact layer is prepared with PDMS with a mass ratio of 5:1 to reduce the loss of external force in the contact layer, while the mass ratio of PDMS used in the dielectric layer is 10:1 to ensure sufficient compressibility.

Dow Corning Sylgard 184 (Dow Corning, USA) is used in this work. The following are the PDMS formulation steps: The specific ratio of resin and curing agent is weighed into

a container based on the desired Young's modulus. Stir for 5 minutes with a magnetic stirrer or glass rod to ensure thorough mixing. Then, it is placed in a vacuum box for 30 min to extract the air bubbles mixed in the PDMS. All PDMS used in this experiment is prepared according to this procedure.

4.3.2 Preparation of the contact layer

The prepared PDMS solution is poured into a mould with a concave structure, and the contact layer is obtained by demoulding after curing. Given that the dimensions of the contact layer structure are on the millimetre scale, the required precision can be met using a 3D printed mould. The preparation process of the contact layer is shown in Figure 4.10, and the detailed process is described as follows:

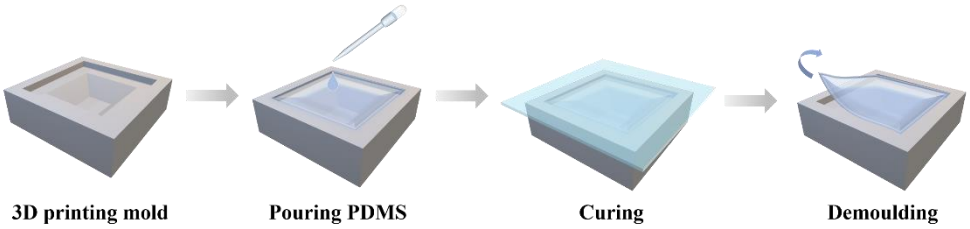

Figure 4.10: Preparation process of the contact layer.

(1) To prevent PDMS from sticking to the mould, treatment is carried out before the mould is used. Specifically, the mould is immersed in a mixed solution with a mass ratio of detergent: ethanol = 1:10 for ultrasonic cleaning for 30 minutes. Then it is put in a 70 °C box until dry.

(2) Drop 0.5 ml of PDMS solution with a mass ratio of 5:1 onto the mould. Tilting the mould allows PDMS to completely fill all concave structures. Vacuum for 20 mins to remove air bubbles generated during PDMS pouring.

(3) Squeeze out the excess PDMS solution by covering the mould with PET film and a glass slide. Place a 500 g weight on it to ensure good contact between the PET film and the mould, then dry it for 5 hours at 60 °C.

(4) Carefully peel off PDMS from PET and heat for 1 hour at 100 °C to increase hardness.

4.3.3 Preparation of dielectric layer

Since the dimensions of the pyramids in the dielectric layer are on the order of micrometres, a silicon mould made by photolithography and etching techniques is used. However, the cured PDMS has strong adhesion to the silicon mould, and so it is difficult to separate it from the silicon mould. Therefore, how to fabricate high-precision silicon mould and complete demoulding are two key issues for preparing dielectric layers.

4.3.3.1 Fabrication of silicon mould

Photolithography and etching techniques are commonly used to fabricate high-precision moulds. The entire process includes silicon wafer photolithography, dry etching with photoresist as a mask, and anisotropic wet etching with an oxide layer as a mask.

Mask design and photolithography

Photolithography is the technique of transferring patterns on a mask onto a silicon wafer, which is the preferred method of micro-fabrication with sub-micron precision (Yang *et al.*, 2019; Ruth *et al.*, 2020). The precision of the mask has a significant impact on lithography quality. The mask used is a silicon dioxide glass substrate with chromium thin film deposited by magnetron sputtering. The precision of the mask reaches 1 μm, which fully meets the precision requirements. Different arrays are designed on a single 4-inch silicon wafer, so that multiple pyramid dielectric layers can be obtained in one process. Figure 4.11 shows the designed mask layout and its enlarged view, where the

array of white squares represents the exposed area and the black area represents the unexposed chrome film.

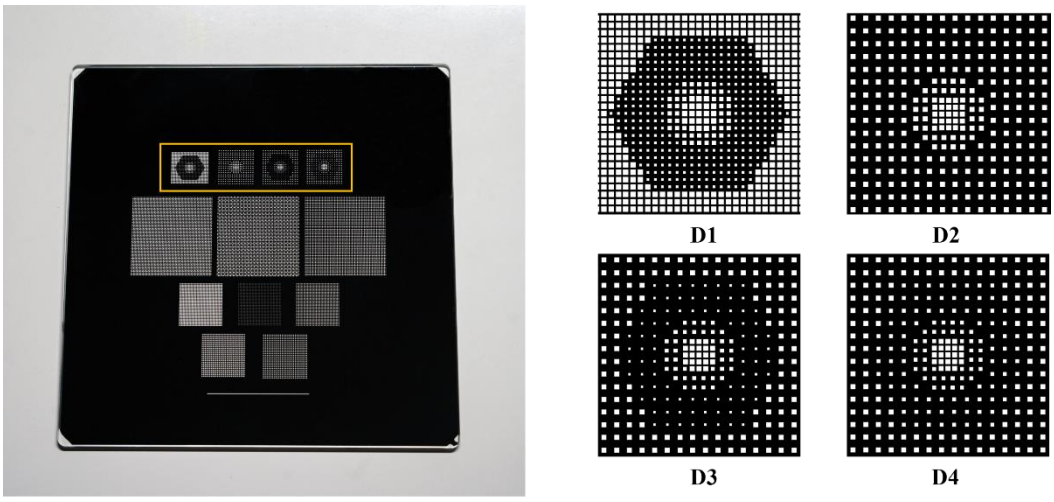

(a) (b)

Figure 4.11: Mask design. (a) Photograph of the actual mask. (b) Mask layout of the four dielectric layers.

The purpose of photolithography is to transfer the geometric design from the mask to the photoresist by exposing and developing. Figure 4.12 shows the key process of photolithography. The detailed steps are:

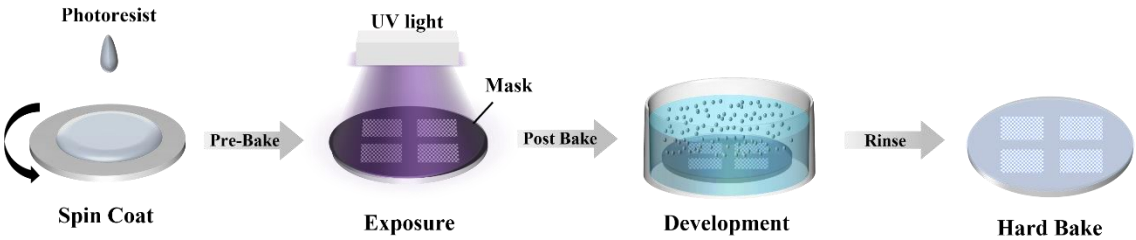

Figure 4.12: The process flow of photolithography.

(1) A 4-inch (100) orientated silicon wafer covered with a 500 nm thermally grown oxide is immersed in acetone and ethanol solution for 5 minutes each for ultrasonic cleaning. Blow dry with nitrogen and bake on a heated plate at 100 °C for 10 minutes to remove moisture.

(2) A positive photoresist with a thickness of 50 um is spin-coated on the wafer. First spin at 500 rpm for 20 s to ensure that the photoresist completely covers the surface of the

silicon wafer. Then spin at 3000 rpm for 20 seconds. 10-minute rest is allowed to eliminate ripples caused by spin coating.

(3) Pre-baking is used to remove excess solvent and improve adhesion between the photoresist and the silicon wafer. To prevent wrinkling of the photoresist, the temperature is gradually increased from 50 °C to 110 °C with a 20 °C gradient and held at each temperature for 2 minutes.

(4) The wafer is exposed to light through a mask. Contact exposure has higher resolution than proximity exposure, and the equipment is simpler than projection exposure. However, contact exposure requires the mask to be pressed against the surface of the photoresist. The exposed pattern after multiple uses may have burrs and deformation due to the residue of the photoresist. Considering that the mask is used only a few times in this work, contact exposure is finally used.

(5) The post-exposure baking is to volatilise the solvent inside the photoresist, increase the hardness of the photoresist, and improve the resolution of pattern.

(6) Put the silicon wafer into the positive developer, drag the silicon wafer with tweezers and shake it for 1 minute to dissolve and remove the photosensitive positive gel. Then, the wafer surface is cleaned with absolute ethanol, and then dried with nitrogen gas.

(7) Place the developed wafer on a heated plate, increase the temperature from 50 °C to 120 °C, and hold at 120 °C for 10 minute. The purpose of the hard bake is to volatilise the developer and improve the adhesion of the photoresist.

Finally, the pattern on the mask is successfully transferred to the surface of the silicon wafer.

Dry and wet etching

Etching refers to the selective etching of semiconductor substrates or oxide layers, including wet etching and dry etching. The surface of the silicon wafer not covered by the photoresist is etched away to obtain the desired concave structure. Wet etching is a method of chemical etching by immersion in an etching solution. While dry etching uses plasma for physical and chemical etching, it has higher resolution than the former.

The principle of creating pyramid concave structures on silicon wafers is based on the anisotropic nature of silicon etching with an alkaline etchant. The etching rate is affected by crystal orientation. When the photoresist surface is aligned with the (110) crystal plane, the (100) crystal plane has the highest etching rate, while the (111) crystal plane has the lowest. As shown in Figure 4.13, the final etched shape is a V-groove or inverted pyramid structure with the (111) crystal plane as the boundary. In theory, the included angle of the etched groove is 54.74 °, which is the angle between the (111) and (100) crystal planes.

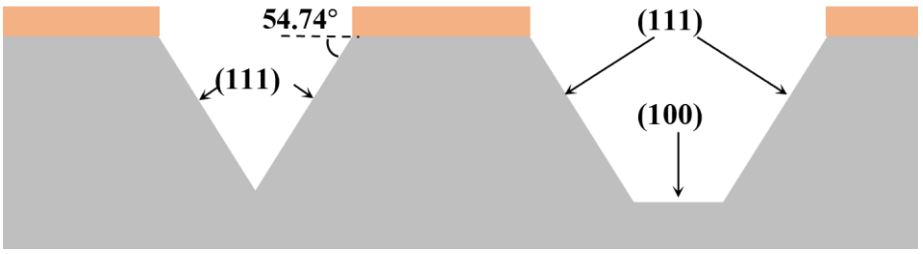

Figure 4.13: Wet etching principle.

Following development, the SiO_2 layer in the corresponding area of the square matrix is exposed, and the remainder is covered with patterned photoresist. Wet etching with photoresist as a mask is straightforward, but it cannot meet precision requirements because the photoresist's edges may be etched. As a result, a combination of dry and wet etching is employed. The key steps are illustrated in Figure 4.14:

(1) Dry etching of SiO_2 with patterned photoresist as a mask.

(2) Remove the photoresist from the surface in acetone and ethanol solution.

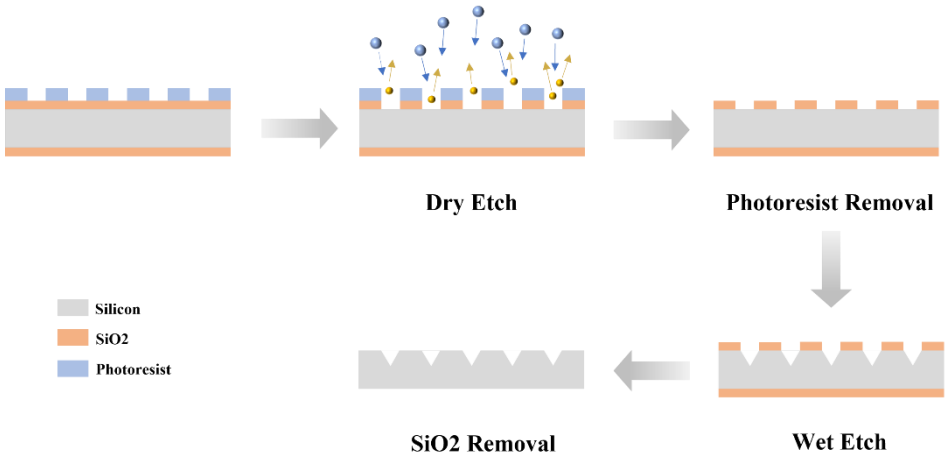

Figure 4.14: Process flow of dry and wet etching.

(3) Anisotropic wet etching of Si with 30 wt% potassium hydroxide (KOH) for 3 hours at 80 °C with patterned SiO_2 as a mask. Stir the solution to remove impurities and air bubbles created during the etching process.

(4) Remove SiO_2 from the surface of the silicon wafer in buffered oxide etch (BOE) (NH4F: HF=6:1) for 60 minutes. The cleaned and dried silicon mould is shown in the Figure 4.15.

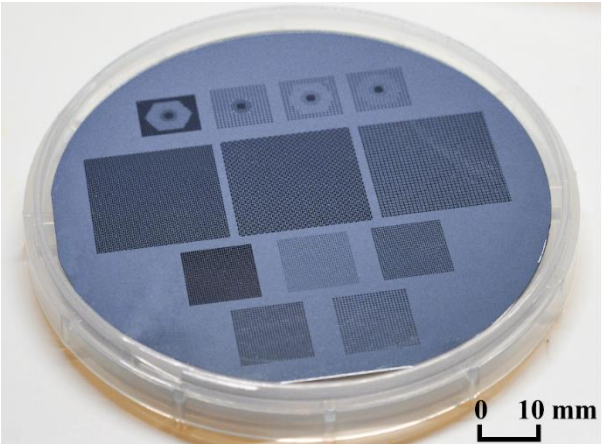

Figure 4.15: The prepared silicon mould.

4.3.3.2 Casting of PDMS dielectric layer

The cured PDMS is difficult to peel from the silicon mould without surface modification. Silanization is a surface modification method used to reduce the surface energy of silicon.

The modified silicon mould has a super hydrophobicity surface, and so PDMS can be easily removed from it (Yang *et al.*, 2019).

The modifier used in this work is 1H, 1H, 2H, 2H-perfluorooctyltrichlorosilane (PFOCTS) and vapour deposition method is employed for treating the surface of the silicon mould. Compared with the liquid phase method, the vapour deposition method requires less time and dosage (Psarski *et al.*, 2012). Figure 4.16 shows the silanization process of silicon mould. The detailed steps are as follows:

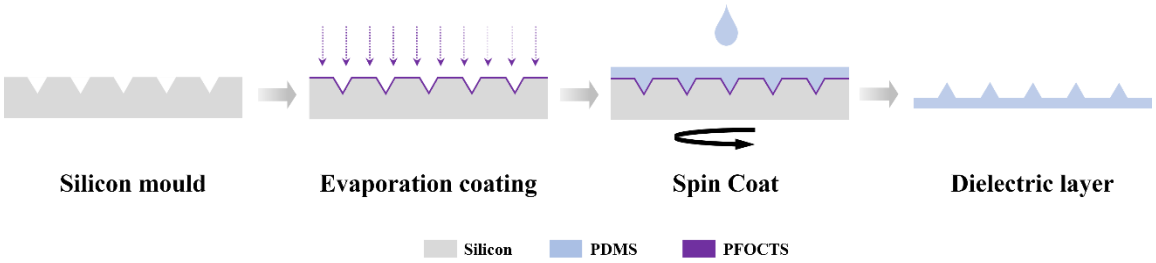

Figure 4.16: Silanization of silicon mould.

(1) Put the silicon mould in acetone and ethanol for ultrasonic cleaning for 10 minutes respectively.

(2) Put the silicon mould and 0.2 ml of PFOCTS into a vacuum box for 4 hours. After liquefaction, a uniform hydrophobic film is formed on the surface of the silicon mould.

(3) PDMS is prepared with a ratio of resin to curing agent = 10:1. Cast evenly on silicon mould and spin-coat at 500 rpm for 60 seconds. It has been confirmed by many attempts that this parameter can obtain a film with a thickness of about 200 μm.

(4) Degas the silicon mould under vacuum for 30 minutes to eliminate air bubbles so that PDMS can completely fill the micro-structure of the silicon mould.

(5) After heating at 70 °C for 3 hours to fully cure, carefully peel off the PDMS from the silicon mould. The prepared dielectric layer with a pyramidal micro-structure is shown in Figure 4.17.

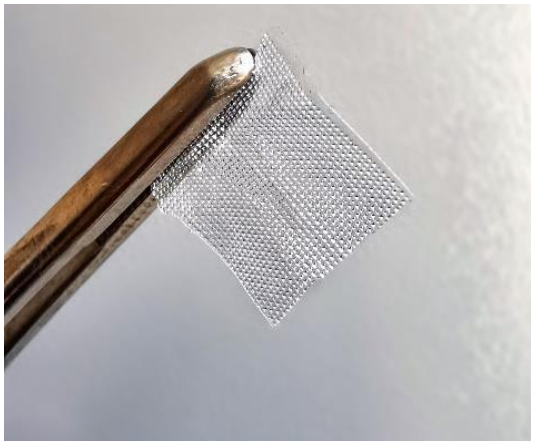

Figure 4.17: The prepared PDMS dielectric layer.

4.3.4 Preparation of electrode layer

Flexible electrodes are usually fabricated by photolithography and noble metal deposition. Considering the manufacturing cost, the electrode layer in this work is a flexible PCB made of polyimide (PI) as the substrate. The double-layer structure simplifies the wiring arrangement. In addition, flexible PCB has good compatibility to provide stable connection for both soft and hard modules.

To reduce interference, a ground shield is placed on the bottom layer of the wires and electrodes. A double-sided flexible PCB with a thickness of 0.2 mm is used to ensure the flexibility. Figure 4.18 shows the front and back layout of the designed square spiral electrode. The wire width is 0.1 mm and the electrode width is 0.3 mm. Each single electrode is connected to external circuit through a gold finger.

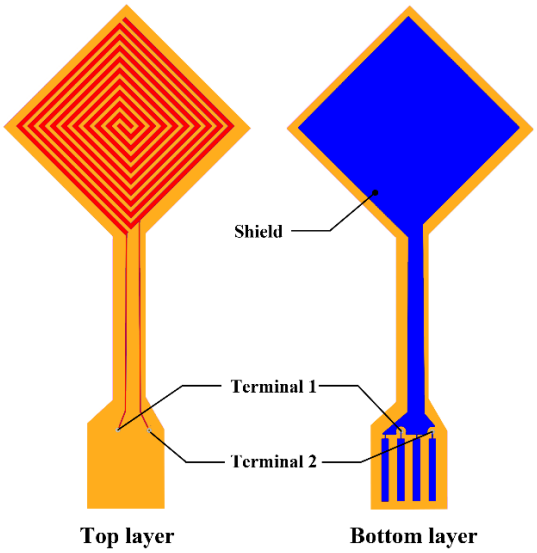

Figure 4.18: PCB diagram of electrode layer.

4.3.5 Integrated packaging of sensor

So far, the contact layer, dielectric layer and electrode layer of the sensor have been prepared. Interlayer integration of tactile sensors is achieved using partially cured PDMS which has a high viscosity. To ensure the functionality of the micro-structure of the dielectric layer, the thickness of the spin coated PDMS film should be less than 1 μm. Therefore, PDMS with the mass ratio of elastomer: curing agent: n-hexane=20:1:20 is prepared. After spin coating on the electrode layer at 8000 rpm for 90 seconds, a PDMS film with a thickness of less than 1 μm can be formed on the electrode surface. As shown in Figure 4.19, the three-layer structure is bonded together by semi-cured PDMS. In addition, a 500 g weight is placed on top and cured at room temperature for 12 hours. After fully curing, remove the weight and put it at 100 °C for 1 hour to improve the bonding strength.

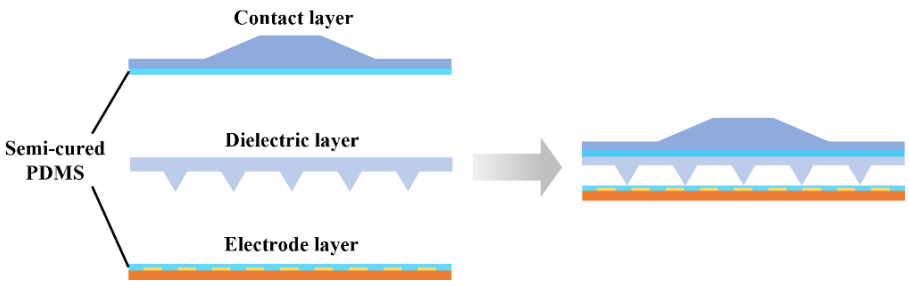

Figure 4.19: Experiment setup for testing capacitive tactile sensor.

4.4 Experimental evaluation

4.4.1 Experiment setup

A test platform is built for performance evaluation, which consists of a 3D force loading platform and a capacitance acquisition system. A high-precision load cell (ELS 50, Mecmesin) is used to load the vertical pressure through the motorised test stand (MultiTest-dV(u), Mecmesin). As shown in Figure 4.20 (a), the tactile sensor is attached to the surface of an adjustable angle gauge. The force gauge is driven to apply a vertical force F, which is decomposed into a normal force F_z and a shear force F_s. F_z and F_s can be expressed as:

$$F_z = F \cdot \cos(\alpha) \tag{4.2}$$

$$F_s = F \cdot \sin(\alpha) \tag{4.3}$$

where α is the angle between the total force F and the normal force F_z.

The direction of the shear force is determined by β, which is the angle between F_s and the central axis of the capacitor C_{12}, as shown in Figure 4.20 (b). In this way, normal force and shear force of different magnitudes and directions can be applied by adjusting α and β.

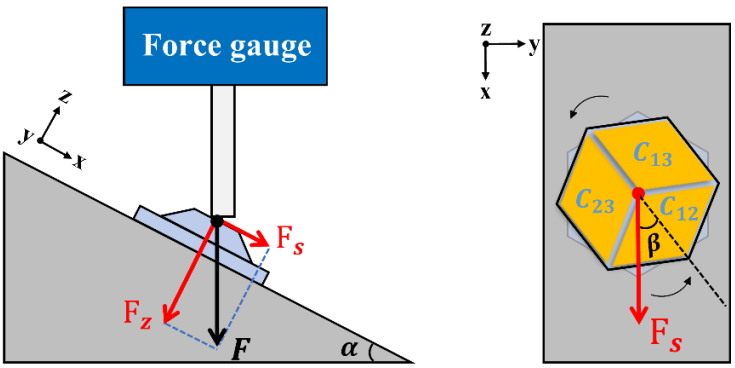

(a) (b)

Figure 4.20: Schematic diagram of the experiment setup and force decomposition.

A schematic diagram of the capacitance measurement system is shown in Figure 4.21. Capacitance is acquired by a capacitance-to-digital converter (CDC) (AD7150, Analog Devices, USA) with a sensitivity of up to 1 fF, which meets the measurement of this sensor. Since the designed tactile sensor contains three capacitors, a multiplexer is employed to expand the limited channels of the AD7150. The two electrodes to be measured are connected to CIN and EXC of the AD7150 respectively, and the remaining electrode is grounded. In addition, a grounded shield is placed on the back of the sensor to reduce parasitic capacitance and improve SNR. The microprocessor based on 32-bit CortextM3 core establishes communication with AD7150 through I^2C and uploads the collected capacitance data to a PC for further data processing.

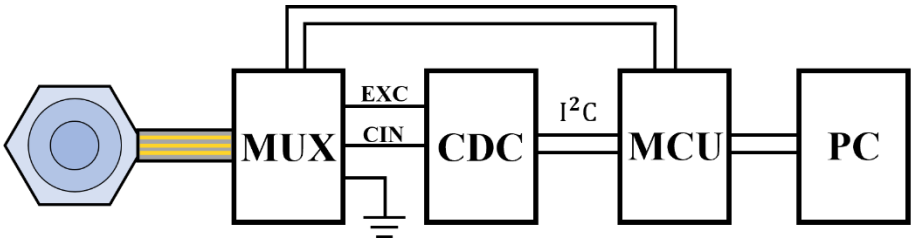

Figure 4.21: schematic diagram of the capacitance measurement system.

Figure 4.22 (a) shows the capacitance acquisition circuit with a dimension of 43 mm × 59 mm. This circuit contains a total of 9 channels, only three of which are used in this experiment. Figure 4.22 (b) shows the fabricated 3D force sensor.

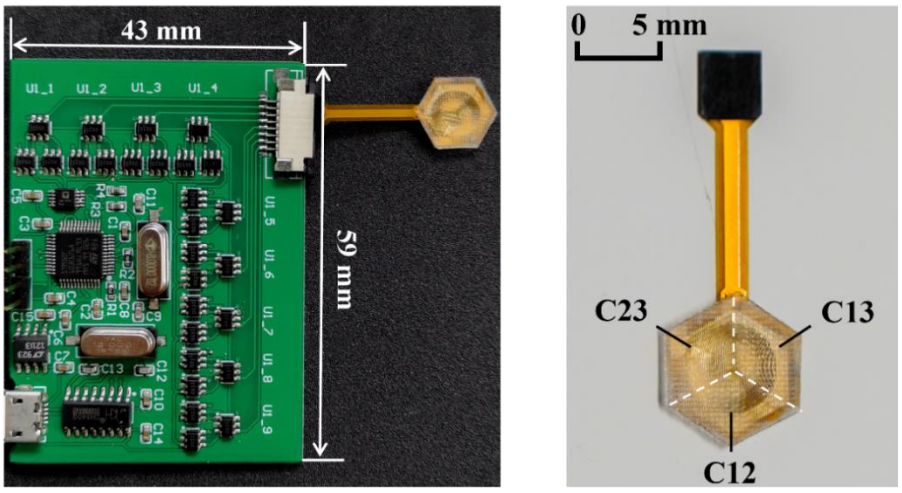

(a) (b)

Figure 4.22: Photographs of measurement circuit and sensor. (a) Capacitance acquisition circuit. (b) The fabricated 3D force sensor.

4.4.2 Sensor characterisation in optimised dielectric layer structures

In this section, the effect of the optimised dielectric layer structure on the sensitivity of the sensor is demonstrated. The uniformly distributed dielectric layer structure is used as a comparison.

A normal force of 0-5N is applied to the sensor. To reduce measurement error, the average value of five loading experiments was recorded as the final result. Figure 4.23 (a–e) shows the output characteristics of the five sensors. The three capacitances increase monotonically with applied force, but the sensitivity changes differ from the simulated results. This is because the dielectric layer in the simulation is simplified as a planar structure, whereas the Young's modulus of the micro-structured dielectric layer increases with pressure, resulting in a decrease in sensor sensitivity.

In theory, the three capacitors should have the same capacitance change. However, errors may be introduced due to uneven force loading, fabrication process, and measurement. As a result, the average of the three capacitances is used to compare the effect of dielectric layer optimisation on sensitivity. As shown in Figure 4.23 (f), with the optimised dielectric layer, the sensitivity of the sensor at low pressures is significantly improved. Within 0-1N, the sensitivity is 1.16 N^{-1}, 0.79 N^{-1}, 1.25 N^{-1} and 0.92 N^{-1}, respectively, which is 2-3 times higher than that of the sensor with uniformly distributed dielectric layer (0.45 N^{-1}).

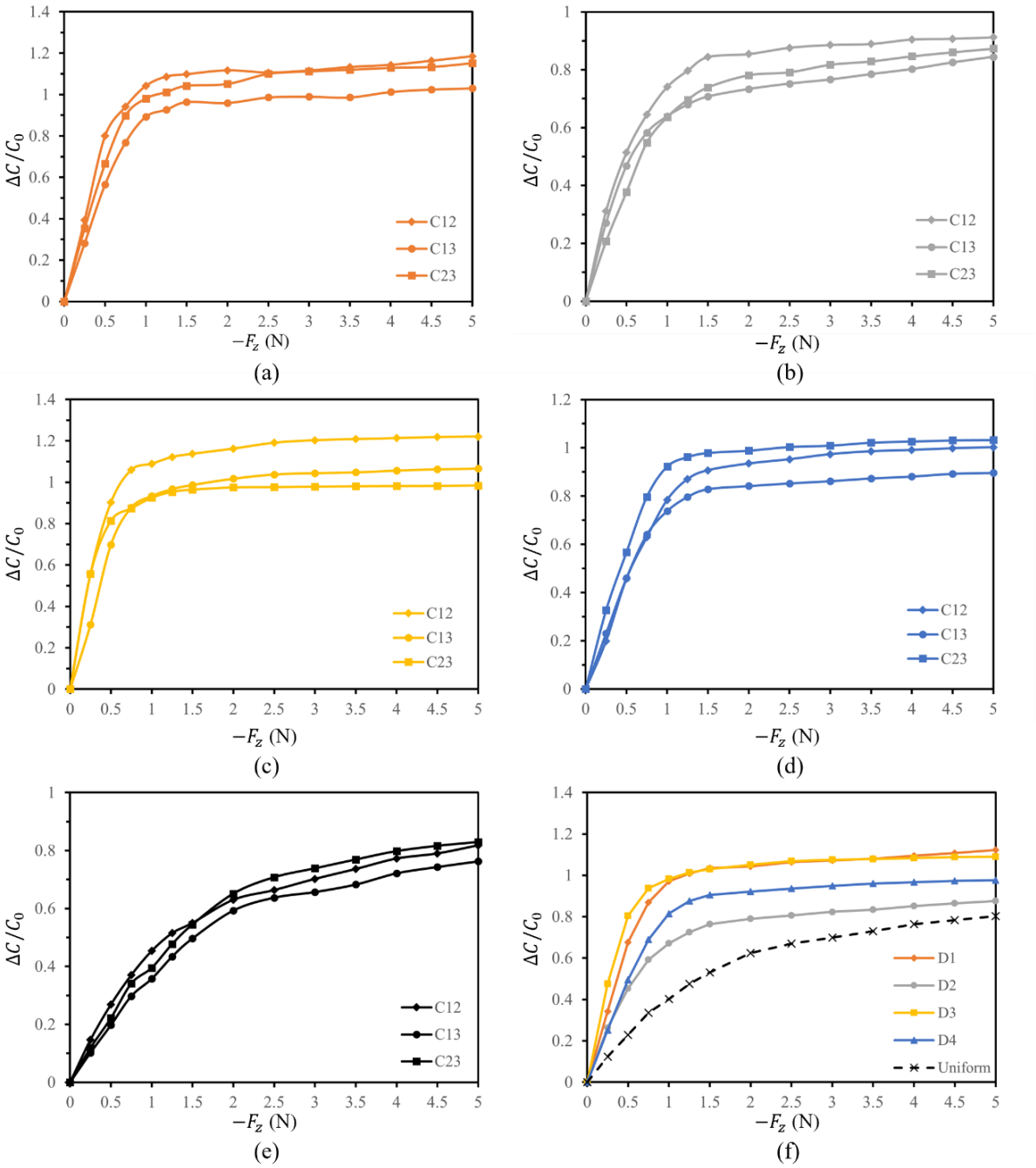

Figure 4.23: Characterisation of sensor under normal force with (a) D1, (b) D2, (c) D3, (d) D4, (e) Uniform distributed dielectric layer. (f) Comparison of average capacitance values for different dielectric layers.

Figure 4.24 (a-c) compare the three capacitances when sensor is subjected to force in an oblique direction ($\alpha = 45°$, $\beta = 0°$). The applied pressure range is 0-2N, and the shear force component and the normal force component are theoretically equal. As can be seen, the capacitance of C_{12} increases significantly due to compression, while the capacitance of the other two capacitors decreases slightly due to tension, which is consistent with the

simulation results. As the normal force component increases, C_{13} and C_{23} show an increasing trend. In addition, the objective function F_{diff} is calculated by Equation 4.1 to qualitatively compare the effects of different dielectric layer structures on the shear force sensitivity, as shown in Figure 4.24 (d). As expected, optimising the dielectric layer can increase the capacitance difference along the shear force direction. Among them, the sensor with D3 dielectric layer has the highest sensitivity to shear force.

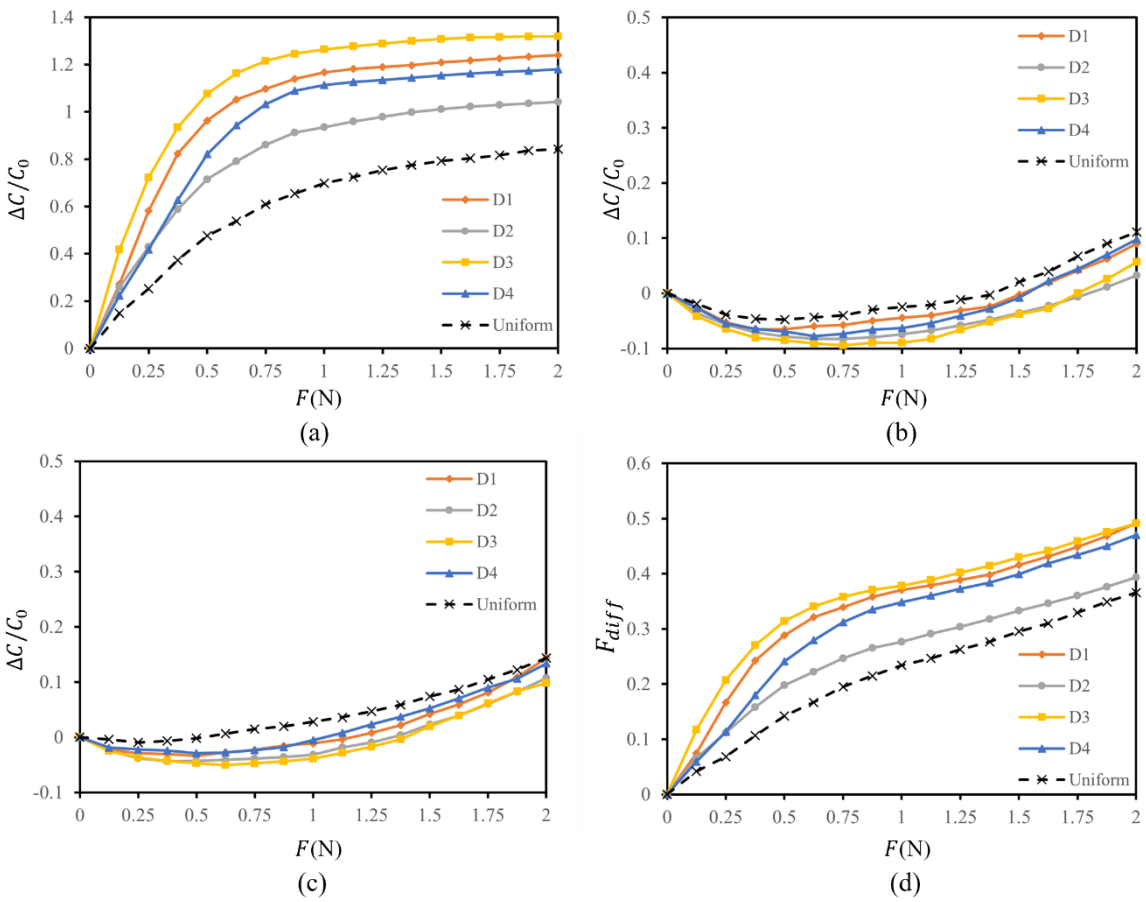

Figure 4.24: Comparison of (a) C_{12}, (b) C_{13}, (c) C_{23} and (d) objective function values for sensors with different dielectric layers.

4.4.3 Multi-directional force sensing performance evaluation

The response of the sensor made of the modified dielectric layer D3 under forces in different directions is measured. First, the shear force angle β is fixed at 0°, and the α is adjusted by angle gauge from 0° at 10° intervals until 60°. Taking 30° and 60° as examples, the test results are shown in Figure 4.25. Because the shear force component

increases with α, the sensitivity of C_{12} with α = 60° is higher than that of C_{12} with α = 30°. This feature also applies to C_{13} and C_{23}. At the beginning of force loading, there is a visible reduction in C_{13} and C_{23} due to the tensile force with α = 60°. While in the case of α = 30°, C_{13} and C_{23} are dominated by the normal force component. Therefore, C_{13} and C_{23} increase slightly with increasing force.

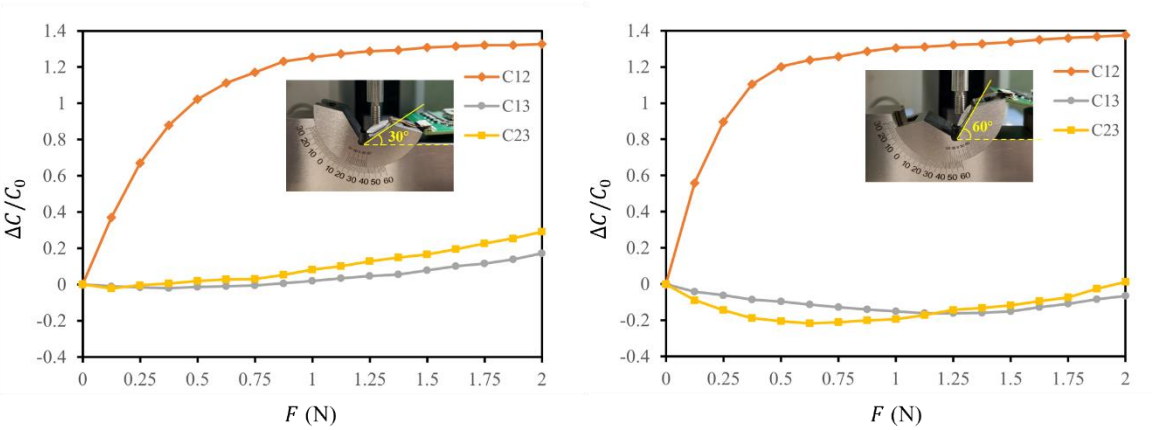

(a) (b)

Figure 4.25: Capacitance change as a function of force with (a) α=30° and (b) α=60°.

Figure 4.26 shows three capacitance variations as a function of α under different magnitudes of force. It can be seen that the three capacitances vary monotonically with α. And C_{12} is positively correlated with α, while C_{13} and C_{23} are negatively correlated with α. Therefore, the difference between C_{12} and C_{13} (C_{23}) becomes larger as the α increases. In addition, the capacitance change is approximately linear with α when the force is within 0.6 N, because C_{12} has a higher sensitivity when the force is

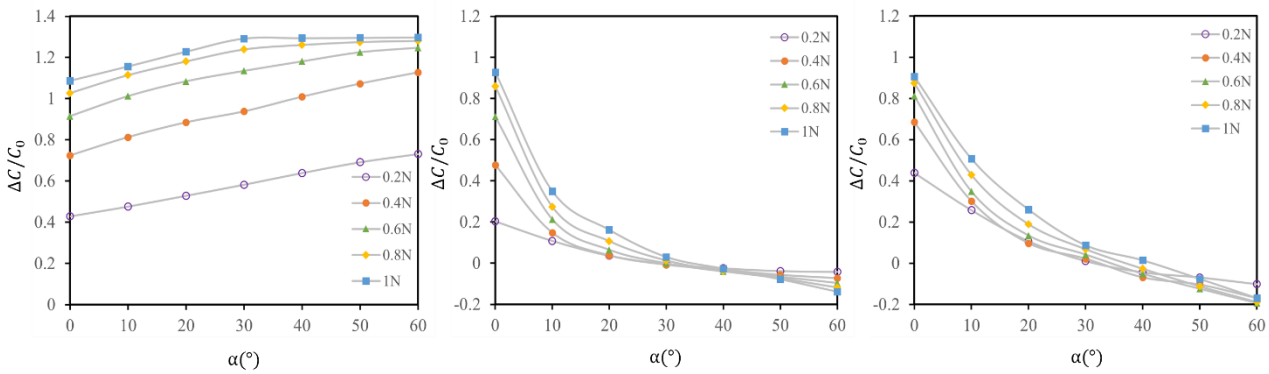

(a) (b) (c)

Figure 4.26: Capacitance change of (a) C_{12}, (b) C_{13} and (c) C_{23} as a function of α under different magnitudes of force.

small. In contrast, C_{13} and C_{23} exhibit a more pronounced difference in α under large force. From another point of view, with the increase in α, the changes of C_{13} and C_{23} under different magnitudes of force are very small. Therefore, it is difficult to infer the magnitude of the force based on the capacitance value alone.

Next, α was fixed at 30°, and the effect of β on the output of the sensor was evaluated. Considering the symmetrical structure of the sensor, 0°, 30° and 60° are typical angles for β. Figure 4.27 shows the capacitance change with β equal to 30° and 60°, respectively. Comparing the results shown in Figure 4.25 (a) with β = 0°, the rotation of the shear component increases the area under pressure for C_{13} and decreases the area under pressure for C_{12} and C_{23}. Therefore, the capacitances of C_{12} and C_{23} decrease, while the capacitance of C_{13} increases. In particular, with β = 60°, C_{12} and C_{13} are theoretically subject to the same pressure, their capacitance changes are similar to each other, and C23 reaches the minimum due to the reverse tension.

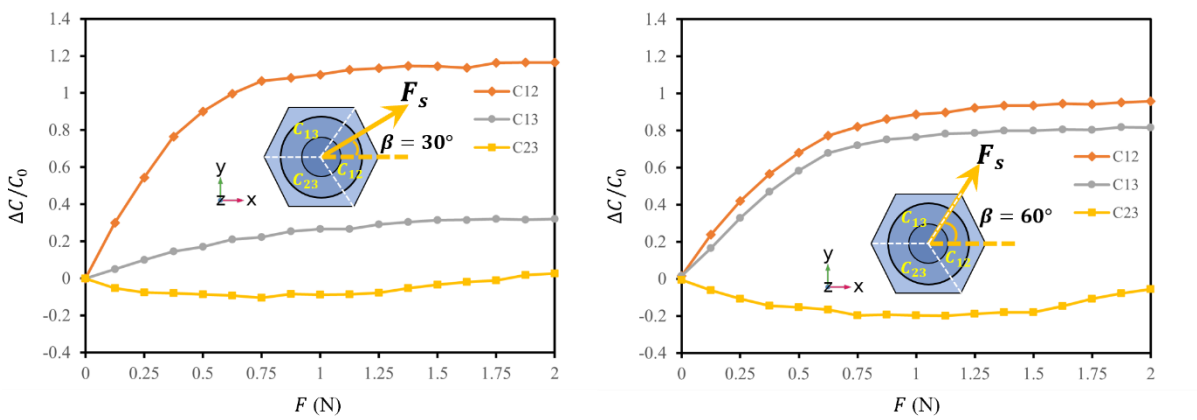

(a) (b)

Figure 4.27: Capacitance change as a function of force with (a) β=30° and (b) β=60°.

The changes in the three capacitances were further evaluated for different shear force angles (β). As shown in Figure 4.28, with force = 1 N, the three capacitors reach peaks and valleys alternately in one cycle (from -60° to 300°), and the phase difference between each adjacent peak/valley is 120°. For example, when β =0°, C_{12} is subjected to the

maximum stress and its capacitance value reaches the maximum. When β changes from 0° to 180°, C_{12} reaches its minimum value. The same phenomenon can be observed for C_{13} and C_{23}. Obviously, the shear force direction (β) can be uniquely identified based on the regularity of the three capacitance changes.

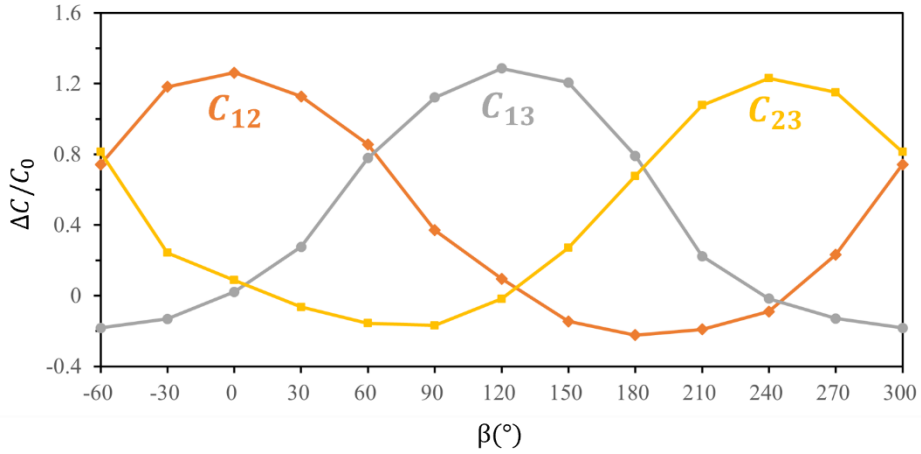

Figure 4.28: Capacitance change as a function of β at force = 1N.

The force along the -z axis, +x axis, -x axis, +y axis and -y axis was sequentially applied to the contact layer of the sensor by a finger, and the changes of the three capacitances are shown in Figure 4.29. Although the capacitance reduction caused by tension is small, the direction of the force applied to the sensor can still be identified by the capacitance change. Because the sensor is based on capacitance, the proximity of the finger can cause the capacitance change. As indicated by the red circle in Figure 4.29, when the finger approaches the sensor surface, the capacitance decreases. When the finger is far away, the capacitance returns to the initial value. Using this feature, the sensor can predict the distance and even the orientation of the target before contact, providing real-time feedback for a robot to achieve dexterous manipulation.

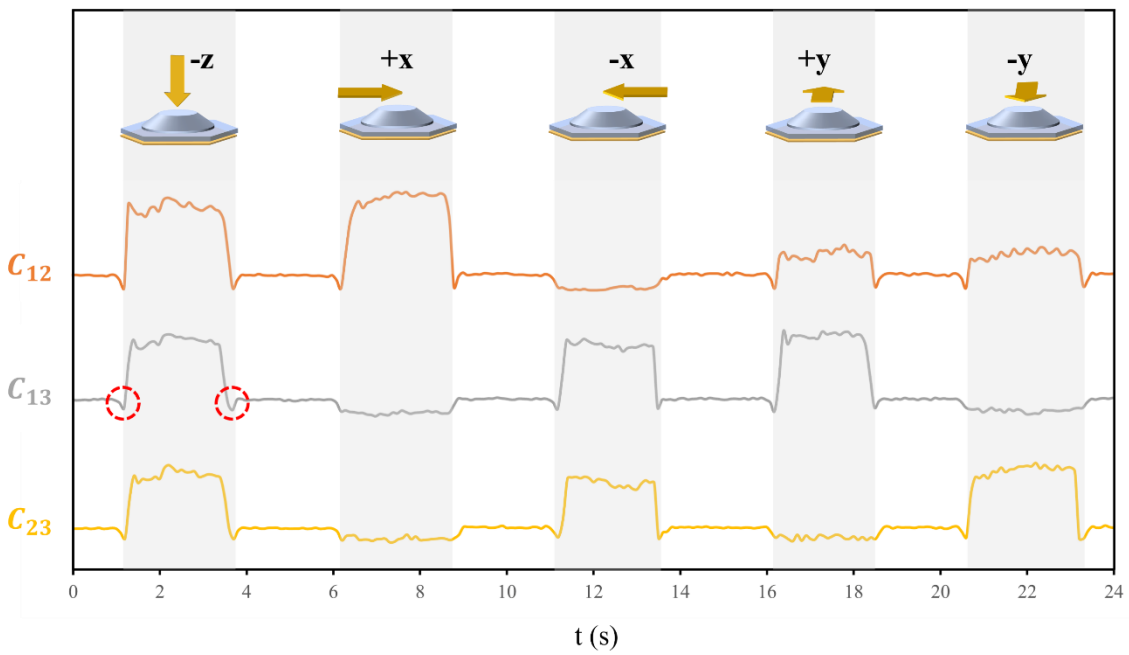

Figure 4.29: Characterisation of the multidirectional force sensing performance of the sensor.

4.5 Summary

This chapter proposes a new design of a multi-directional force tactile sensor. The design of three interdigitated electrodes is proposed for the first time to achieve multi-directional force detection with a minimum number of electrodes. This simplifies the sensor structure and facilitates the array design of the sensor. The arrangement of the micro-structure of the dielectric layer is modified to further improve the measurement sensitivity of shear force. In addition, a general and efficient fabrication process of flexible tactile pressure sensor is provided. Finally, a 3D force-loading platform and a custom capacitance measurement system are built to characterise and test the designed sensor. The experimental results show that the developed capacitive tactile sensor is capable of multi-directional force detection as well as proximity detection, which has a promising application in robotics.

Chapter 5 Optimal design of dual-function distributed capacitive tactile sensor

In the previous chapter, it has been verified that the designed planar capacitive tactile sensor has excellent performance, such as high sensitivity, high stability and fast response. However, the tactile information provided by a single tactile sensor is limited, which may not meet the needs of many scenarios, such as robotic skin and human-robot interaction. This chapter expands the previous single tactile sensor into an 8×8 array. The structure of dielectric layer and the contact layer are further optimised to improve the sensor performance and facilitate mass production. The dual functions of tactile sensing and proximity sensing can be realised under the same sensor structure. With this feature, this sensor is expected to be used in the fields of robot skin and human-computer interaction interface.

5.1 Sensor design

The designed distributed tactile sensor consists of 64 tactile sensing units. As shown in the inset in Figure 5.1, each sensing unit has a three-layer structure of electrode layer with spiral electrode pair, dielectric layer with micro-structures and contact layer. When an external force acts on the tactile sensing array, the capacitance of the sensing unit at the

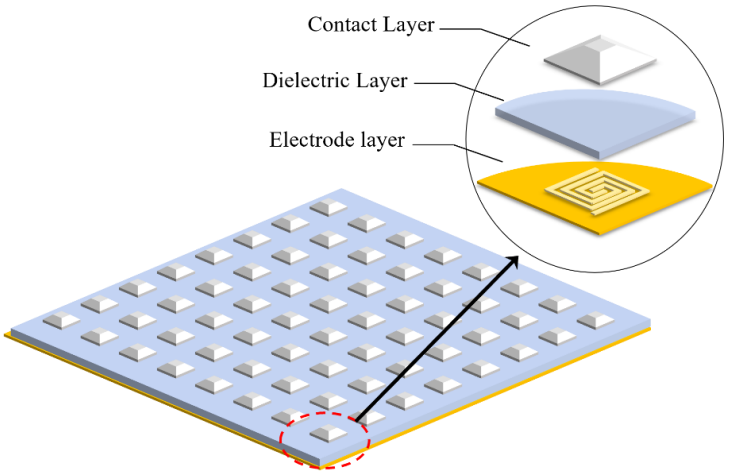

Figure 5.1: Schematic diagram of the designed distributed tactile sensor.

corresponding position increases. By measuring the capacitance changes of all sensing units, both the magnitude and location of the external force can be inferred.

5.1.1 Electrode arrangement

The electrode arrangement methods of tactile sensing array can be classified into three types, namely independent electrode array, common electrode array and orthogonal electrode array.

Independent electrode array: Two electrodes of each sensing unit are drawn out separately. Since each sensing unit is independent, the interference of electrical signals with each other is minimised. However, this method has high requirements on the measurement circuit. For an M×N sensing array, a total of 2×M×N wires are required.

Common electrode array: Only one electrode of each sensing unit is drawn out individually and the other electrodes are all connected in series as a common electrode. For an M×N array, there are (M×N +1) wires in total, which can save nearly half hardware interface compared to the former, but inevitably introduces more parasitic capacitance.

Orthogonal electrode array: The two electrodes are connected in series by the row and column where the sensing unit is located. In that case, the number of required wires is reduced to (M+N), which is widely used in many types of array sensors.

In this work, an orthogonal electrode arrangement is used. Figure 5.2 (a) shows the equivalent circuit diagram for a 4×4 array. A spiral electrode is formed at the intersection of each row and column, as shown in Figure 5.2 (b).

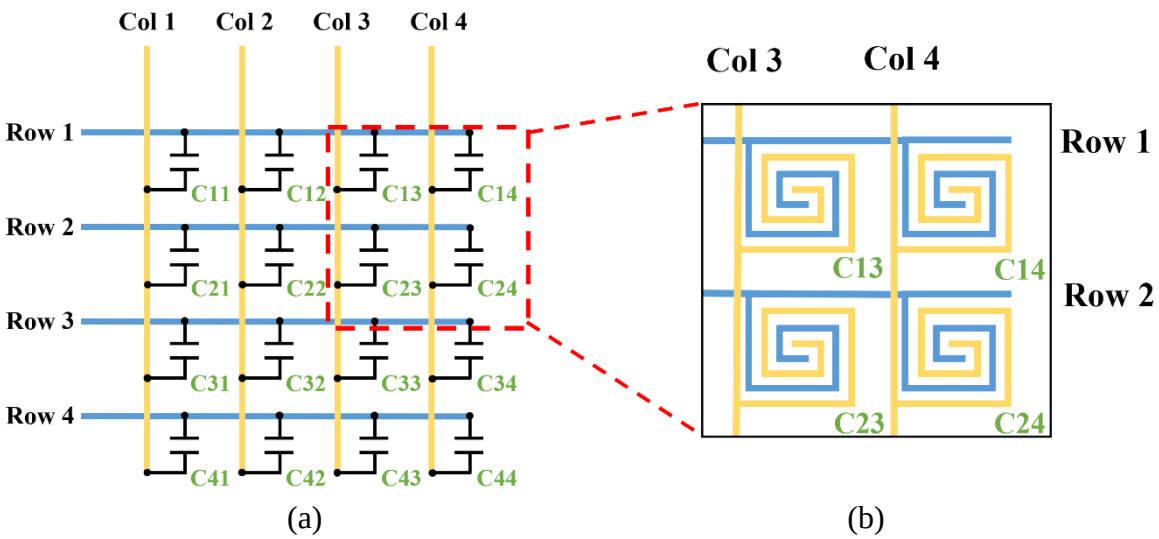

Figure 5.2: Orthogonal electrode array. (a) Equivalent circuit diagram of a 4x4 array, (b) Partial schematic diagram of the electrode array.

5.1.2 Finite element simulation of dielectric layer micro-structure

The mechanical properties of the dielectric layer micro-structure are the key factors affecting the performance of capacitive sensors. Tee *et al.* (2014) reported that the sensitivity of the sensor can be tuned by changing the side inclination angle and separation distance of the pyramidal structure of the dielectric layer. However, high-sensitivity tactile sensors typically have a small measurement range. In this subsection, the structural parameters of the micro-structure are optimised through finite element simulation with the goal of balancing the sensitivity and measurement range of the sensor.

This work adopts a truncated pyramid, which can achieve good stability despite the loss of sensitivity. The dielectric layer is made of Polydimethylsiloxane (PDMS). Although PDMS is a nonlinear hyper-elastic material, the strain region within 50% can be approximately linear (Kim *et al.*, 2011). Therefore, PDMS is set as a linear elastic material in COMSOL simulation.

Figure 5.3 shows the cross-sectional view of the truncated pyramid micro-structure. The geometric parameters include length of the upper side a, length of the lower side b, height h and side inclination angle θ. These parameters satisfy the formula: $b = a + 2 * h * \cot(\theta)$. The truncated pyramids are uniformly distributed with separation distance s. With a fixed h, a unique structure can be obtained if any two parameters are known.

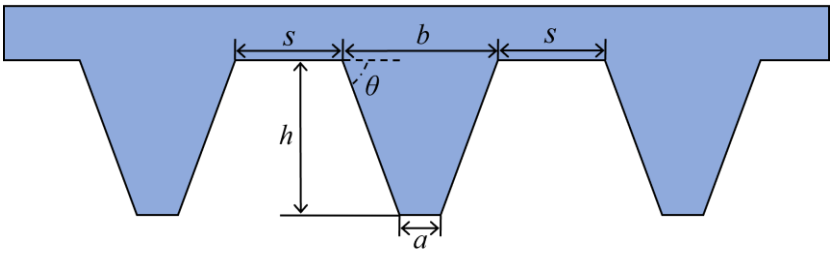

Figure 5.3: Structural parameters of the truncated pyramid.

Figure 5.4 (a) shows the dielectric layer displacement as a function of θ when a is fixed under pressure of 100 kPa. The greater the displacement of the dielectric layer, the higher the sensitivity of the sensor. The displacement of the dielectric layer increases with increasing θ, which is consistent with the results in the literature (Tee *et al.*, 2014). However, this model does not consider the effect of separation distance. The separation distance of the micro-structures also increases with θ, which is another important factor for the increased sensitivity. If the separation distance is set to be constant, the larger the θ, the greater the number of micro-structures per unit area. In this case, the displacement of the dielectric layer decreases with increasing θ, as shown in Figure 5.4 (b).

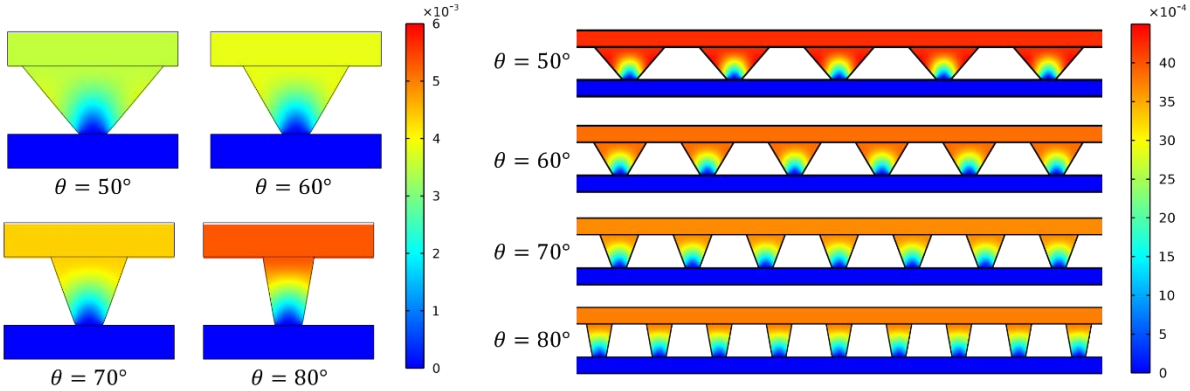

(a) (b)

Figure 5.4: The effect of separation distance on the displacement of the dielectric layer. (a) Displacement of a single microstructure as a function of θ (various separation distances), (b) Displacement of the dielectric layer per unit area as a function of θ (fixed separation distance).

The aspect ratio (defined as $\alpha = a/h$) and θ are used as variables to analyse the influence on the sensitivity. The value of aspect ratio is in the range of 0.2 to 1.2, and the range of θ is 50° to 80°. Other geometric parameters are listed in Table 5.1.

Table 5.1: Geometry parameter settings for finite element simulation.

Parameters	Value	Description
t	0.1 mm	Thickness of dielectric layer/electrode layer
s	0.2 mm	Separation distance
h	0.2 mm	Height of truncated pyramid
α	0.2~1.2	Aspect ratio
θ	50° ~ 80°	Side inclination angle

The normalised displacement of the dielectric layer under 100 kPa is shown in Figure 5.5. Under the same aspect ratio, the displacement does not change monotonically with θ. As the aspect ratio increases, the effect of θ on the sensitivity decreases. The upper red line represent the mean value of the displacement under the same aspect ratio, which intuitively reflects that the sensitivity of the sensor is negatively related to the aspect ratio.

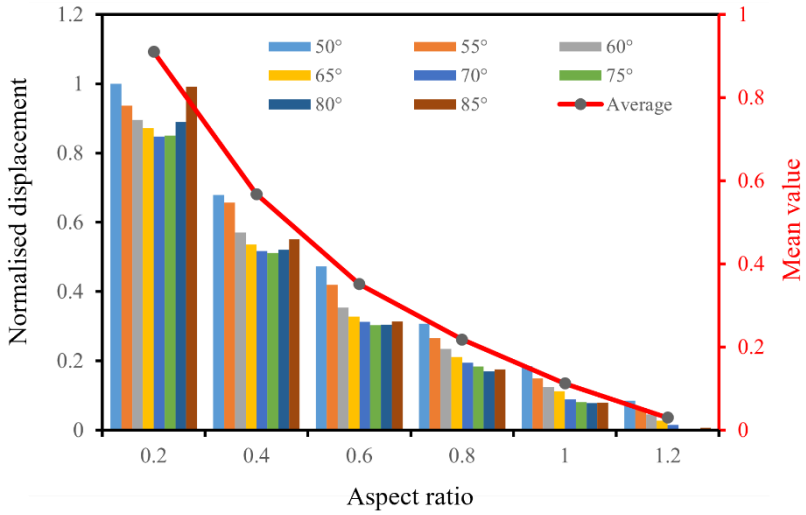

Figure 5.5: Normalised displacement and average value as a function of aspect ratio.

The maximum pressure that the micro-structure can withstand is regarded as the measurement range of the sensor, and the finite element calculation no longer converges beyond this pressure value. Figure 5.6 shows the normalised measurement range. As expected, the measurement range increases as the aspect ratio increases.

From the above results, the aspect ratio of the truncated pyramid has a greater impact on the sensitivity and measurement range than the side inclination angle. Also, the negative correlation between the sensitivity and the measurement range is verified. To balance the sensitivity and measurement range of the sensor, the multiplication of the two is used as an evaluation index, as shown in Figure 5.7. The sensitivity and measurement range of the sensor are relatively balanced when the aspect ratio around 0.6.

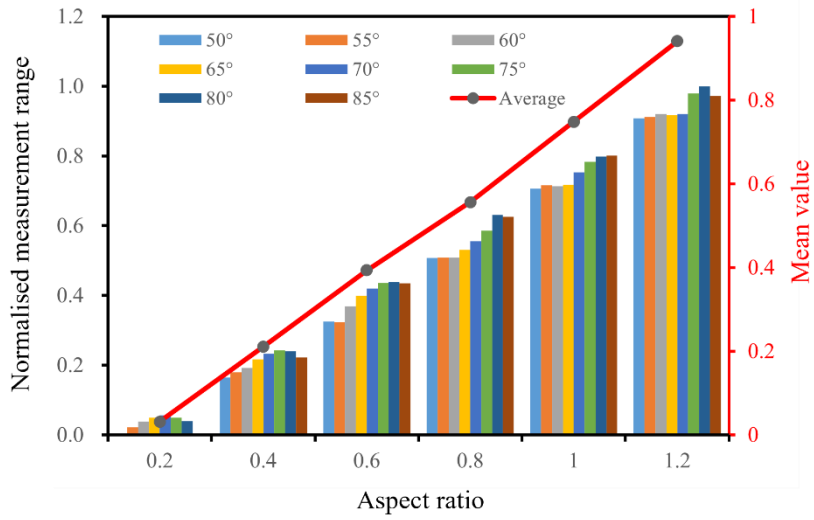

Figure 5.6: Normalised measurement range and average value as a function of aspect ratio.

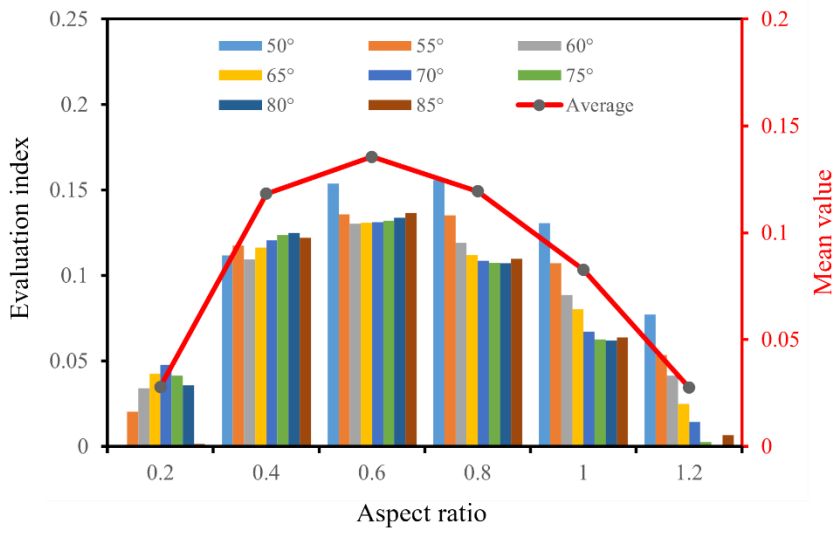

Figure 5.7: Evaluate index as a function of aspect ratio.

5.1.3 Optimised design of contact layer

For distributed tactile sensors with a large number of sensing units, configuring the contact structure for each unit is undoubtedly time-consuming and labour-intensive. In the following, three novel contact structures will be introduced to replace the traditional truncated pyramid structure.

As shown in Figure 5.8, the contact layer structure has a height of 500 μm and is uniformly distributed on the PDMS substrate with a thickness of 200 μm. Figure 5.8 (a) and (b) are

arrays of cylinders and hemispheres with a base diameter of 1 mm, respectively. Figure 5.8 (c) is an array of Y-shaped structures, the angle between any two sides is 120°, and the length and width of each side are 1.5 mm and 0.5 mm, respectively.

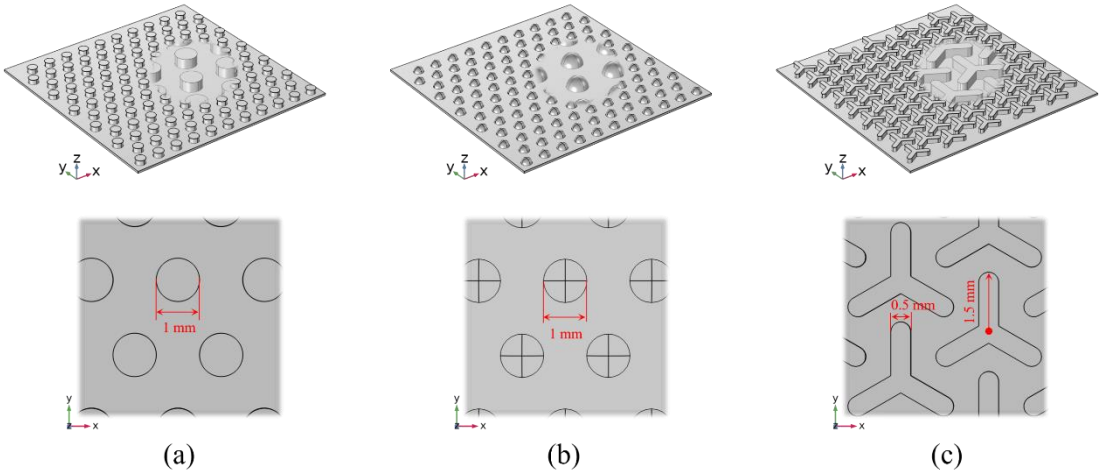

Figure 5.8: Schematic diagram of the contact layer structure. (a) Cylindrical structure, (b) Hemispherical structure, (c) Y-shaped structure.

The deformation of the dielectric layers caused by the same pressure distribution on different contact layer structures is differentiated. Here, three geometric models are used to simulate the situation of different pressure distributions, as shown in Figure 5.9. Model 1 is a circular pressure model that moves from centre to corner. Model 2 is a hollow square pressure model with three different side lengths. Model 3 is a triangle pressure model rotated around z-axis at 30° intervals. The dielectric layer displacements are compared by applying a normal pressure of 10 kPa to the top surfaces of the three models.

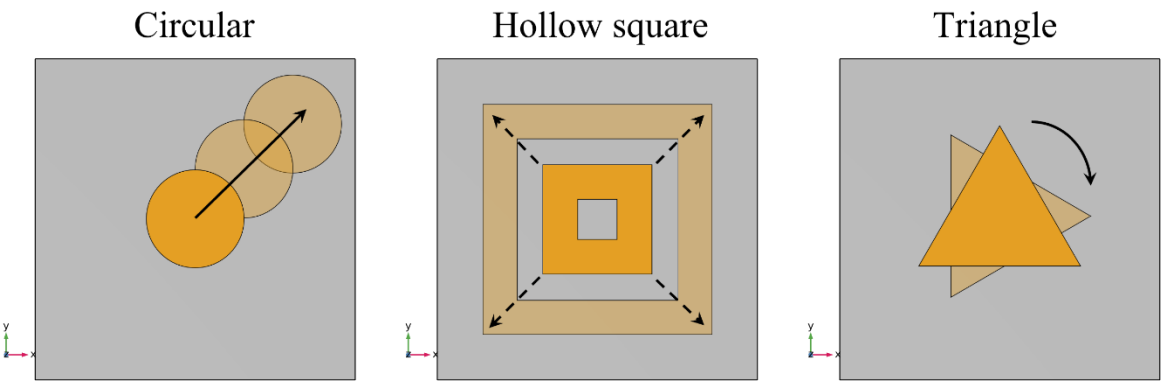

Figure 5.9: Geometric pressure distribution model.

The displacements of the dielectric layers under circular pressure distribution are compared in Figure 5.10. C1-C7 denote the circular pressure distribution at seven positions, and the red circle in the figure represents the actual contact profiles. Obviously, the displacement of the dielectric layer differs from that of the actual contact surface. The displacement distribution exhibits randomness as the contact position changes for contact layers with truncated pyramid, cylindrical, and hemispherical structures. In contrast, no significant difference is observed in the dielectric layer displacement of the Y-shaped structure, though there is still some blurring at the edges.

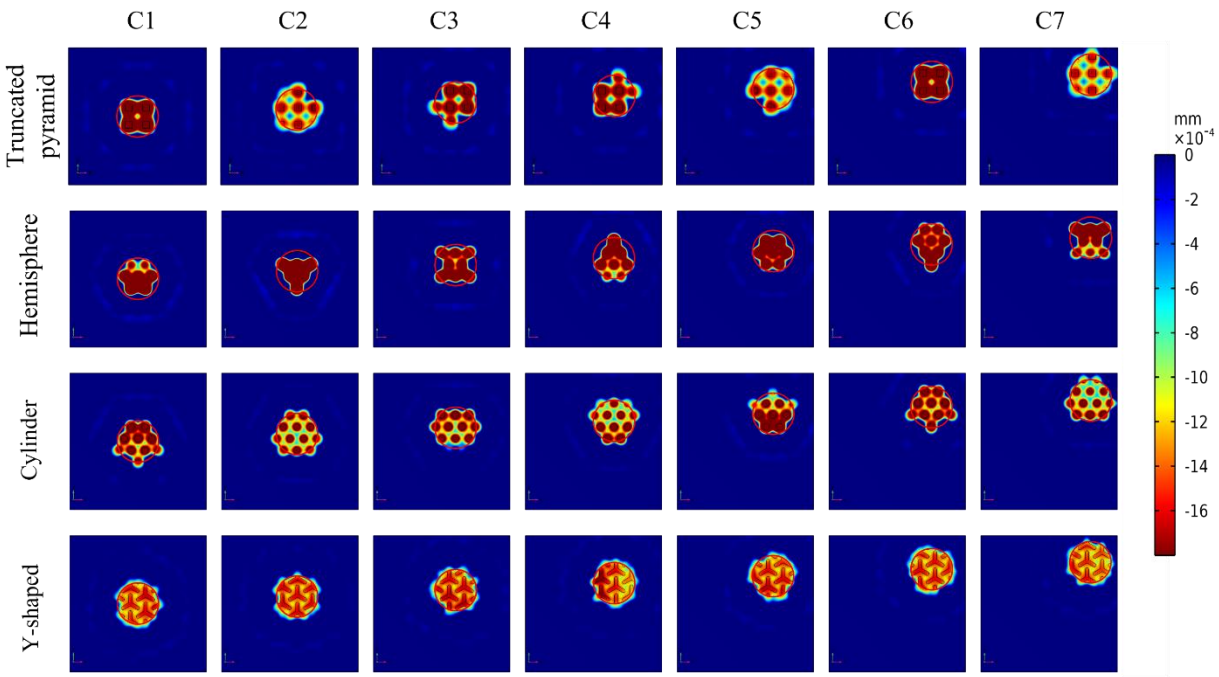

Figure 5.10: Displacement comparison of dielectric layers under circular pressure distribution.

Three evaluation indices are defined to quantitatively compare the four contact layer structures. Note that the actual contact area is taken as the region of interest (ROI).

(1) Average displacement (AD) is the average displacement of dielectric layer within ROI. Under the same pressure, the larger the AD, the higher the sensitivity of the sensor.

(2) Uniformity (P) reflects the uniformity of the displacement distribution within ROI. The smaller the value of P, the higher the uniformity.

(3) Area error (AE) is a measurement of the difference between the displacement distribution of the dielectric layer and the actual contact area. The smaller the error, the more accurate the estimate of the shape of the contact object.

Tables 5.2-5.4 show the normalised average displacement, uniformity, and area error, respectively. In terms of average displacement, the hemi-spherical contact layer has the largest value due to the smallest contact area with the pressure model, while the Y-shaped contact layer has the smallest value. However, The Y-shaped contact layer has better uniformity and smaller area error than the other three structures. Moreover, the Y-shaped structure has the smallest standard deviation of these three evaluation indexes, indicating that it is more consistent in different pressure distributions than the other three structures.

Table 5.2: Comparison of the average displacement under circular pressure distribution.

Structure	**C1**	**C2**	**C3**	**C4**	**C5**	**C6**	**C7**	**Average**	**Standard deviation**
Truncated pyramid	0.68	0.10	0.31	0.30	0.09	0.66	0.00	0.30	0.27
Hemisphere	0.88	1	0.67	0.69	0.86	0.66	0.70	0.78	0.13
Cylinder	0.49	0.24	0.31	0.27	0.56	0.43	0.16	0.35	0.15
Y-shape	0.17	0.17	0.18	0.17	0.16	0.14	0.11	0.16	0.02

Table 5.3: Comparison of the uniformity under circular pressure distribution.

Structure	**C1**	**C2**	**C3**	**C4**	**C5**	**C6**	**C7**	**Average**	**Standard deviation**
Truncated pyramid	0.58	0.31	0.46	0.46	0.31	0.59	0.33	0.43	0.121
Hemisphere	0.80	0.83	0.66	0.73	0.65	0.61	0.79	0.72	0.084
Cylinder	0.47	0.30	0.40	0.35	0.56	0.46	0.35	0.41	0.090
Y-shape	0.17	0.17	0.20	0.19	0.20	0.17	0.16	0.18	0.015

Table 5.4: Comparison of the area error under circular pressure distribution.

Structure	C1	C2	C3	C4	C5	C6	C7	Average	Standard deviation
Truncated pyramid	58%	52%	55%	56%	52%	59%	51%	55%	0.033
Hemisphere	80%	84%	74%	79%	65%	69%	83%	76%	0.072
Cylinder	55%	51%	54%	52%	59%	57%	53%	54%	0.026
Y-shape	34%	35%	34%	35%	37%	36%	31%	35%	0.019

The simulation results for hollow square pressure distribution are shown in Figure 5.11. The truncated pyramid structure performs best under the large-scale hollow square pressure distribution. However, as the square shrinks, the central hollow area cannot be accurately identified. In contrast, the hollow area can be distinguished by hemi-spherical and cylindrical structures, but there is a distortion in comparison to the actual distribution. Even though the Y-shaped structure has a smaller displacement than the other three, the overall uniformity of the pressure distribution is excellent.

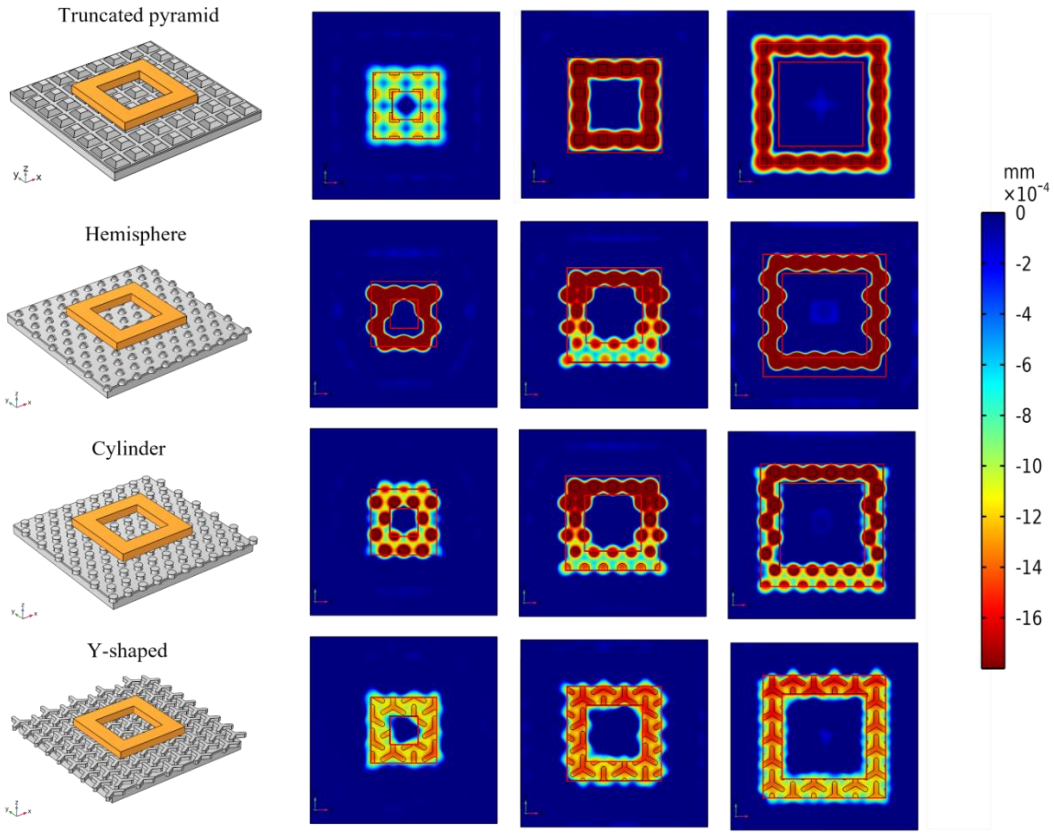

Figure 5.11: Displacement comparison of dielectric layers under hollow square pressure distribution.

The disadvantage of the truncated pyramid structure is more noticeable in the case of the triangular pressure distribution. As shown in Figure 5.12, the displacement distribution of the dielectric layer is severely distorted, and the rotation angle cannot be determined. In addition, the hemi-spherical structure has an approximately triangular pressure distribution only at a specified rotation angle. In contrast, the displacement distribution caused by the cylindrical and Y-shaped structures is closest to the triangle and can accurately distinguish the variation of the rotation angle.

According to the above simulation results, regardless of whether the shape of the pressure distribution is regular or not, the contact layer of the Y-shaped structure provides a uniform displacement distribution and has little effect on the area without pressure. This means that contact layers with a Y-shaped structure do not require a precise alignment process, which can simplify the fabrication of distributed tactile sensors.

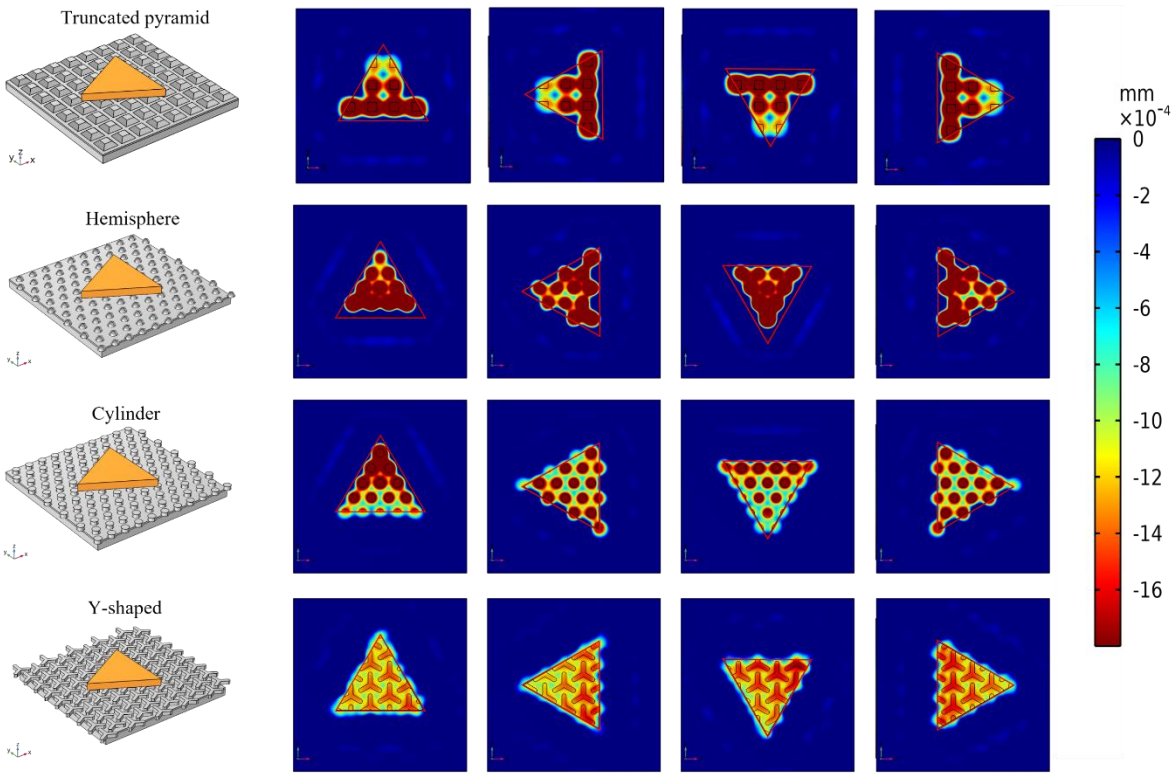

Figure 5.12: Displacement comparison of dielectric layers under triangular pressure distribution.

5.2 Sensor fabrication

5.2.1 Electrode layer

The electrode of the sensor is made of double-sided flexible printed circuit board (FPCB). The row and column electrodes are drawn from the top and bottom layers and are connected through 0.3 mm metallised vias. As shown in Figure 5.13 (a), red and blue represent the traces (0.1 mm) on the top and bottom layers, respectively. All traces are gathered in the corner of the sensor array, which connects to a gold finger with 17 pins (16 electrode terminals and 1 ground terminal).

The design of distributed sensors needs to consider the problem of crosstalk between adjacent electrodes. As the number of sensing units increases, parallel traces introduce a large amount of parasitic capacitance. Therefore, the back grounding shield is extended to cover all parallel traces. Figure 5.13 (b) shows an exploded view of the electrode structure.

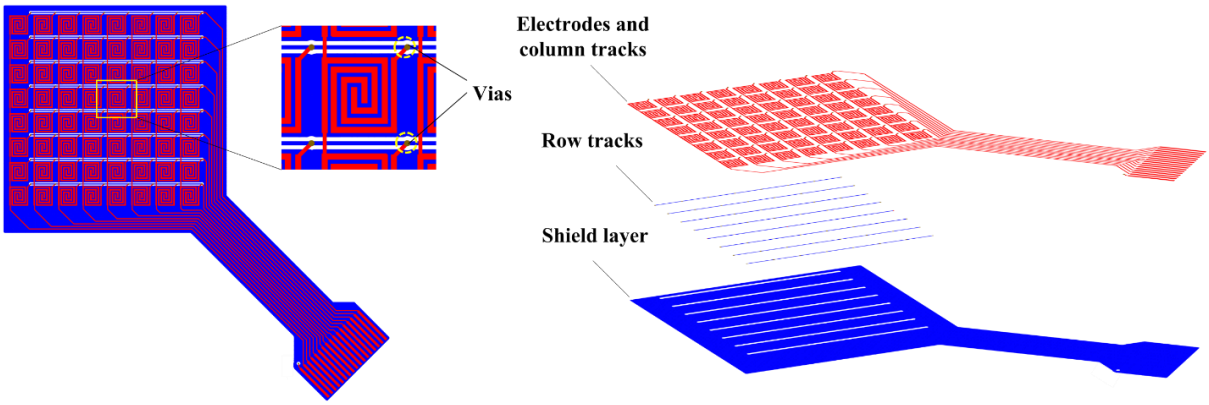

(a) (b)

Figure 5.13: Schematic diagram of the electrode structure. (a) PCB layout of electrodes and traces, (b) Exploded view of PCB layers.

Figure 5.14 shows the fabricated electrode array. The overall electrode array dimensions are 20 mm x 20 mm. The square spiral electrode has a side length of 2 mm. The centre-to-centre distance between adjacent electrodes is 2.5 mm, implying that the spatial resolution is 2.5 mm, which is greater than the spatial resolution of the human palm (about 5 mm) (Dahiya *et al.*, 2009).

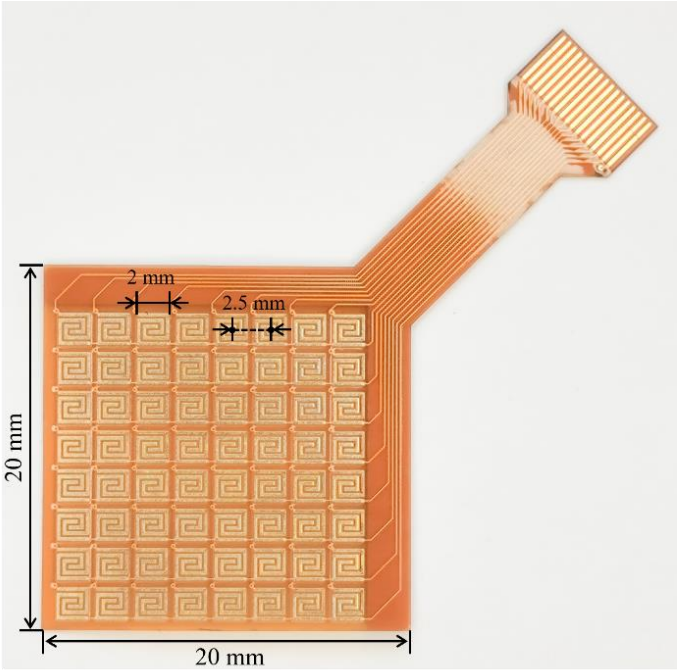

Figure 5.14: Photograph of actual electrode.

5.2.2 Dielectric layer and contact layer

Figure 5.15 shows the 3D printed mould based on the simulation of the structural parameters of the dielectric layer. The 3D printed mould is made of photosensitive resin with an accuracy of 5 μm. Although 3D printed moulds are inevitably rougher than silicon moulds, the surface roughness is acceptable because it has no effect on the mechanical properties of the dielectric layer. Before use, the mould is ultrasonically cleaned in absolute ethanol, and then PDMS mould release agent (HAMLD) is sprayed evenly on the mould surface. After the solvent has completely evaporated, a thin film is formed on

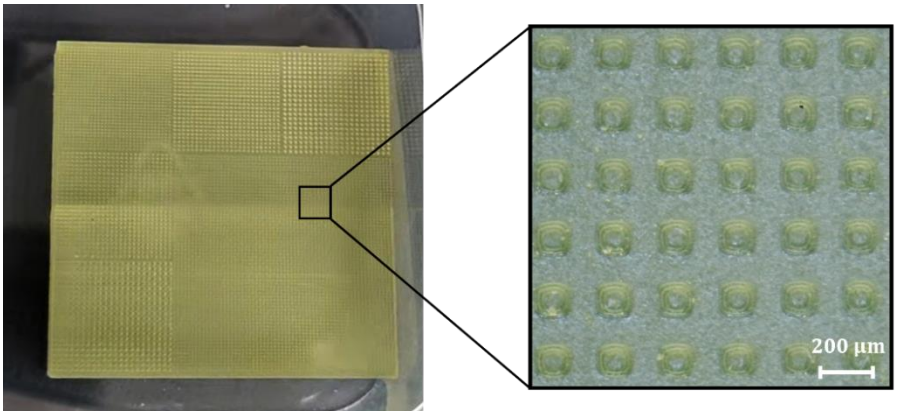

Figure 5.15: 3D printed mould of dielectric layer.

the mould surface to ensure that the PDMS can be easily peeled from the mould (Cairone *et al.*, 2016).

Because the dimensions of the Y-shaped structure are in millimetres, the contact layer is made with a CNC-fabricated aluminium mould, as shown in Figure 5.16. Furthermore, the surface energy of metal moulds is lower than that of resin moulds, making PDMS easier to release from them. Higher temperature resistance is another reason to choose metal moulds, as temperature is a key parameter in determining PDMS hardness. The higher the temperature, the harder the cured PDMS and the less external force loss on the contact layer.

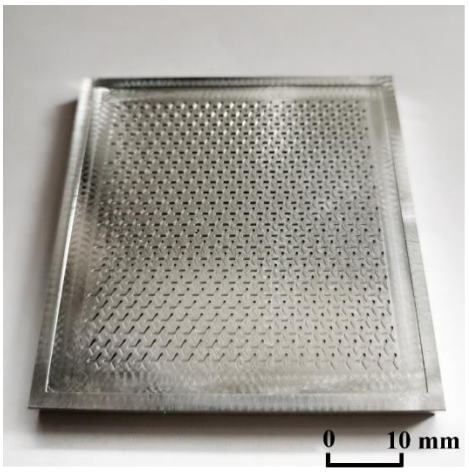

Figure 5.16: CNC aluminium mould of Y-shaped contact layer.

The mass ratios of resin and curing agent of PDMS (Sylgard 184, Dow Corning) used to cast the dielectric and contact layers are 10:1 and 5:1, respectively. After mixing and stirring, PDMS is degassed for 30 min and poured into a mould for spin coating with a thickness of 300 μm, followed by a second degassing. The mould is then placed in a 60 °C oven for 6 hours to peel off the cured PDMS. The contact layer is hardened for an additional 30 minutes at 100 °C. The electrode layer, dielectric layer and contact layer are assembled with uncured PDMS with a thickness of 50 μm as the adhesive layer. Figure 5.17 shows the final fabricated sensor.

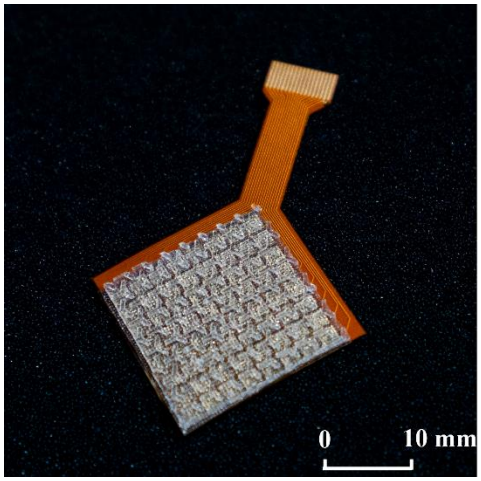

Figure 5.17: Photograph of the fabricated sensor.

5.3 Capacitance measurement system design

To validate the rationality and practicability of the design of the distributed tactile sensor, a multi-channel capacitance acquisition system is designed to record the capacitance changes of all tactile sensing units. As shown in Figure 5.18, the core components consist of a microcontroller (MCU), a capacitance-to-digital converter (CDC), and a multiplexing module (MUX). The upper computer receives the collected capacitance data via the serial port. A graphical user interface is developed using C#.net platform, which combined with MatLab for data analysis and pressure map visualisation.

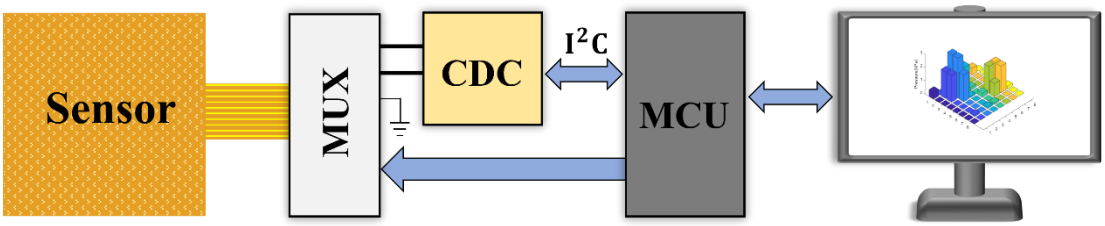

Figure 5.18: Schematic diagram of distributed tactile sensing measurement system.

5.3.1 Capacitance-to-digital converter

A 12-bit CDC AD7150 (Analog Devices, 2007) is used to measure capacitance. Compared with the traditional circuit using separate components, this solution has simple circuit and high measurement accuracy. AD7150 has a measurement range of 0–14 pF

and a sensitivity of up to 1 fF, which fully covers the capacitance value of the designed tactile sensing array. The capacitance conversion time is 10 ms, and the converted digital signal is sent to the MCU (STM32F103C8T6, STMicroelectronics) through I^2C communication.

5.3.2 Crosstalk analysis

With an orthogonal electrode arrangement, only 16 wires are needed for an 8×8 sensing array, which eases the design of the sensor and measurement system. The measurement results, however, may contain errors due to coupling and crosstalk between adjacent units. Taking sensing unit C_{11} (Row 1, Column 1) as an example, the equivalent circuits for 2×2 and 3×3 arrays are shown in Figures 5.19 (a) and (b), respectively. The measured capacitance C_X is the parasitic capacitance C_P connected in parallel with C_{11}. Ideally, the initial capacitance of each sensing unit is the same, denoted as C_0. By calculation, the actual measured capacitances of the 2×2 array and the 3×3 array are $4C_0/3$ and $9C_0/5$, respectively. This means that the measured sensing unit will change with the surrounding sensing units, which is the so-called crosstalk.

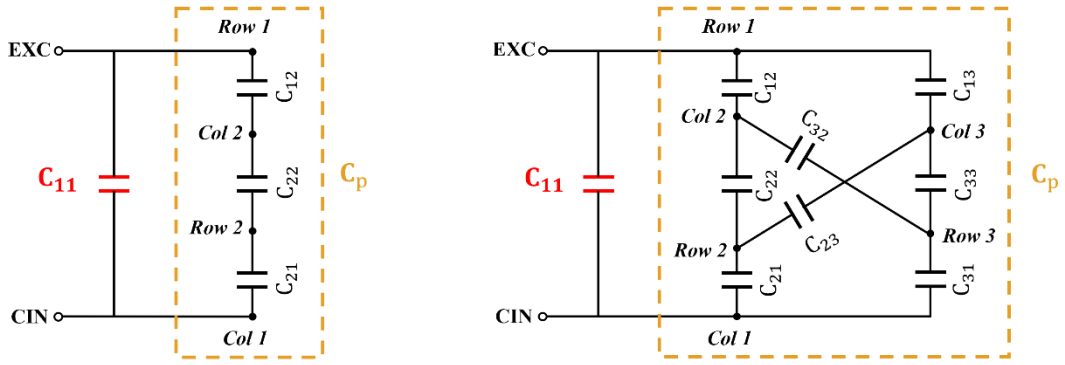

$C_X = C_{11} || C_p = C_0 + C_0/3 = 4C_0/3$

(a)

$C_X = C_{11} || C_p = C_0 + 4C_0/5 = 9C_0/5$

(b)

Figure 5.19: Crosstalk analysis for (a) 2×2 sensing array and (b) 3×3 sensing array.

5.3.3 Multiplexing module

A way to protect against parasitic capacitance is to ground electrodes that are not being measured. The configuration of three single-pole single-throw (SPST) switches for each electrode, as shown in Figure 5.20 (a), is the simplest way to achieve the three-state switching of EXC, CIN, and GND. However, the parasitic capacitance inside the switch is ignored. For instance, the measurement may still be impacted by the parasitic capacitance of switch S2 when switch S1 is closed and switch S2 and switch S3 are open. Therefore, the T-switch shown in Figure 5.20 (b) is used. When switches S3 and S6 are closed, the parasitic capacitances in switches S1 and S2 (or S4 and S5) are released and current can flow down the path, reducing the impact on the measurement. (Rodriguez-Frias and Yang, 2020).

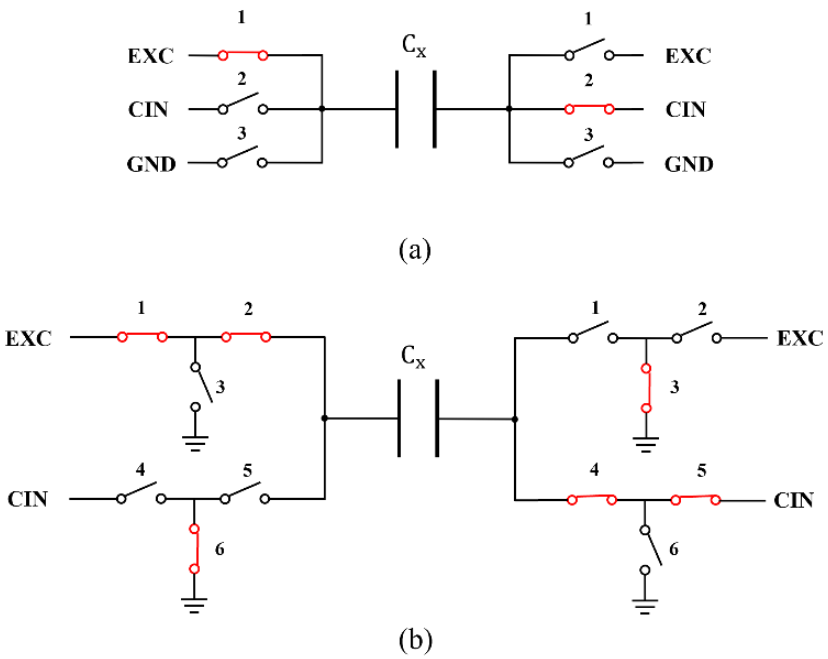

Figure 5.20: Two types of multiplexer modules. (a) Configuration of three SPST analogue switches, (b) Configuration of T-switch.

Three single-pole double-throw (SPDT) analogue switches are used to implement the T-switch, as shown in Figure 5.21. The analogue switch used is SN74LVC1G3157 (Texas Instruments, 2003), which provides adequate switching speed (typically 0.5 ns). The switching logic for the T-switch is shown in Table 5.5. Since the logic of switches S1 and S2 is always the same, the switch logic can be simplified by two bits. The electrodes are

connected to EXC, CIN, and GND when the control terminals of switches S1 (S2) and S3 are 01, 10, and 00, respectively.

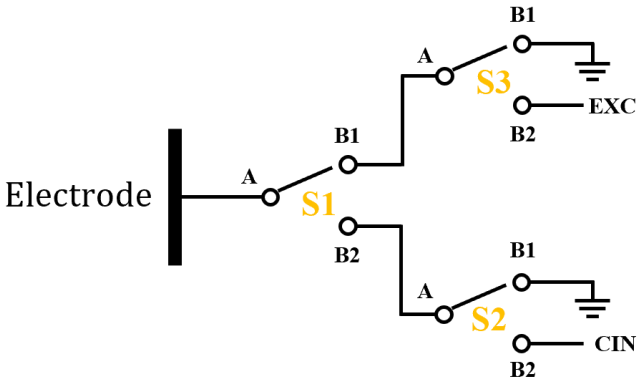

Figure 5.21: Implementation of a T-switch with three SPDT analogue switches.

Table 5.5: The switching logic of the T-switch.

S1	S2	S3	State
0	0	1	EXC
1	1	0	CIN
0	0	0	GND

The maximum number of capacitance measurement channels is limited by the number of I/O ports of the MCU. In this work, channel expansion is implemented using a shift register (SN74HC595, Texas Instruments), which is an 8-bit serial input parallel output shift register. Figure 5.22 shows the schematic of a cascaded circuit of 10 pieces of SN74HC595. A 40-channel measurement system can be implemented by controlling 80-bit signals synchronously with only three ports (SER, SRCLK, and SCLK).

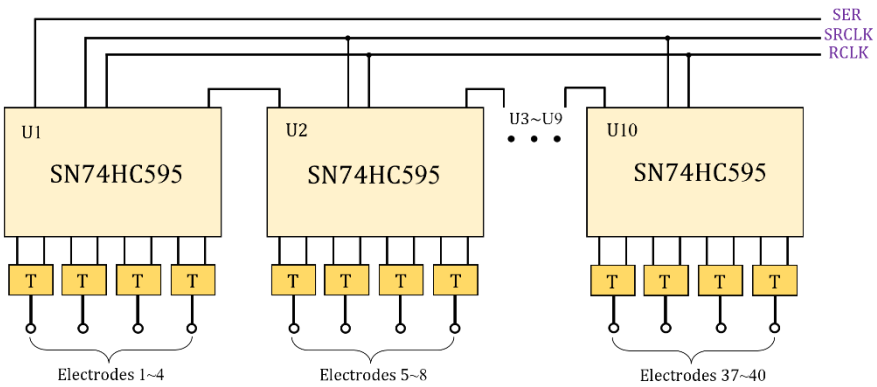

Figure 5.22: Schematic of the cascade circuit of 10 pieces of SN74HC595.

Capacitance measurement systems with different number of channels are designed according to application requirements. Figure 5.23 (a) shows a 9-channel capacitance measurement system that utilises 18 I/O ports directly. This system is designed for single tactile sensor and 3D tactile sensor applications. In this chapter, a measurement system that expands the number of channels to 40 is designed for the distributed capacitive sensor, as shown in Figure 5.23 (b). In addition, by isolating the multiplexing unit, the two measurement ports of the AD7150 are drawn out with SMB connectors for connection with coaxial shielded cables.

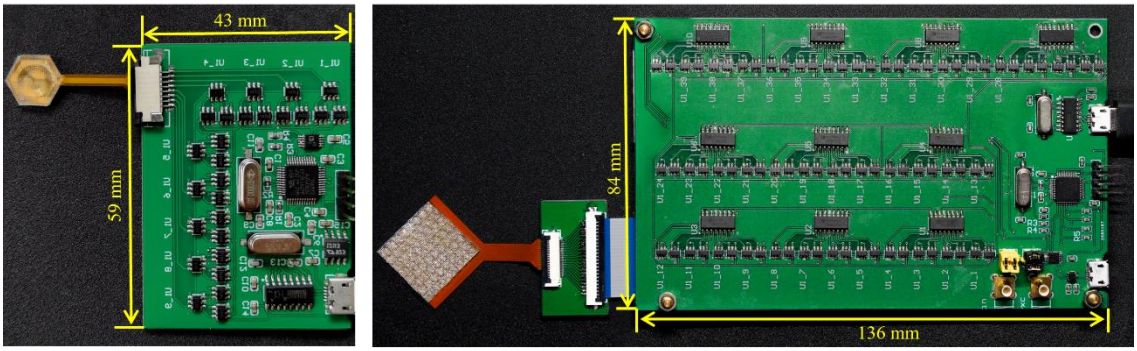

(a) (b)

Figure 5.23: Photographs of (a) 9-channel capacitance measurement system and (b) 40-channel capacitance measurement system.

5.4 Experimental results

5.4.1 Evaluation of capacitance measurement system

The capacitance measured by the impedance analyser (MFLI 500 kHz Lock-in Amplifier, Zurich Instruments) is used as a reference to assess the accuracy of the capacitance acquisition system. As shown in Figure 5.24 (a), AD7150 and impedance analyser are connected to the MUX via jumpers and SMB connectors to measure the initial capacitance of all sensing units. The impedance analyser performs measurement with an excitation signal frequency of 32 kHz and a voltage amplitude of 1 V. As shown in Figure 5.24 (b), the capacitance measured by AD7150 almost coincides with the capacitance

measured by impedance analyser. The slightly larger capacitance measured by AD7150 comes from the parasitic capacitance that exists between the chip pins and jumpers. However, the maximum deviation value is 236.7 fF, demonstrating the high accuracy of the capacitance measurement system. Because the electrode traces of Row 8 and Column 1 are adjacent (as shown in the inset), the capacitance of the sensing unit at the intersection (R8-C1) is significantly higher than the capacitance of the other sensing units.

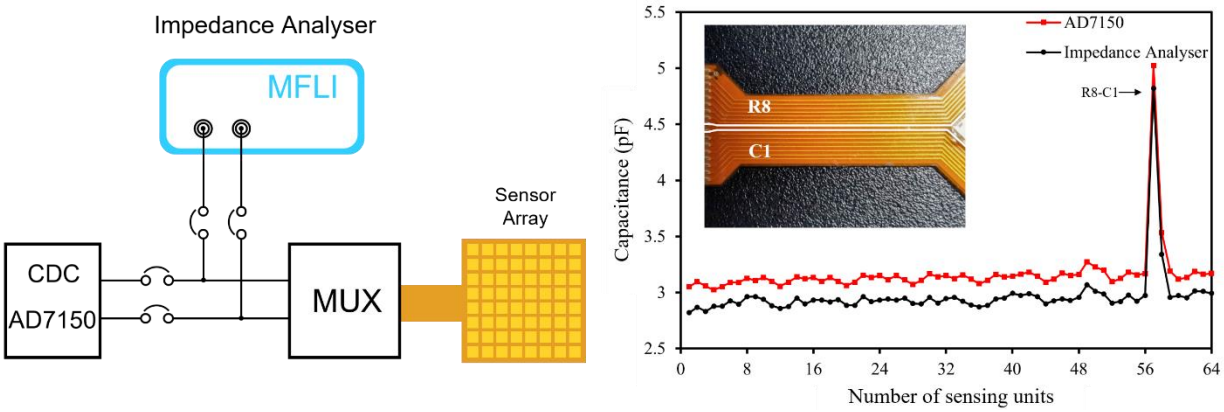

(a) (b)

Figure 5.24: Capacitance measurement system accuracy test. (a) Hardware setup, (b) Comparison of initial capacitance.

5.4.2 Tactile sensing

The crosstalk of the sensing array is evaluated. A rod with a diameter of 3 mm is used to sequentially apply a pressure of 2 kPa to the sensing unit R5-C5 and its four surrounding sensing units. The normalised capacitance changes for five adjacent sensing units are depicted in Figure 5.25 (a). When a force is applied to a single sensing unit, the capacitance of the surrounding sensing units rises as well. This is caused by the mechanical properties of the flexible contact layer on the one hand, and the interference between the capacitive signals of the sensing array on the other. Despite this, the capacitance change caused by crosstalk is much smaller than the capacitance change caused by external force. Furthermore, the effect of crosstalk diminishes as one moves away from the centre of the external force.

To investigate the effect of external force amplitude on crosstalk, sensing unit R5-C5 is subjected to pressures of 2 kPa, 1.5 kPa, and 1 kPa. Figure 5.25 (b) depicts a 2D map of the capacitance change, with the dotted circle representing the position where the external force is applied. As expected, in addition to sensing unit R5-C5, the remaining sensing units also exhibit capacitance changes, which appear as ghosting in the 2D map. When the pressure is reduced from 2 kPa to 1 kPa, the ghosting caused by crosstalk is reduced as well. In any case, it is obvious that the sensing unit R5-C5 always experience the greatest capacitance change.

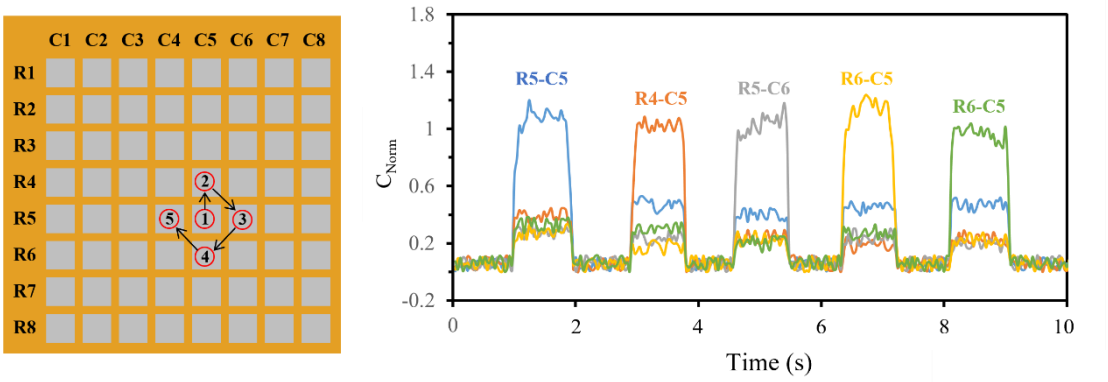

(a)

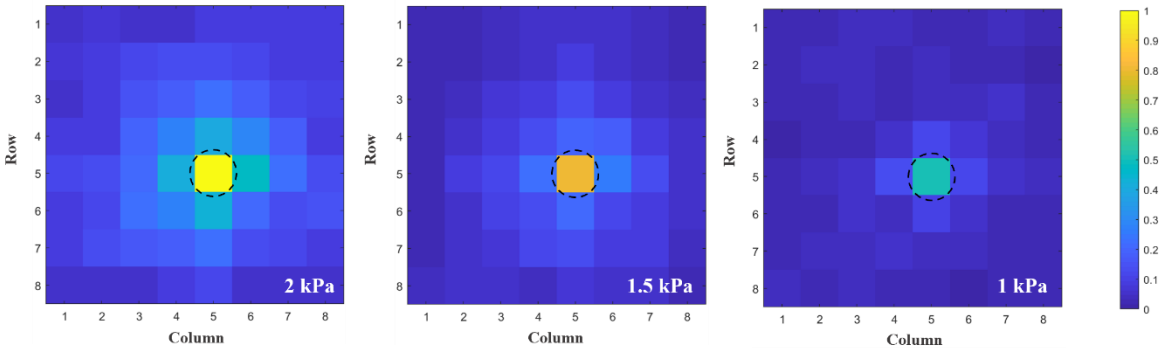

(b)

Figure 5.25: Crosstalk analysis of five adjacent electrodes. (a) Capacitance response when external force is applied at different positions, (b) 2D map of the capacitance change of the sensing array under different external force amplitudes.

To demonstrate the detection performance for spatially distributed pressure, five 3D printed letters 'U', 'O', 'M', 'A' and 'N' are placed on the sensor surface with a uniform force, as shown in Figure 5.26 (a). The acquired capacitance change is processed by

MatLab to obtain the pressure map, as shown in Figure 5.26 (b). Figure 5.26 (c) shows the result of quadrupling the interpolation. The pressure distribution is not uniform, which can be attributed to the inconsistent sensitivity of each sensing unit and measurement noise. However, the shapes of these letters are still discernible. Due to mechanical stress and signal crosstalk, there is also a slight change in capacitance near the contact area. Regardless, the accuracy of shape recognition can be improved further by increasing the resolution of the electrode array.

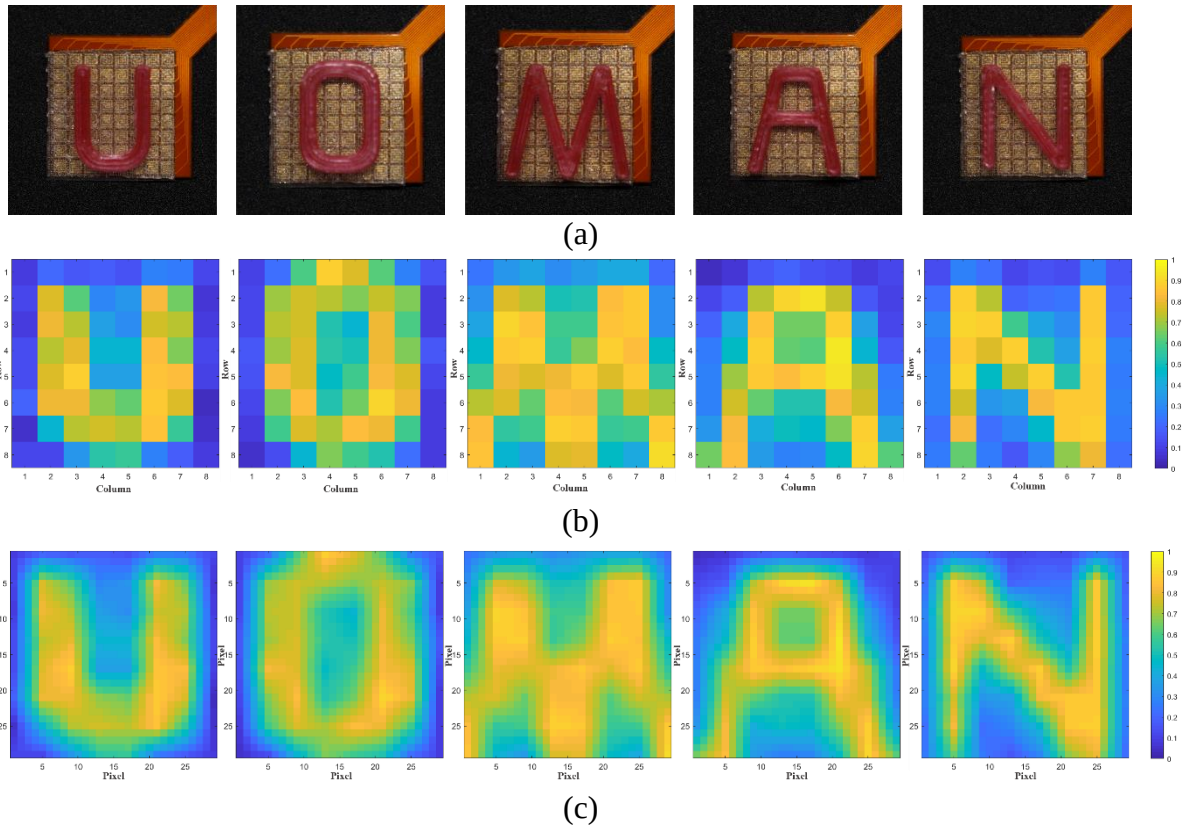

Figure 5.26: Detection performance of sensor array for letter-shaped pressure distribution. (a) The actual position of the letter, (b) The original pressure distribution map, (c) The quadruple interpolated pressure distribution map.

5.4.3 Proximity sensing

In addition to tactile sensing, planar capacitive sensors can also be used for proximity sensing, which is difficult to achieve with other types of tactile sensors. As shown in Figure 5.27, the fringing electric field between the two electrodes is disturbed by the

approaching finger, and part of the electric field is shunted to ground. The proximity of the finger results in the increase in Cf between the finger and the electrode, and thus a decrease in the measured mutual capacitance Cm. This is the general principle of capacitive proximity sensing, which is known as the shunt mode in the literature (Smith *et al.*, 1998).

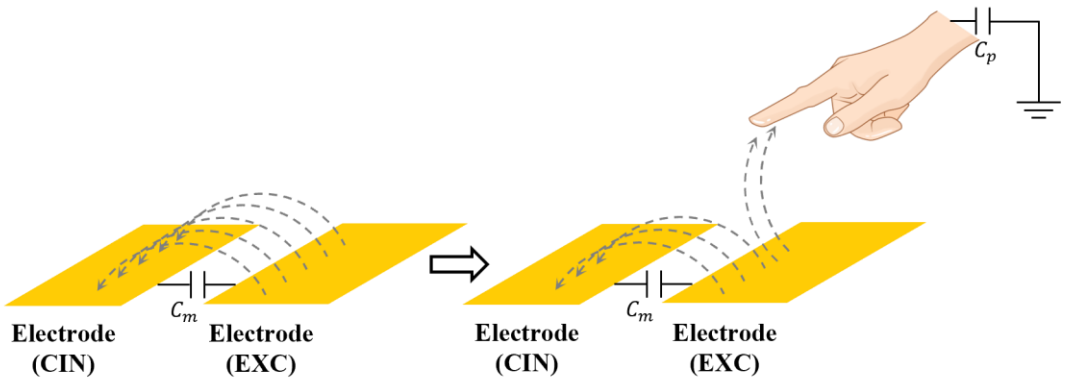

Figure 5.27: The principle of proximity sensing.

The detection distance is one of the most important metrics for evaluating the performance of proximity sensors, which is proportional to the electrode spacing (Xia *et al.*, 2018). For applications such as anti-collision and human-computer interaction, electrodes with large spacing are required to improve the detection distance. However, high spatial resolution is required for robotic grasping, which requires closely spaced electrodes. In this work, the electrode array is reconfigured to achieve the dual functions of far-proximity sensing and near-proximity sensing.

Figure 5.28 (a) illustrates the electrode configuration for far-proximity sensing. The symmetrical structure ensures sensitivity uniformity. To simulate a human finger, a grounded metal probe (15 mm × 15 mm) is used. Figure 5.28 (b) shows the change in capacitance as the metal probe approaches the centre of the sensor. According to the

definition in the literature (Li *et al.*, 2004), the effective detection distance is increased to 23 mm under this electrode configuration.

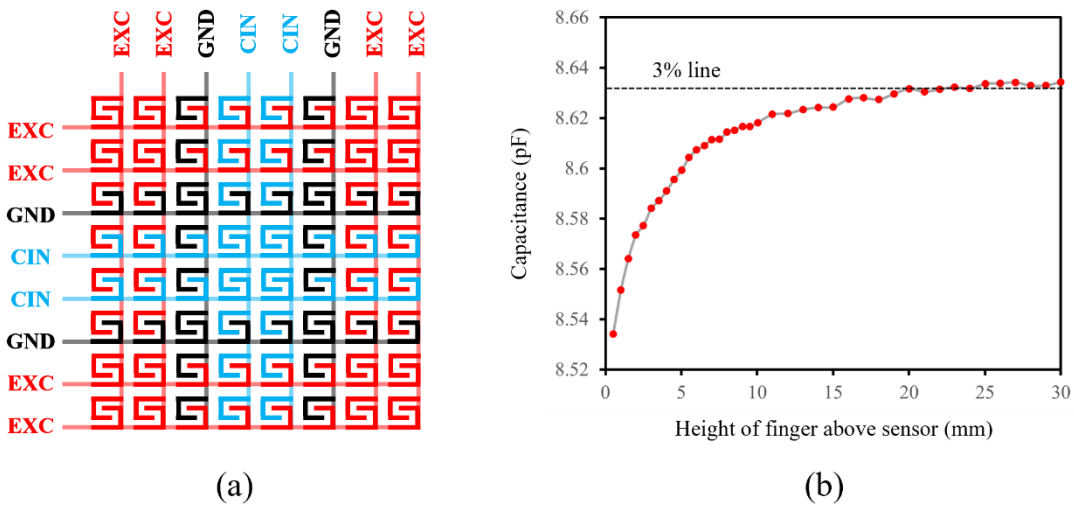

Figure 5.28: Evaluation of far-proximity sensing. (a) Electrode configuration, (b) Effective detection distance of the sensor.

To determine whether the sensor can reliably distinguish between finger approach and physical pressing, capacitance measurements are taken as the finger approaches the sensor, applying and releasing pressure until it moves away from the sensor. Figure 5.29 displays two cycles with two different pressure amplitudes. The turning points A and B in the figure represent where the finger touches and moves away from the sensor surface. Although the changes in capacitance caused by finger approach and physical pressing are opposite, the decrease in capacitance caused by finger approach is much smaller than the increase in capacitance caused by pressing. Therefore, the approach and touch of the finger can be accurately recognised by the turning points. In addition, the capacitive response near the turning points has high sensitivity, which can effectively avoid misjudgement.

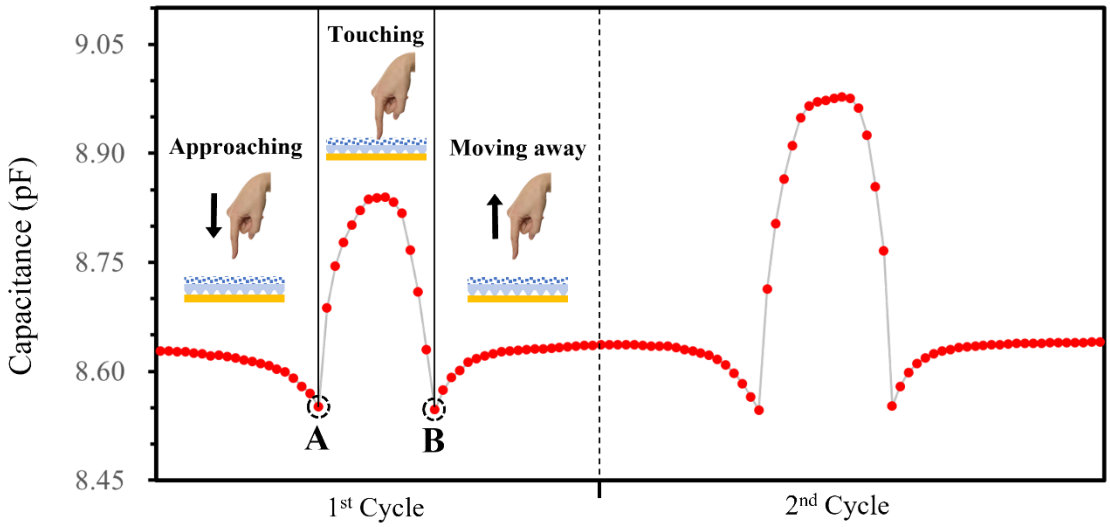

Figure 5.29: Capacitive response of finger approaching, applying pressure, and removing.

Determining the relative position of objects in hand is critical for robotic hands to ensure stable grasping. To acquire the target position without touching it, the sensor must have enough spatial resolution. Theoretically, the spatial resolution of the sensor depends on the spacing of adjacent electrodes. However, for the purpose of increasing the detection distance, adjacent electrodes are combined as new electrodes. Figure 5.30 shows the electrode configuration for near-proximity sensing at positions (1, 1) and (4, 4).

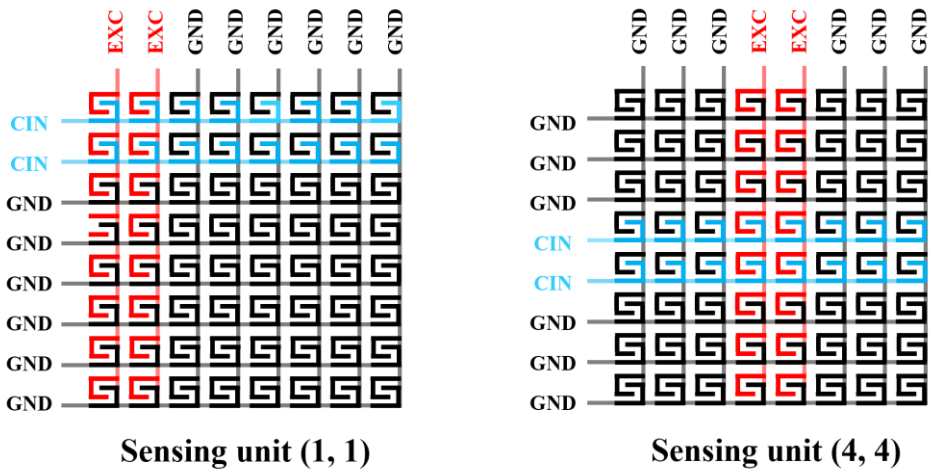

Figure 5.30: Electrode configuration for near-proximity sensing.

Figure 5.31 shows the capacitance change as a function of height when a single finger is hovered over the (4, 4) sensing unit to study the sensitivity in the z-axis direction. The

location of the finger is indicated by the dotted box in the centre. The capacitance change caused by the proximity of the finger is gradually revealed as the finger height is reduced from 10 mm to 2 mm. Furthermore, the shape of this area resembles that of a finger (ellipse), indicating that the sensor has excellent spatial resolution.

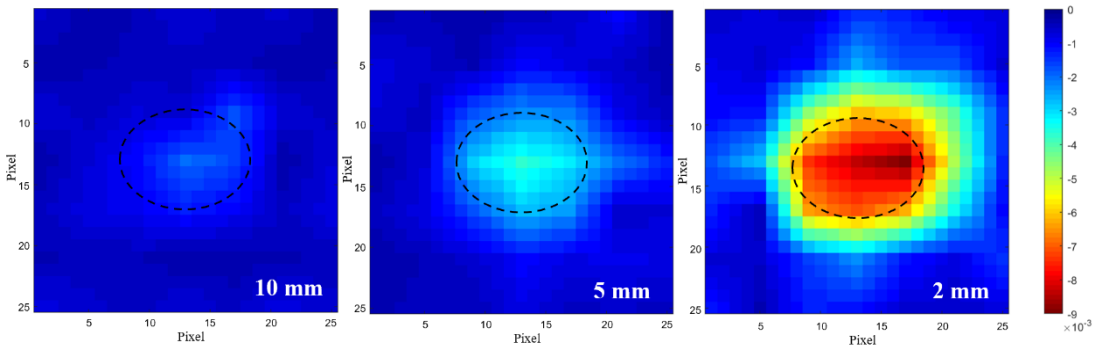

Figure 5.31: The capacitance variation with proximity of the finger.

To further illustrate the spatial resolution of near-proximity sensing, fingers in different orientations are hovered 2-4 mm above the sensor as shown in Figure 5.32. Obviously, the capacitance in the region where the finger is located is higher than in other regions. This experiment demonstrates the potential application of the sensor in contactless shape recognition and object localisation.

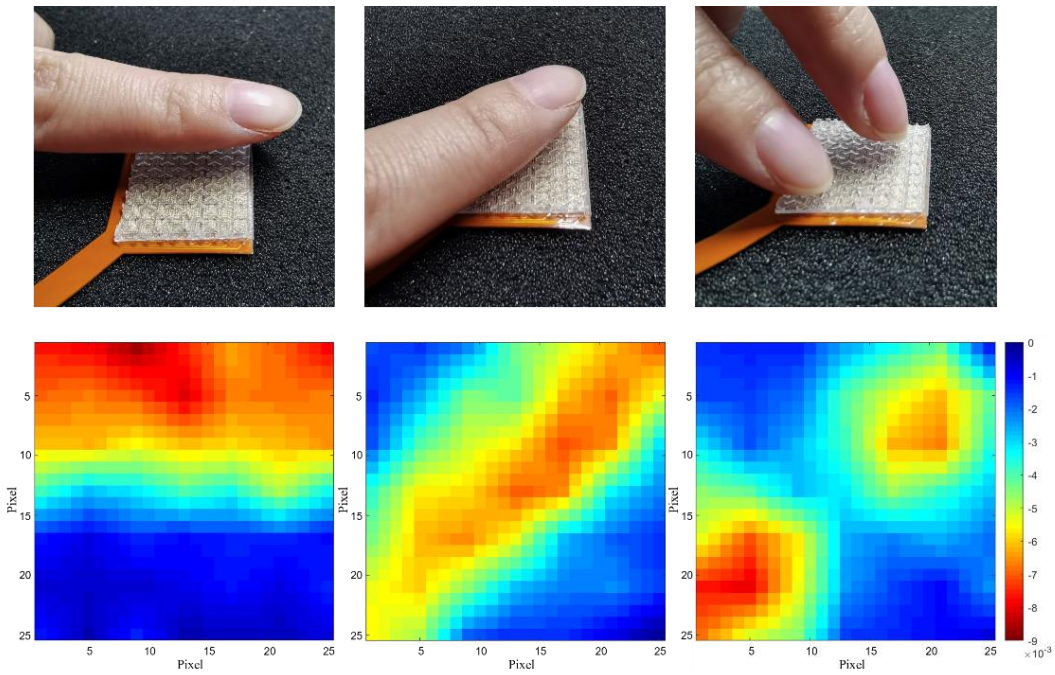

Figure 5.32: Evaluation of spatial resolution for near-proximity sensing.

5.5 Summary

In this chapter, a distributed tactile sensor array based on planar capacitance is designed, which can be summarised as follows:

(1) Finite element simulation is used to quantify the relationship between the geometric parameters of the micro-structure and the measurement range and sensitivity of the sensor. The results show that when the aspect ratio of the pyramid is around 0.6, the sensitivity and measurement range are relatively balanced. In practise, the fabrication process limits the minimum separation distance of the micro-structures. As a result, this model reflects the lower limit of sensitivity and the upper limit of measurement range. On this basis, according to practical applications, higher sensitivity and smaller measurement range can be obtained by increasing the separation distance.

(2) A contact layer with a Y-shaped structure is proposed, which solves the problem of difficult alignment of conventional contact layer. Besides, the combination of 3D printing and CNC is used to replace photolithography to make the mould, greatly simplifying the sensor manufacturing process and lowering production costs.

(3) As a supplement, proximity sensing expands the function of the tactile sensor. By configuring the electrode combination, the dual modes of far-proximity sensing and near-proximity sensing are realised on the same sensor. The tactile distribution and proximity sensing performance of the sensor are assessed using a self-designed capacitance measurement system. Through experiments, it has been confirmed that this sensor has promising applications in robotics, electronic skin, and human-computer interaction.

Chapter 6 Flexible tactile sensing based on ERT

As a potential tactile sensing solution, electrical resistance tomography (ERT) has certain advantages over conventional tactile sensor arrays. The purpose of this chapter is to increase the precision of ERT reconstructed images. To make the sensitivity distribution more uniform and increase the image accuracy in the central area, a new sensitivity matrix pre-processing method is proposed. In addition, the discrete wavelet transform-based image fusion is applied in combination with the features of various images to generate more accurate images. For the application of multi-objects, a new technique for extracting object position and size is proposed, and it can directly identify objects from distorted images. The above method has been verified by simulation and experiments with different distributions. The results demonstrated that the proposed method can effectively increase image accuracy, thus promoting the practical application of ERT in tactile sensing.

6.1 Sensor design

A square ERT sensor is used for both simulation and experimental verification with practical consideration. A 2D model of a square sensor created using COMSOL 5.6 is shown in Figure 6.1 (a). The sensor has a 200 mm side length. 16 electrodes of 9 mm in diameter are evenly distributed around it. The area highlighted in red is the region of interest (ROI), which is used to detect the pressure distribution.

To achieve reliable electrical connection, a flexible printed circuit board (FPCB) is used as the substrate and metal snap poppers as electrodes, as shown in Figure 6.1 (b). The male part of the snap popper is evenly installed at the boundary of the sensitive material

and the female part of the snap popper is fixed on the pad of the FPCB at the corresponding position.

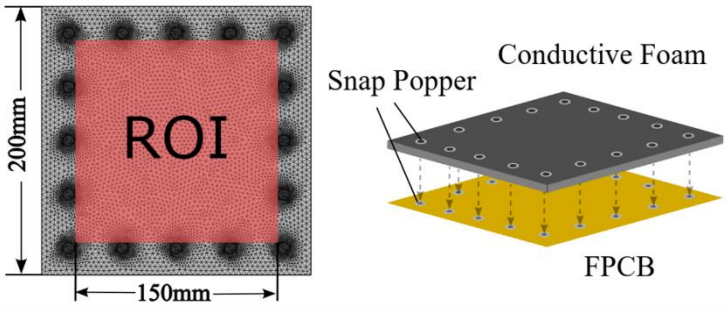

(a) (b)

Figure 6.1: Simulation model and structure diagram of the ERT tactile sensor.

Figure 6.2 (a) shows the fabricated flexible ERT sensor. Pressure-sensitive foam is used as the sensitive material. The resistance decreases when external pressure is applied. The electrodes are connected to the measurement circuit through a flexible cable connector. Benefiting from the flexible characteristics of FPCB, the ERT sensor can be bent in any direction while still maintaining a stable electrical connection, as shown in Figure 6.2 (b). This design also has the benefit of making it simple to disassemble sensitive materials for experimental verification and maintenance.

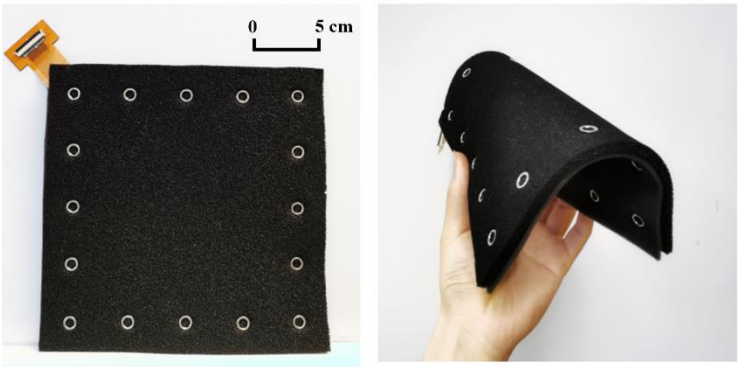

Figure 6.2: The flexible ERT tactile sensor used in this work.

6.2 Image distortion analysis

As mentioned, the reconstructed image of ERT has obvious distortion compared with the actual conductivity distribution. Image distortion can be caused by a variety of factors, including sensor design, measurement accuracy, signal interference, *etc*. To improve the image quality, the reconstruction process that causes distortion must be investigated.

Despite the nonlinear nature of the relationship between the boundary voltage and the conductivity distribution, a linear approximation is utilised to simplify the model. The electric field and equipotential lines for a uniform distribution and a distribution with two targets are shown in Figure 6.3. Figure 6.3 (a) shows a uniform distribution with a conductivity of 0.1 S/m when a current of 1 A is injected from adjacent electrodes. Figures 6.3 (b) and (c) show the electric field distribution in the presence of objects with high conductivities of 2 S/m and 10 S/m, respectively.

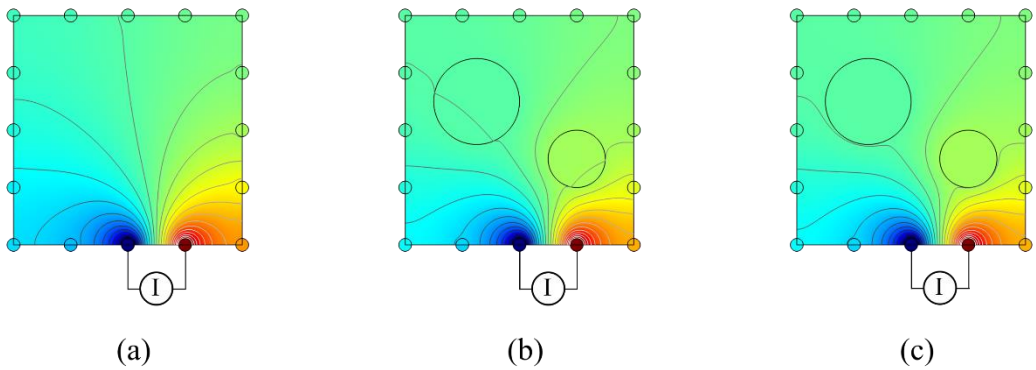

Figure 6.3: Comparison of electric field distribution. (a) Uniform distribution with conductivity 0.1 S/m. (b) Target object distribution with conductivity 2 S/m. (c) Target object distribution with conductivity 10 S/m.

As can be seen, there are two distinct characteristics in the electric field distribution within the ERT sensor:

- The electric field distribution is not uniform. Specifically, the equipotential lines are dense near the excitation electrode and sparse in the area far from the electrode.

- The conductivity distribution has an impact on the electric field distribution, particularly near the object edge where the equipotential lines are considerably deformed. Additionally, as the conductivity of the objects increases, the potential lines tend to bypass them rather than pass through them.

The sensitivity matrix $S_{n\times m}$ reflects the sensitivity of the voltage to changes in conductivity of each pixel. The sensitivity between the ith and jth electrode pair at position (x, y) can be calculated by:

$$S_{i,j}(x,y) = -\int_{p(x,y)} \frac{\nabla\emptyset_i(x,y)}{I_i} \cdot \frac{\nabla\emptyset_j(x,y)}{I_j} dxdy \tag{6.1}$$

where $\nabla\emptyset_i(x,y)$ and $\nabla\emptyset_j(x,y)$ are the electric potential distribution at the position (x, y) when the ith and jth injection currents are I_i and I_j, respectively. p(x, y)is the finite element to be solved.

The average sensitivity, which describes the contribution of each pixel to all boundary voltages, is calculated by averaging the values of each column of the sensitivity matrix. The average sensitivity for the three distributions is shown in Figure 6.4.

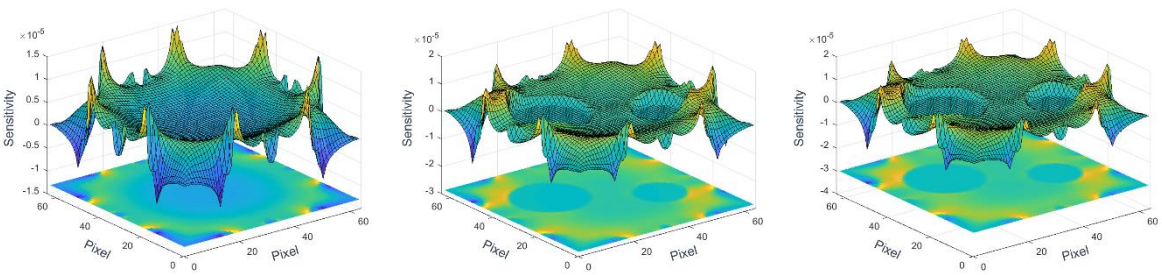

(a) (b) (c)

Figure 6.4: Comparison of average sensitivity distribution. (a) Uniform distribution with conductivity 0.1 S/m. (b) Target object distribution with conductivity 2 S/m. (c) Target object distribution with conductivity 10 S/m.

As previously noted, the sensitivity distribution is not uniform, and the boundary area has a larger sensitivity than the central region. This indicates that the conductivity change

near the electrode has a greater impact on the boundary voltage than the conductivity changes near the centre. As a result, the centre of the reconstructed image has more artefacts, which causes image distortion. Additionally, the sensitivity of the pixel where the objects are located is changed. It contains more information about the objects than the uniform sensitivity does.

However, the actual sensitivity matrix cannot be calculated when the conductivity distribution is unknown. Therefore, a uniform field sensitivity matrix, represented by S_0, is usually used by most image reconstruction algorithms. Object distributions with conductivity of 2 S/m and 100 S/m are used to calculate the actual sensitivity matrix, which are termed as S_2 and S_{100}, respectively. Figure 6.5 shows the reconstructed images using the Landweber algorithm after 100 iterations under different sensitivity matrix.

Conductivity of Objects	Sensitivity matrix		
	S_0	S_2	S_{100}
2 S/m	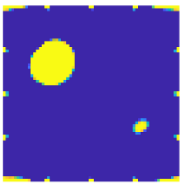		
100 S/m	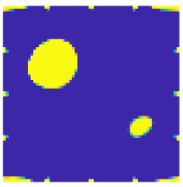		

Figure 6.5: Reconstructed images under different sensitivity matrix.

It is clear that the images obtained with the actual sensitivity matrix matches the actual distribution of conductivity. This demonstrates that when the actual sensitivity matrix is known, the error brought on by the inverse problem can be disregarded. The image that is reconstructed with S_0, however, exhibits obvious artefacts at the object boundary. The

shape of the objects is essentially unrecognisable. This further illustrates that the linear approximation of the nonlinear relationship between the conductivity change and the boundary voltage change is the main cause of image distortion.

6.3 Image reconstruction based on wavelet image fusion

6.3.1 Sensitivity matrix normalisation

The mathematical model of ERT is described as:

$$U = S \times \sigma \tag{6.2}$$

where U is the independent boundary voltage, S is the sensitivity matrix and σ is the conductivity distribution.

Image reconstruction is the process of solving the conductivity distribution when S and U are known.

$$\sigma = S^{-1} \times U \tag{6.3}$$

Due to the nonlinearity and ill-pose of the inverse problem, the sensitivity matrix directly affects the quality of the reconstructed image. The impact of soft fields can be greatly diminished by normalising the sensitivity matrix.

The most widely used form to normalise the sensitivity matrix $S_{m \times n}$, is

$$S_{norm} = \frac{S_{i,j}}{\sum_{j=1}^{m} S_{i,j}} \tag{6.4}$$

where S_{norm} is the normalised sensitivity matrix.

The matrix form of equation (6.4) can be written as the left multiplied by a weight matrix W:

$$S_{norm} = W \times S \tag{6.5}$$

where $W = \text{diag}\left(\left(\sum_{j=1}^{m} S_{i,j}\right)^{-1}\right)$.

Thus, equation (6.2) and equation (6.3) can be rewritten as:

$$W \times U = S_{norm} \times \sigma \tag{6.6}$$

$$\sigma = S_{norm}^{-1} \times W \times U \tag{6.7}$$

This method normalises the sensitivity of all pixels under the same electrode pair. In view of the difference in the sensitivity of the same pixel to different measured voltages, a normalisation method based on each pixel is introduced, i.e. the right is multiplied by a weight matrix W_p on the original sensitivity matrix:

$$S_{norm} = S \times W_p \tag{6.8}$$

In this case, equation (6.2) and equation (6.3) are converted to:

$$U = S_{norm} \times W_p^{-1} \times \sigma \tag{6.9}$$

$$\sigma = W_p \times S_{norm}^{-1} \times U \tag{6.10}$$

For comparison, W_p is defined as $\text{diag}\left(\left(\sum_{i=1}^{n} \left| S_{i,j} \right|\right)^{-1}\right)$ and $\text{diag}\left(\left(\sum_{i=1}^{n} S_{i,j}^{2}\right)^{-1/2}\right)$, respectively.

The above three normalisation methods are named as Norm 1, Norm 2 and Norm 3, respectively. For adjacent excitation and measurement strategies, the sensitivity maps between electrode pairs 1-3, 1-5, 1-7, 1-9 and average sensitivity distribution are shown in Figure 6.6.

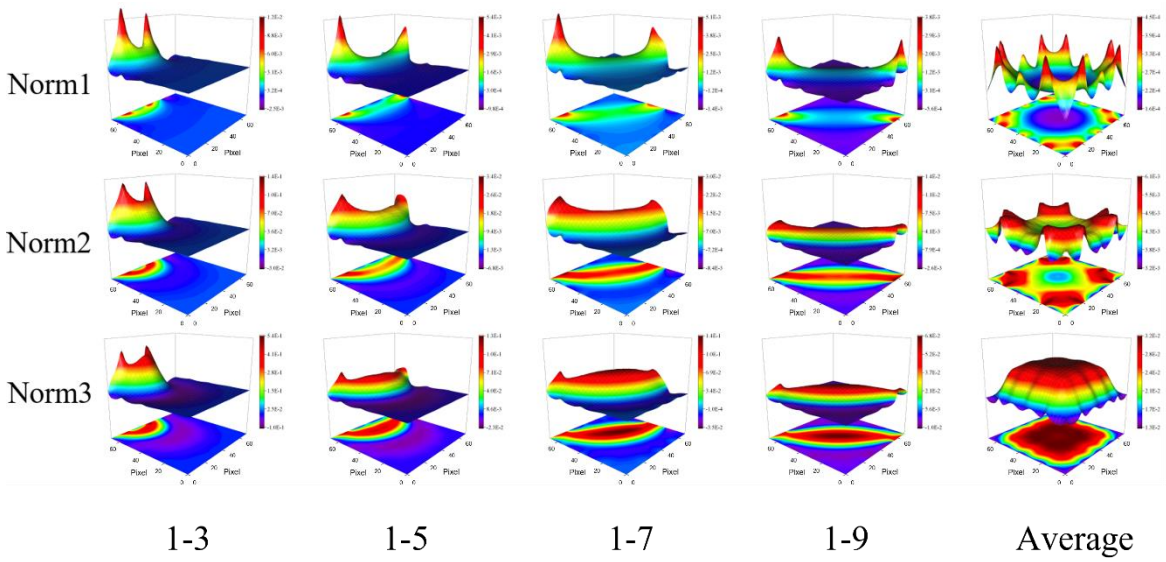

Figure 6.6: Comparison of sensitivity distribution under different normalisation methods.

The sensitivity distribution of Norm 1 is similar to the original sensitivity distribution as shown in Figure 6.4, the sensitivity is low in the central area and high near the boundary. While Norm 2 and Norm 3 effectively reduce this difference, the sensitivity distribution is more uniform, especially Norm 3, which greatly improves the sensitivity in the central area.

Uniformity P is introduced as the evaluation index of the sensitivity field:

$$S_n^{avg} = \frac{1}{M}\sum_{m=1}^{M} S_{n,m} \tag{6.11}$$

$$S_n^{dev} = \sqrt{\frac{1}{M-1}\sum_{m=1}^{M}(S_{n,m} - S_n^{avg})^2} \tag{6.12}$$

$$P_n = \frac{S_n^{dev}}{S_n^{avg}} \tag{6.13}$$

$$P = \sum_{n=1}^{N} |P_n| \tag{6.14}$$

The smaller P, the smaller difference of the sensitivity matrix (de Lima *et al.*, 2007). The uniformity of the three normalised sensitivity matrix is shown in Table 6.1. Norm 3 has the best sensitivity field uniformity, which is consistent with the previous conclusion.

Table 6.1: Comparison of uniformity under different normalisation method.

Normalisation Method	Norm1	Norm2	Norm3
P	60.3	42.4	32.6

The second step of pre-processing is to use a mean filter to further reduce the difference in sensitivity distribution. The principle of mean filter is similar to convolution, i.e. each pixel value in an image is replaced with the mean value of its neighbours. Figure 6.7 shows the average sensitivity distribution after filtering with a size of 5×5 mean filter. Compared with Figure 6.6, the sensitivity is more uniform.

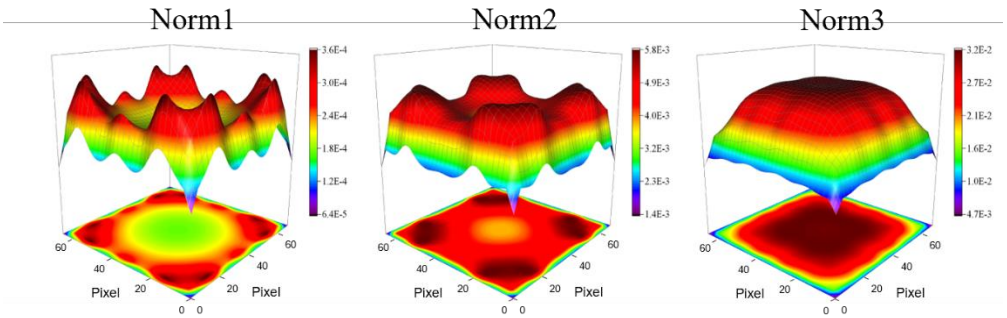

Figure 6.7: Average sensitivity distribution with 5×5 mean filtering.

6.3.2 Image fusion based on DWT

Image fusion is a technique used to combine several images into one image, which typically contains more information. In this section, images that have been reconstructed using different sensitivity matrix are combined using discrete wavelet transform (DWT). The image fusion process based on DWT is shown in Figure 6.8. As an illustration, let's consider the one-level DWT image fusion. The low frequency component and high frequency components of the two original images are represented by DWT as an

approximate image (A) and three detailed images (HD, VD, and DD) (Pajares and De La Cruz, 2004). The matching components are fused in accordance with the prescribed rules, and the inverse DWT is then employed to create the final fused image.

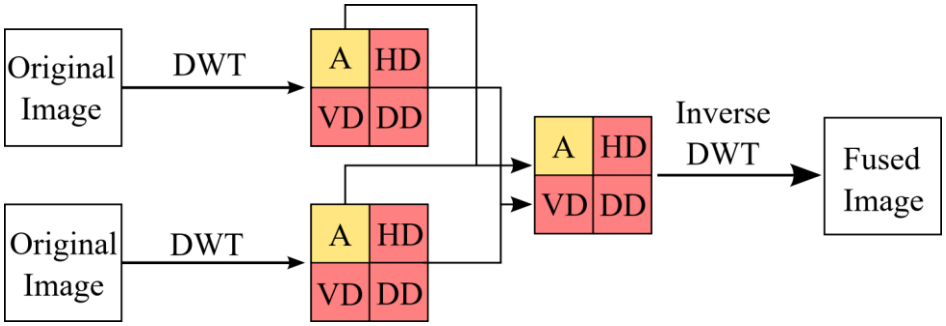

Figure 6.8: Diagram of one-level DWT image fusion.

The choice of the fusion rule is directly related to the image quality. For the reconstructed image of ERT, its low frequency component determines the overall shape of the image and reflects the average characteristics of the image. The boundary information is extracted by the high frequency component. Therefore, the low frequency and high frequency components of the decomposed image are combined using a weighted average rule and the largest absolute value rule.

6.3.3 Simulation results

For this work, COMSOL 5.6 is used to build the sensor model as shown in Figure 6.1 (a). The initial conductivity of the material is set to 0.1 S/m and a target object with high conductivity (2 S/m) is set to simulate external pressure. Adjacent current excitation and adjacent voltage measurement are used, and the injection current is 1 A. The imaging area is divided into 64×64 with a total of 4096 pixels.

Single target object

First, the position detection performance of a single target object is evaluated. A circular object with a diameter of 10 mm is placed in seven positions of the sensor, as shown in Figure 6.9 (a). Due to the symmetry of the square sensor, these seven positions can be used to evaluate the overall sensitivity distribution. The LBP algorithm is used to reconstruct the image because the position detection of a single point emphasises real-time performance over image quality.

The reconstructed images with normalised sensitivity matrix Norm 1, Norm 2 and Norm 3 are shown in Figure 6.9 (b). The real target position is indicated by the red circle and the centre coordinate of the binary picture is represented by the red cross. As the target object gets closer to the boundary, the image of Norm 1 suffers from severe distortion.

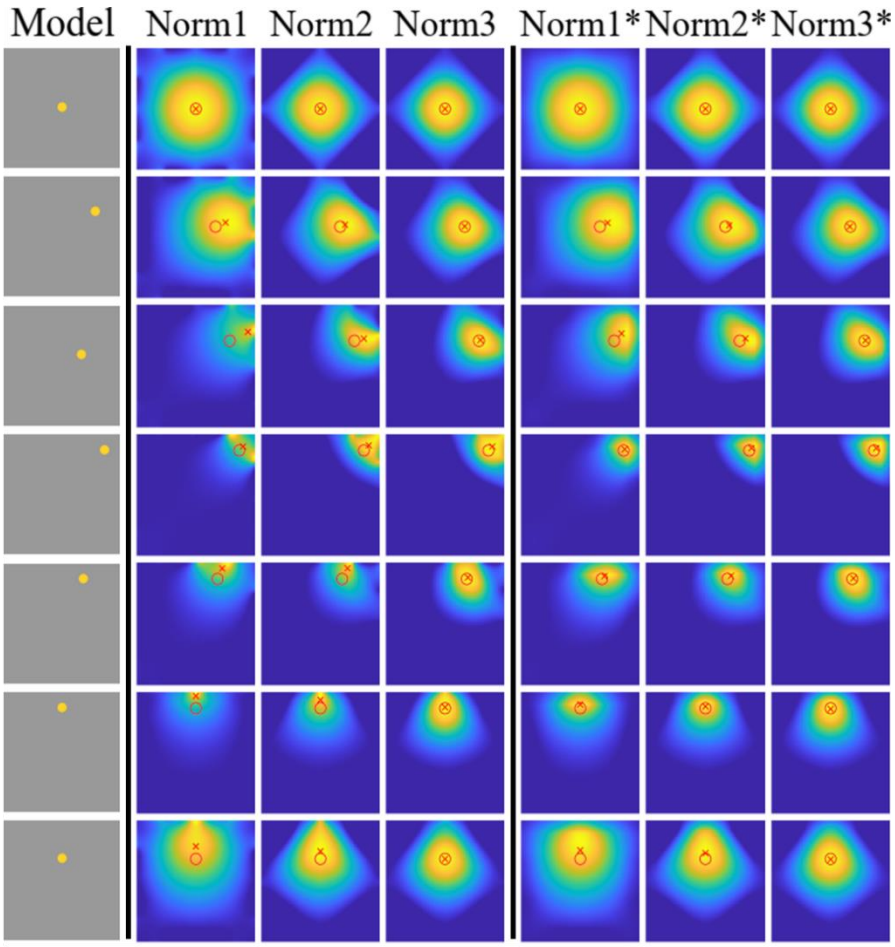

(a) (b) (c)

Figure 6.9: Comparison of reconstructed images with and without mean filtering. * means the sensitivity matrix is processed by mean filter.

The number of artefacts is lower with the latter two due to the more uniform sensitivity distribution. Even when it is close to the boundary, they can still provide useful information. Among them, Norm 3 has the highest accuracy.

Multi-target objects

Six distributions built by COMSOL are shown in Figure 6.10, with the number of objects ranging from 1 to 5. The Landweber algorithm is used to obtain more accurate images because the LBP algorithm is no longer applicable for the detection of multi-objects.

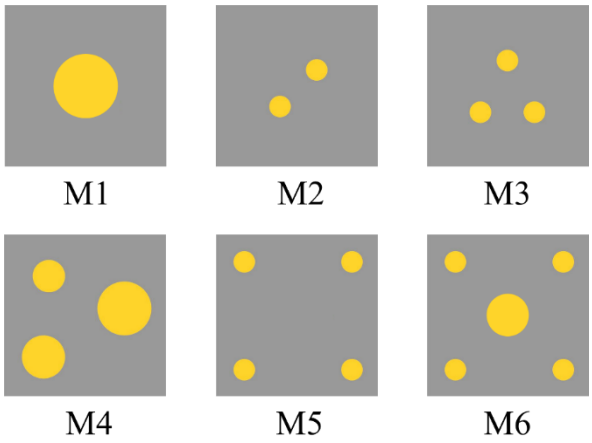

Figure 6.10: Six objects distributions model.

The images after 100 iterations are shown in Figure 6.11 (b-d). The objects in M2 and M3 cannot be distinguished because the sensitivity of Norm 1 in the central region is lower than that near the electrode. The results of Norm 2 are much better than that of Norm 1, although they still contain some artefacts. As Norm 3 has the highest sensitivity in the central area, it can differentiate the targets in the centre with excellent precision. However, Norm 2 and Norm 3 are not sensitive to the size of the target, while the result of Norm 1 is similar to the actual distribution.

To further improve the image accuracy, the image results of Norm 1 and Norm 3 are used as original images, and the proposed method based on DWT is used for image fusion. Through multiple simulation, the Haar function is selected for wavelet transform and the

decomposition level is set to 3. To reduce the distortion caused by image fusion, the fused image is filtered by a 7×7 mean filter, and the result is shown in Figure 6.11 (e). The fused image combines the characteristics of the original images and has a better resolution than a single image. It can not only separate the target objects in the central area, but also distinguish the size of the target objects.

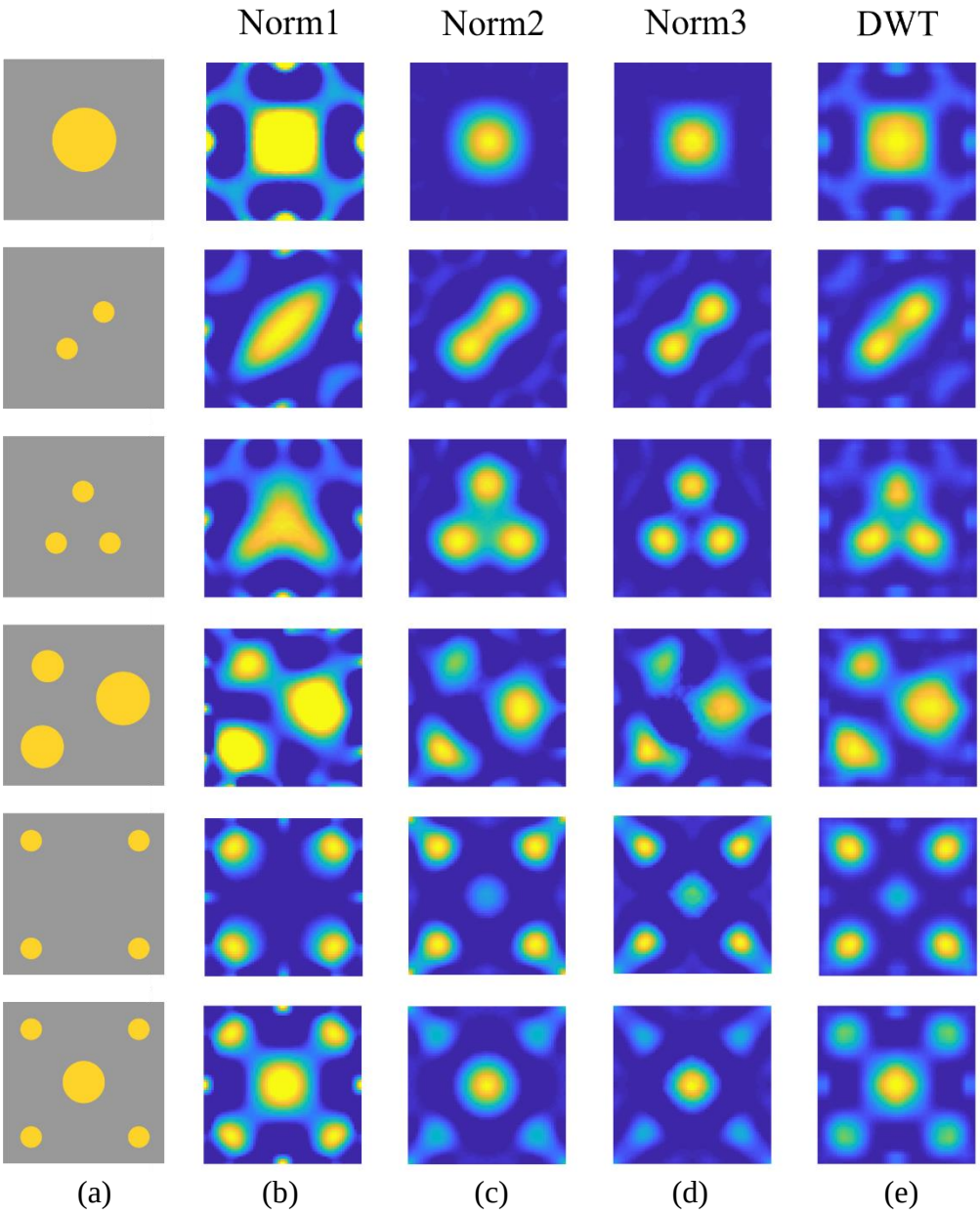

Figure 6.11: Comparison of reconstructed images of multi-target objects.

Table 6.2 and Table 6.3 list the correlation coefficients and image errors. The average values in both tables demonstrate the improvement of the overall image resolution of the fused image.

Table 6.2: Correlation coefficient comparison between single image and fused image.

Correlation Coefficient	M1	M2	M3	M4	M5	M6	Average
Norm 1	0.84	0.51	0.43	0.88	0.75	0.84	0.71
Norm 2	0.65	0.60	0.65	0.64	0.78	0.54	0.64
Norm 3	0.64	0.77	0.74	0.57	0.66	0.47	0.64
DWT	0.94	0.66	0.82	0.84	0.74	0.60	0.77

Table 6.3: Image error comparison between single image and fused image.

Image Error	M1	M2	M3	M4	M5	M6	Average
Norm 1	18%	23%	25%	15%	15%	16%	19%
Norm 2	22%	19%	19%	25%	14%	24%	20%
Norm 3	23%	11%	14%	27%	16%	25%	19%
DWT	11%	16%	12%	17%	14%	22%	15%

6.4 Multi-target extracted method based on PSO algorithm

Traditional imaging methods are unable to solve the problem of blurring imaging borders for the application of multiple objects, which causes inaccurate estimates of the position and size of objects. This section proposes a new method by combining image processing techniques and optimisation algorithms to extract target information in reconstructed images.

6.4.1 Localisation method based on k-means clustering

It is vital to use tactile sensing to determine the contact position of the target object in the practical application of robotics or human-computer interaction. However, this is difficult for low-resolution images reconstructed by ERT. When there are several targets close to one another, localisation becomes more challenging. The k-means clustering algorithm is applied to determine the coordinates of several targets.

K-means clustering algorithm

K-means clustering is an unsupervised observational learning algorithm. Due to its simplicity, efficiency and excellent performance, it has been one of the most popular clustering algorithms (Adnan *et al.*, 2021). The algorithm works by repeatedly reducing the distance between the centre of the cluster and all the data. The goal of the algorithm is to split all the data into k clusters, the data that are highly similar to each other and have few differences are allocated to one cluster. The following are the detailed steps:

STEP 1: Obtain the reconstructed image using the Landweber algorithm, then threshold the image to remove part of the artefacts. This yields the collection of pixel locations X:

$$X = \{x_i | x_i \in R^d, i = 1, 2, \cdots, n\} \tag{6.15}$$

where $x_1, x_2, \cdots x_n$ are the n pixel coordinates of the image. d is the dimension of the data. Here, d=2, which means that each pixel is represented by the horizontal and vertical coordinates.

STEP 2: Determine the k value based on the known number of targets, and randomly select k initial cluster centres:

$$C = \{c_j | c_j \in R^d, j = 1, 2, \cdots, k\} \tag{6.16}$$

STEP 3: Calculate the Euclidean distance between all pixels x_i and cluster centres c_j:

$$D(x_i, c_j) = \|x_i - c_j\|^2, i = 1, 2, \cdots n;\ j = 1, 2, \cdots, k \tag{6.17}$$

STEP 4: Using the minimum distance as the criterion, all pixels x_i are assigned to the cluster where the closest cluster centre is located.

STEP 5: Calculate the mean of all pixel coordinates within the cluster as the new cluster centre.

STEP 6: Repeat STEP 3 to STEP 5 until the cluster centre does not change or the specified number of iterations is reached.

Automatic update of k value

The k-means algorithm requires the k value to be specified in advance, which is usually determined by experience. However, the number of target items is typically unknown in practical situations. Therefore, an improved k-means algorithm based on automatic selection of k value is suggested. The flowchart of the improved k-means algorithm is shown in Figure 6.12.

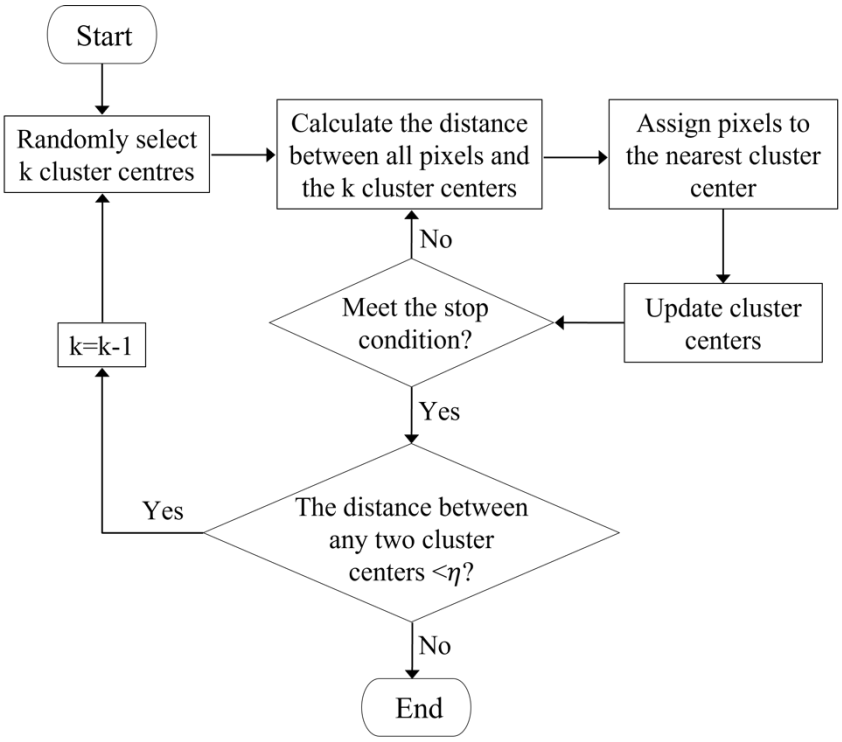

Figure 6.12: Flow chart of k-means algorithm.

STEP 1: Initialise k to the maximum value of the expected number of targets and use standard k-means algorithm to obtain k cluster centres C.

STEP 2: Use equation (6.17) to calculate the Euclidean distance D_c of all cluster centres in turn:

$$D_c = \{D(c_{1,}\, c_2), D(c_{1,}\, c_2), \cdots, D(c_{k-1,}\, c_k)\} \tag{6.18}$$

STEP 3: Set parameter η as the resolution distance. If any value of D_c is less than η, it is considered that the corresponding cluster centres are in the same target, the value of k is reduced by 1.

STEP 4: The iteration is repeated until all the values of D_c are greater than η.

Selection of initial cluster centres

Note that the initial cluster centre has a great influence on the final clustering result. If the initial cluster centre is improperly chosen, the algorithm will fall into a local optimal solution. Therefore, the pre-clustering method is used to choose the initial cluster centre.

Specifically, m groups of cluster centres are randomly selected, and total distance from all pixels to each group of cluster centres calculated:

$$D_m = \sum_{j=1}^{k}\sum_{i=1}^{n}\left\|x_i - c_{m,j}\right\|^2, i = 1, 2, \cdots n;\ j = 1, 2, \cdots, k \tag{6.19}$$

The group with the smallest D_m is used as the initial cluster centre. It has been verified that this method can effectively avoid convergence to the local optimal solution.

The reconstructed images after 100 iterations using the Landweber algorithm are shown in Figure 6.13 (b), followed by the binary images after thresholding in Figure 6.13 (c).

Figure 6.13 (d) shows the target position obtained by the above improved k-means algorithm and the centre of each target is marked with '+' in yellow.

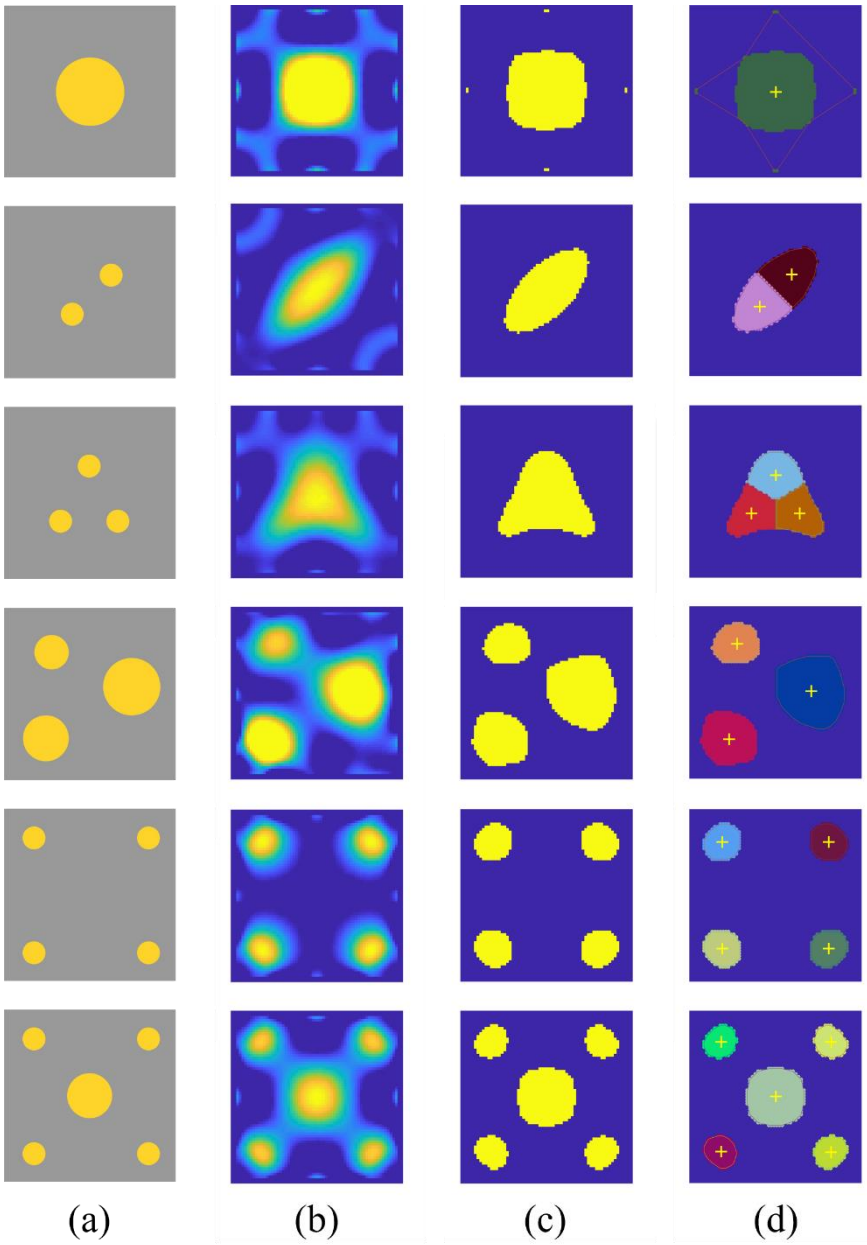

Figure 6.13: Target localisation results based on automatically selected k values. (a) Actual distribution. (b) Reconstructed image. (c) Binary image. (d) Target localisation.

The initial value of k is 5. As illustrated, the improved k-means algorithm can modify the k value in accordance with the target distribution. The calculated position is consistent with the actual distribution. However, M2 and M3 cannot be distinguished in the reconstructed images due to the closeness of the targets. The proposed algorithm can

automatically identify the number of targets and estimate the target location in good accuracy.

Position error (PE) is used to measure the discrepancy between the obtained coordinates and the actual coordinates:

$$PE = \frac{1}{k}\sum_{i=1}^{k}\frac{\|C_i' - C_i\|^2}{\|C_i\|^2} \times 100\% \tag{6.19}$$

where C_i' is the calculated centre coordinate, C_i is the actual centre coordinate, and k is the number of targets.

The position errors of the six distributions are shown in Table 6.4. M1 has the smallest error of only 0.11%, while the largest error occurs in the M3, which is 4.17%.

Table 6.4: Position error of target localization.

Model	**M1**	**M2**	**M3**	**M4**	**M5**	**M6**
Position Error	0.11%	2.62%	4.17%	1.93%	2.82%	1.08%

The effect of the number of iterations of the Landweber algorithm on the position error is studied. It is found that when the number of iterations exceeds 200, the determination of the k value is wrong. Therefore, the position errors under the iterations of 50, 100, 150 and 200 are compared, as shown in Figure 6.14. As the number of iterations increases, there is a little but noticeable decrease for the overall position error. Taking into account the execution time of the algorithm, the result under 100 iterations is selected as the optimal solution. In that case, the position error is within an acceptable range.

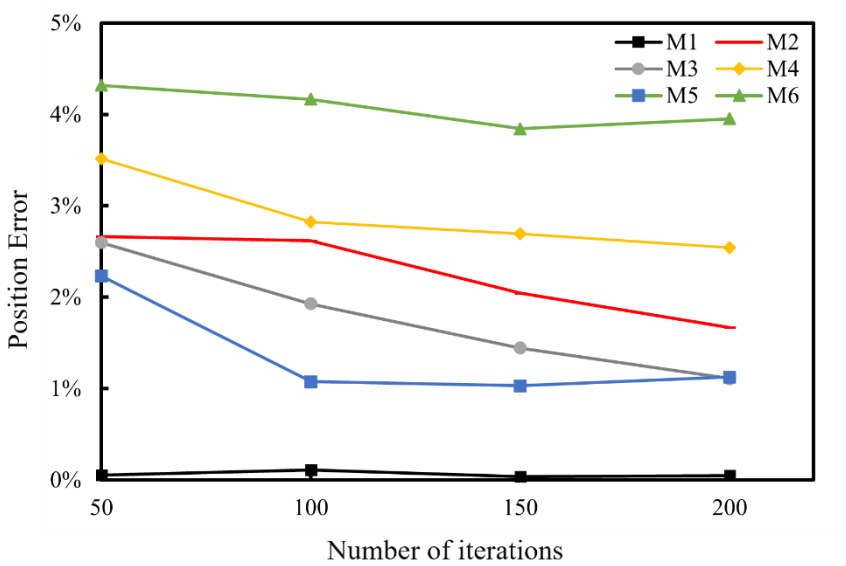

Figure 6.14: Position error of target localisation.

6.4.2 Shape estimation based on edge detection

Assuming the targets are all circular, the radius of each target can be obtained with the known centre coordinates. The image reconstructed by the Landweber algorithm is not accurate enough to directly extract reliable object information, but it still provides some useful information. Although the absolute sizes of each target cannot be accurately determined, the reconstructed image can indicate the relative sizes of the objects. In other words, a large target occupies more pixels than a small target. Thus, a novel approach to predicting the target distribution has been developed, as seen in Figure 6.15.

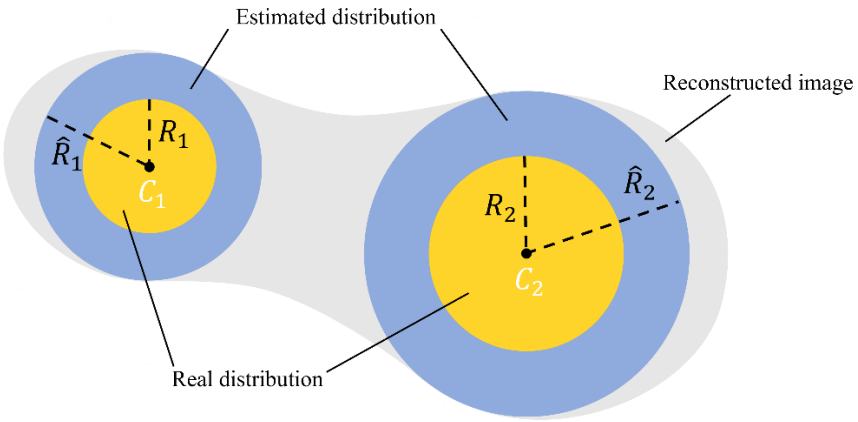

Figure 6.15: Flow chart of k-means algorithm.

The centre coordinate C_i $(i = 1, 2, \cdots, k)$ has been calculated by the improved k-means clustering algorithm. The radius of the circle R_i is defined as the closest distance from C_i to the edge of the image. The initial distribution estimate is denoted as $\hat{\sigma}(C_k, \hat{R}_k)$. Theoretically, $\hat{R}_k$ is proportional to the radius of the actual target R_k. Thus, a scaling function ρ is defined, which implements scaling for all circles. Therefore, equation (6.20) is used as the objective function to solve the optimal solution of ρ.

$$\min \left\| S \cdot \sigma\left(C_k, \rho_k \cdot \hat{R}_k\right) - U \right\| \tag{6.20}$$

where S is the normalised sensitivity matrix, U is the normalised boundary voltage and $\sigma\left(C_k, \rho \cdot \hat{R}_k\right)$ is the estimated target distribution.

Edge detection

Before solving the scaling factor ρ, it is necessary to obtain the edge coordinates of the image. Edge detection is based on the feature that the image intensity of the edge changes considerably compared to the image intensity of the nearby pixels. The edge information can be obtained by calculating the first-order derivative or the second-order derivative of the image. Because the image is a two-dimensional plane, it is equivalent to a function of the image intensity in the horizontal and vertical directions. Mathematically, the approximation of the derivative of a pixel is performed by convolution with the specified operator and the edge of the image is defined as the pixel with the highest value. Roberts, Prewitt and Sobel operators are the most commonly used operators (Chaple *et al.*, 2015). These three operators have a suppressive impact on noise and require less computation. Among them, the Sobel operator conducts a weighted average on the influence of the pixel position, which removes noise interference. Also, the quality of edge detection is better compared to Prewitt operator and Roberts operator.

In the case that the image intensity of the edge is smooth, the first order derivative may not be able to extract the edge, while the second order derivative can provide more useful information. The position of the corresponding edge is determined by the second order derivative using the zero-crossing point. Before edge detection, the image often needs to be filtered to remove the noise. Canny edge detector is recognised as one of the best edge detection algorithms (Bao *et al.*, 2005). It calculates the gradient magnitude and direction based on first-order differential, and introduces non-maximum suppression and double threshold detection. The Canny edge detector is more precise yet costly to compute, making it appropriate for applications that need high precision.

As shown in Figure 6.13 (c), the original images for edge extraction are binarised images. Taking M4 as an example, four operators are used to extract its edge information. As shown in Figure 6.16, the edge obtained by the Canny operator does not have any evident advantages over the other three. To extract the edge of the image, the Sobel operator is chosen as a trade-off between computation cost and performance.

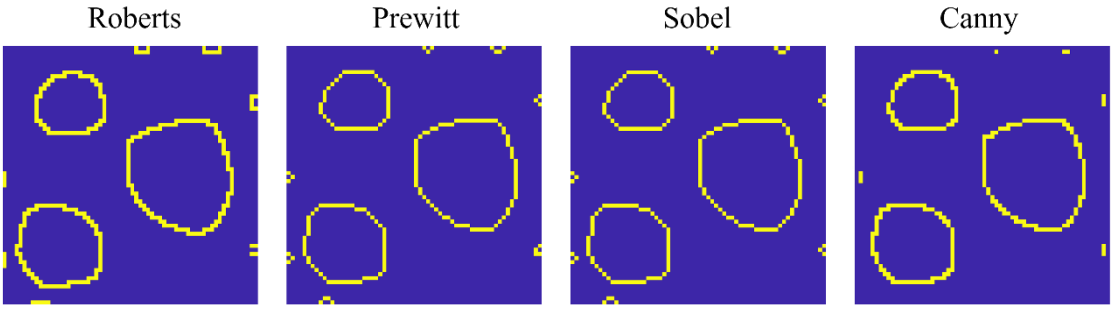

Figure 6.16: Edge detection with different operators.

Figure 6.17 depicts the edges of the six distribution models using the Sobel operator. It can be seen that the coordinates of the edges of the binary image are accurately extracted. Combined with the calculated centre coordinates of the targets, the initial distribution estimate can be obtained by using the method illustrated in Figure 6.15.

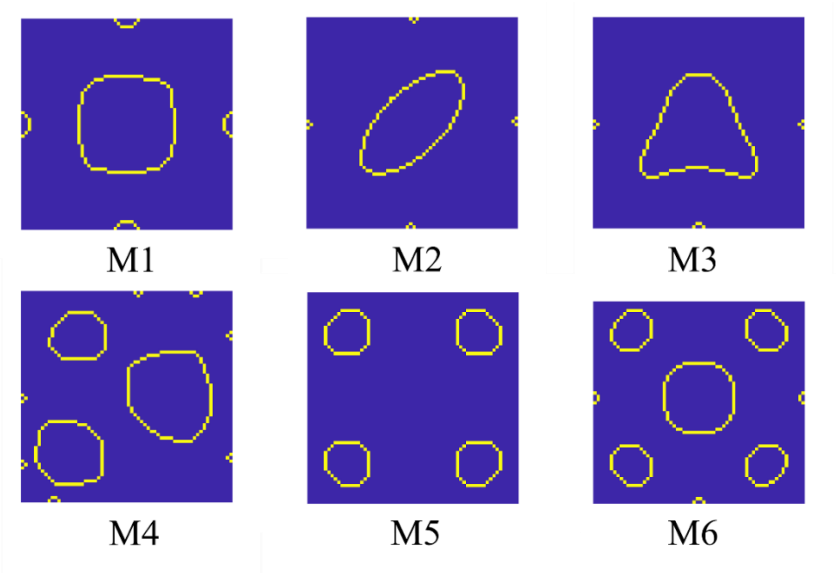

Figure 6.17: Edge detection of different distributions based on Sobel operator.

6.4.3 Radius calculation based on PSO algorithm

Particle swarm optimisation (PSO) is a global optimisation algorithm, which originated from the research on the predation behaviour of birds (Kennedy and Eberhart, 1995). The PSO algorithm is easy to implement and does not have many parameters to adjust. It has been widely used to solve multi-objective optimisation problems.

A population (referred to as a swarm) in this algorithm is made up of N particles. Each particle contains a D-dimensional position vector x_i and a D-dimensional velocity vector v_i. The position vector x_i represents a candidate solution to the optimisation problem. To promote the convergence of the algorithm, the position is updated iteratively using the velocity vector v_i. The update equations of x_i and v_i are as follows.

$$v_i(t+1) = w(t) \cdot v_i(t) + c_1 r_{1i}\big(p_i(t) - x_i(t)\big) + c_2 r_{2i}\big(g_i(t) - x_i(t)\big) \tag{6.21}$$

$$x_i(t+1) = x_i(t) + v_i(t+1) \tag{6.22}$$

where $w(t)$ is the inertia weight, t represents the current number of iterations, i represents the i-th particle ($i = 1, 2, \ldots, N$), N represents the size of the swarm. p_i is the best-known position searched by particle i, and g_i is the best-known position searched by the entire swarm in one iteration. c_1 and c_2 are non-negative learning factors used to adjust the influence of p_i and g_i on particles. r_{1i} and r_{2i} are independent random numbers within [0, 1].

In the process of searching for the global optimal solution, the position of particle i is evaluated by the determined objective function. The best-known position of particle i will be shared with the swarm and, likewise, the best-known position of the entire swarm is obtained. During the process, particle i adjusts the search direction according to the best-known position of the current particle and the swarm, and continuously approach the global optimal solution.

The inertia weight $w(t)$ plays a role in coordinating the global and local search capabilities of the swarm. Fixed inertia weights tend to fall into local best positions during optimisation (Shi, 2004). To improve the global search ability of the algorithm, a larger inertia weight should be selected at the beginning of the algorithm iteration to broaden the search range. As the number of iterations increases, a small inertia weight is more beneficial for the algorithm to find the optimal solution accurately (Abido, 2002).

The classical linear decreasing method is adopted here to change the inertia weight factor, the iterative equation is defined as:

$$w(t) = w_{start} - \frac{w_{start} - w_{end}}{\text{MaxEpochs}} \text{Epochs} \tag{6.23}$$

where w_{start} and w_{end} represents the initial value and the termination value of the inertia weight, respectively. $Epochs$ represents the current number of iterations, $MaxEpochs$ represents the maximum number of iterations.

The PSO algorithm is then:

(1) Initialise the parameters, calculate the objective function value of each particle and obtain the best-known position of the swarm g_i.

(2) According to equation (6.21) and equation (6.22), update the velocity and position of particles.

(3) Compare the objective function value of each particle with that of p_i and g_i, and update p_i and g_i.

(4) The iteration ends when the maximum number of iterations is reached or the objective function value of g_i meet the pre-set minimum error. Otherwise, go back to (2).

Objective function

The objective function, as mentioned above, determines the iterative updates of particle optimal p_i and swarm optimal g_i. For ERT, the objective function is typically regarded to be the minimal difference between the measured voltage and the voltage calculated from the reconstructed image, as shown in equation (6.24).

$$\min \ \|S \cdot \sigma - U\| \tag{6.24}$$

However, the sensitivity matrix changes with the conductivity distribution. Errors are definitely introduced when the uniform field sensitivity matrix is used instead of the object field sensitivity matrix. Therefore, even if equation (6.24) can converge to the global optimal solution, there is still a significant difference between the optimal solution

and the actual conductivity. As a result, the sensitivity matrix in the objective function needs to be corrected according to the actual conductivity distribution.

Because the actual distribution of the conductivity is unknown, Zhang (2013) proposed to use the reconstructed image obtained by the Landweber algorithm as the basis for updating the sensitivity matrix. Chen *et al.* (2019) introduced a penalty factor to modify the sensitivity to obtain an approximation of the actual sensitivity matrix. However, these methods take a lot of time to calculate the sensitivity matrix in the forward problem, and so they are not suitable for real-time applications.

Compare the actual sensitivity distribution with the sensitivity distribution for a uniform field in Figure 6.4 (a-b). The difference in sensitivity between the two lies in the pixel where the targets are located. Figure 6.18 shows the ratio of the average sensitivity under two distributions. It is considered that the actual sensitivity distribution can be obtained by proportionally magnifying the uniform sensitivity at the pixel where the targets are located.

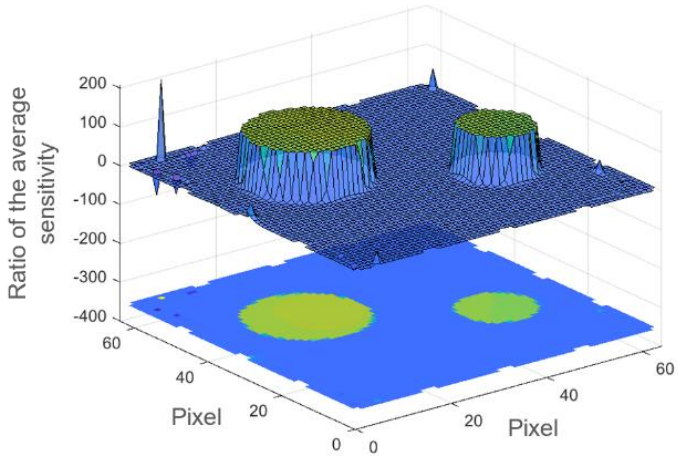

Figure 6.18: The ratio of the average sensitivity of the empty field to the average sensitivity of the object field.

Therefore, suppose there is a factor μ, the correction from the uniform sensitivity matrix S_0 to the real sensitivity matrix S can be achieved through equation (6.25).

$$S = S_0 \cdot \mathrm{diag}(\mu\sigma) \tag{6.25}$$

where σ is the actual conductivity distribution, which is unknown, and so it is replaced by the binary image σ_L reconstructed by Landweber algorithm.

The modified objective function is yielded by integrating equation (6.25) into equation (6.20):

$$\min\left\|S_0 \cdot \mathrm{diag}(\mu\sigma_L) \cdot \sigma\left(C_k, \rho_k \cdot \widehat{R}_k\right) - U\right\| \tag{6.26}$$

6.4.4 Simulation result

Figure 6.19 is the estimated distribution using the above method. The population size of the PSO algorithm is 10, the maximum number of iterations is 50, and both c1 and c2 are 1.4. Figure 6.19 (b) has a correction factor of 1, which is identical to using a uniformly distributed sensitivity matrix. Due to the approximation error of the sensitivity matrix, the extracted shape is slightly different from the actual distribution. For comparison, the correction factors for Figure 6.19 (c-d) are 1.8 and 2.5, respectively. As can be seen, a more accurate result can be obtained by choosing an appropriate correction factor.

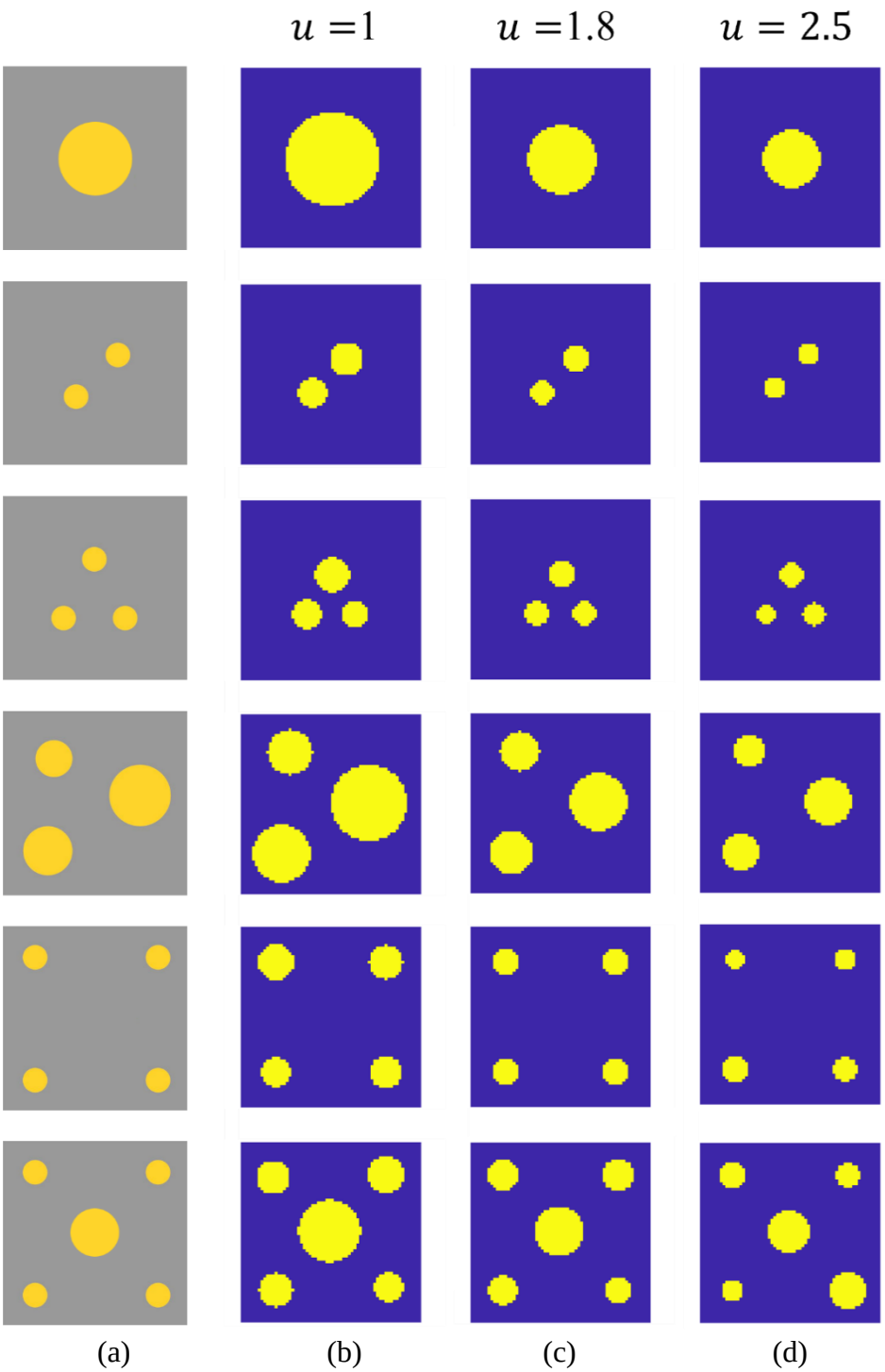

Figure 6.19: Distribution estimation using different u values.

To analyse the influence of u value on the results of image extraction, Figure 6.20 shows the image error and correlation coefficient of the extracted images for six distributions under various u values. As the value of u increases, the image error falls and the correlation coefficient rises. This shows the effectiveness of modifying the sensitivity

matrix to improve image quality. However, further increasing the value of u does not significantly improve the image, and some images even tend to deteriorate. The average of image error and correlation coefficient are shown in Figure 6.21. As shown, low image error and a high correlation coefficient are present when the value of u is in the range of 1.8-1.9.

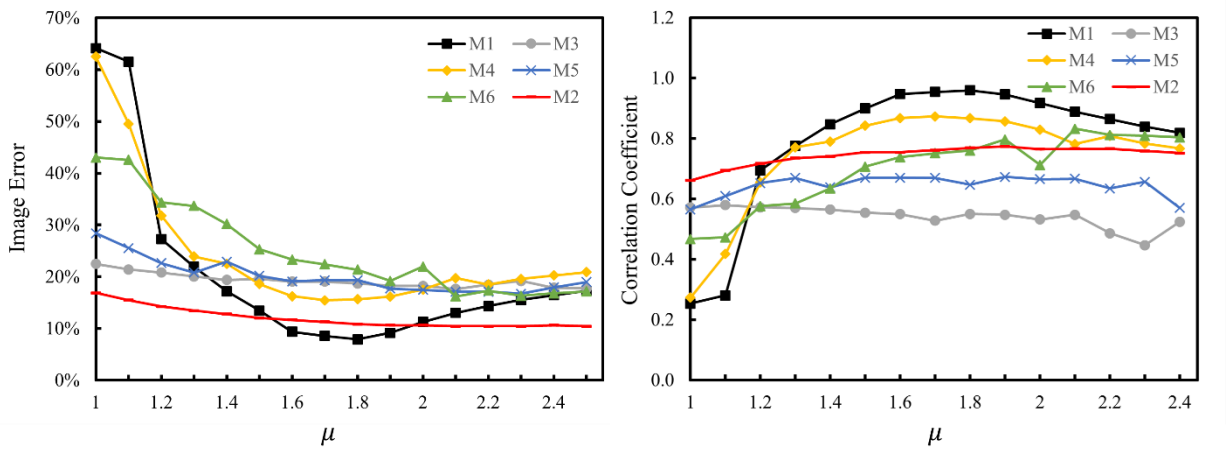

Figure 6.20: Image error and correlation coefficient.

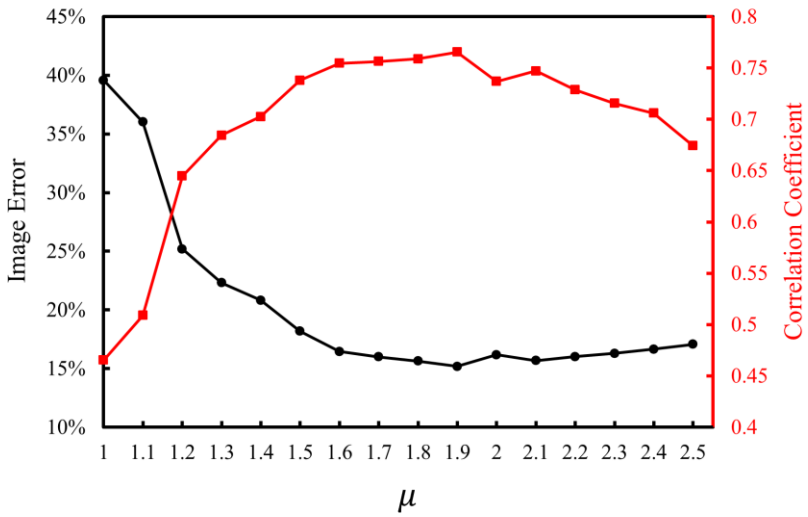

Figure 6.21: Average of image error and correlation coefficient.

6.5 Experimental validation

6.5.1 Experiment setup

To verify the feasibility of the proposed method, an ERT system is built, as shown in Figure 6.22. A voltage-controlled current source (VCCS) outputs an AC current with an

amplitude of 100 mA and frequency of 50 kHz. Four 16-channel multiplexers (ADG1606) are controlled by Arduino Nano to switch between electrodes to complete current excitation and voltage measurement. Because only the conductivity is considered, the RMS value of the voltage is taken as the final data. The collected data is uploaded to the PC through the serial port, followed by data processing and algorithms, which are implemented in MatLab. Due to the limited measurement accuracy and speed, this system is only used for static measurement.

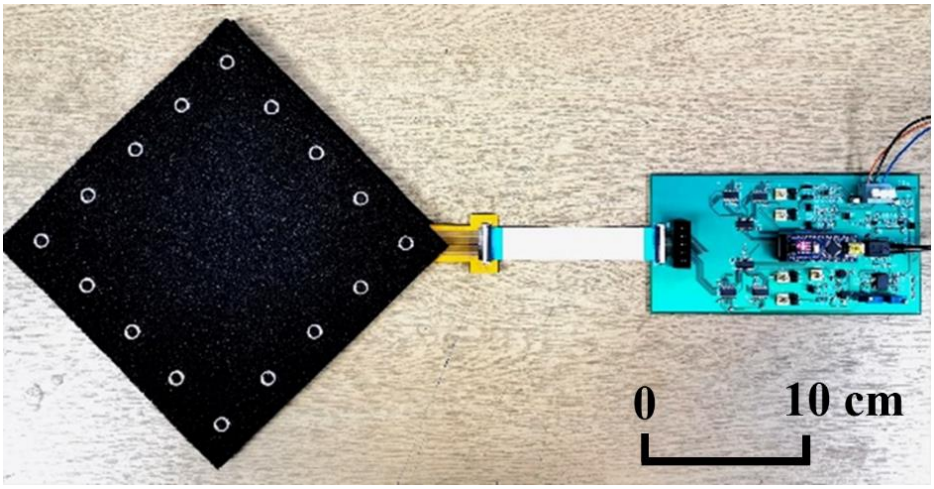

Figure 6.22: Flexible ERT tactile sensing system.

6.5.2 Experiment results and discussion

Different magnitudes of pressure applied to the conductive foam cause different conductivity changes. Standard geometry for applying pressure is manufactured via 3D printing. As shown in Figure 6.23, two cylinders are used for the initial pressure distribution. Additional pressure is applied on top of the surface by finger. The effect of pressure on conductivity can be reflected by the amplitude change of the reconstructed 3D image. Iterations are performed 100 times using Landweber algorithm based on the sensitivity matrix normalised by Norm1. The images contain several artefacts, which are ascribed to fabrication errors in the sensor, measurement errors, and environmental interference. The two major peaks of the image are prominent, and the artifacts can be

removed by further filtering. Despite this, this test verifies the ability of the ERT-based tactile sensor for pressure amplitude detection.

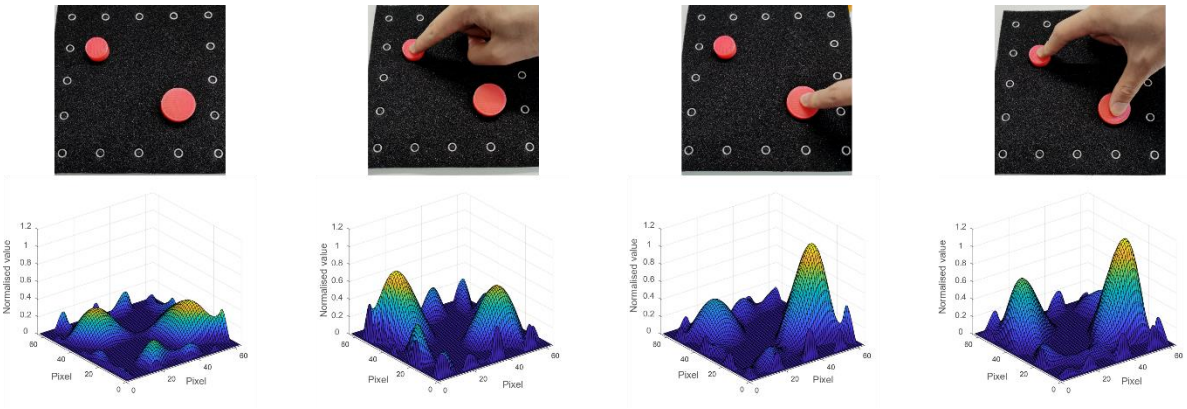

Figure 6.23: Imaging results at different pressure amplitudes.

Figure 6.24 compares the reconstructed images of different methods under five pressure distributions. The pressure is applied by cylinders of different sizes. During experimental measurement, the standard weights are placed on the top of the cylinder to obtain stable and effective voltage data.

The five methods compared include the Landweber algorithm based on three sensitivity normalisations (referred to as Norm1, Norm2 and Norm3), followed by the fused image obtained by DWT image fusion and the image extracted by PSO algorithm. The Landweber algorithm runs 100 times to produce the original image. Norm 1 and Norm 2 are used as the original images for the fusion algorithm since Norm 2 is more stable than Norm 3 in practical test. Harr is chosen as the wavelet basis function and the number of decomposition layers is set to 4. The scaling factor of the PSO algorithm is set to 1.9, the remaining parameters are consistent with the simulation.

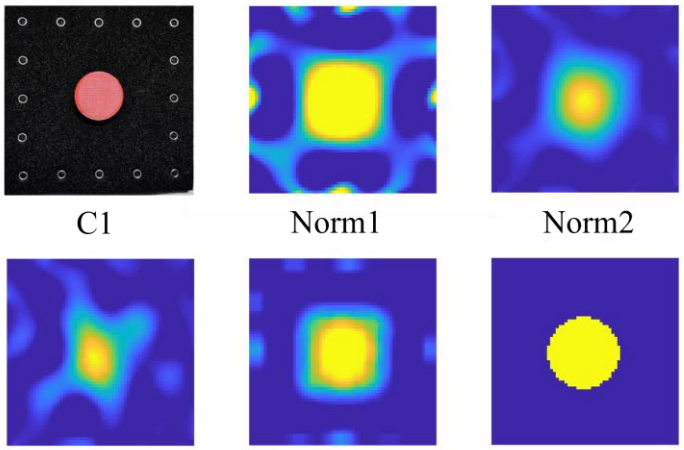
C1
Norm1
Norm2
Norm3
DWT
PSO

(a)

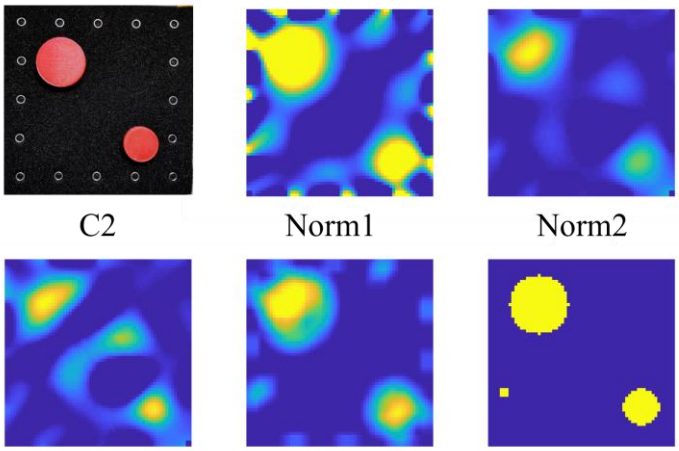
C2
Norm1
Norm2
Norm3
DWT
PSO

(b)

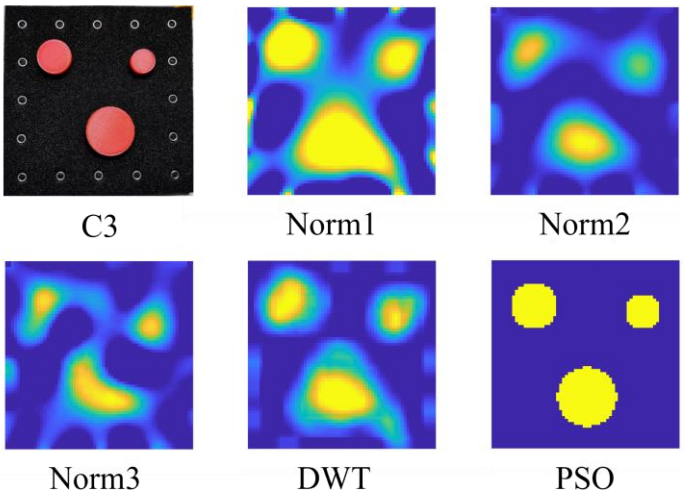
C3
Norm1
Norm2
Norm3
DWT
PSO

(c)

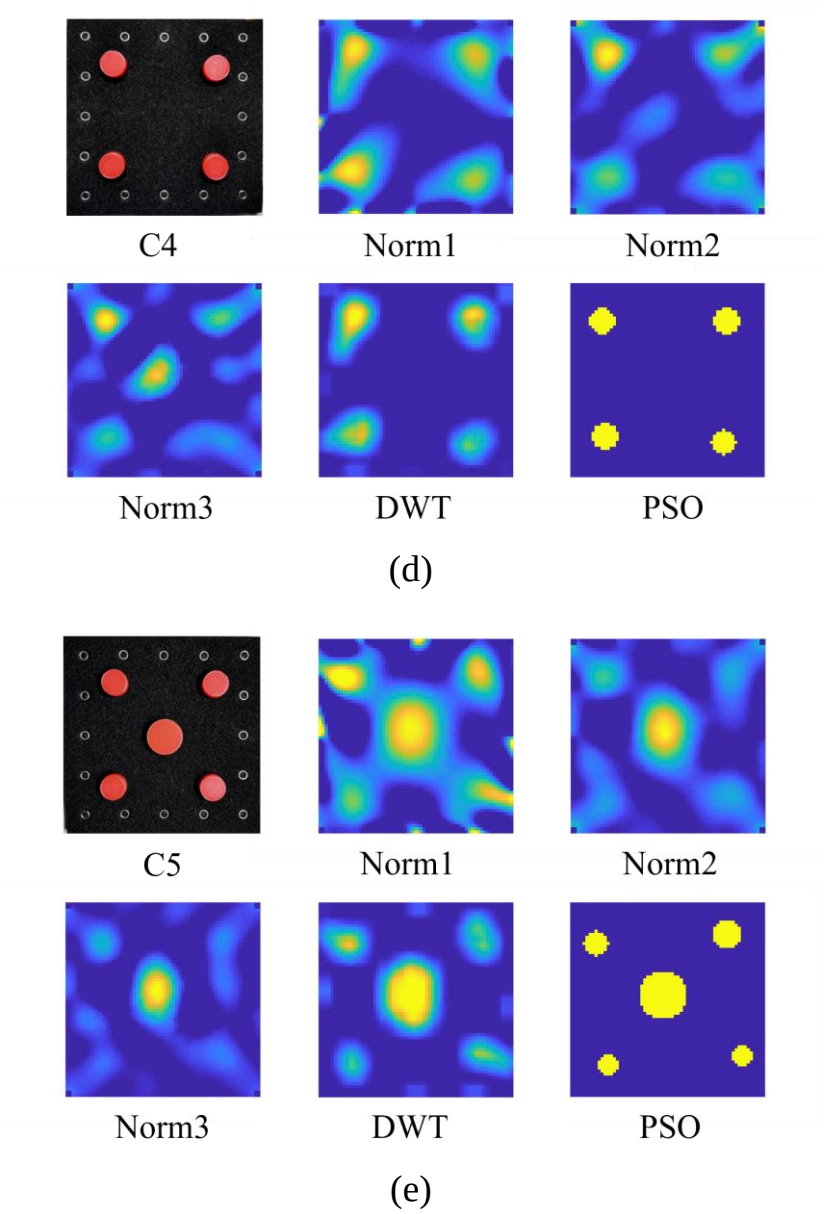

Figure 6.24: Reconstructed image of pressure mapping based on experimental data.

The correlation coefficients and image errors of the above images are listed in Table 6.5 and Table 6.6. Because ERT is ill-conditioned, a minor change in the voltage data can have a significant influence on the reconstructed image. As shown in Figure 6.24, the image obtained by just normalising the sensitivity matrix is severely distorted. In contrast, image fusion significantly reduces artefacts while pressure contours are enhanced. Compared with a single image, it has higher correlation coefficient and lower image error.

However, the quality of the image degrades as the number of targets in the pressure distribution increases.

Table 6.5: Comparison of correlation coefficients under five circular distributions.

Correlation Coefficient	C1	C2	C3	C4	C5
Norm 1	0.75	0.62	0.67	0.34	0.46
Norm 2	0.89	0.79	0.78	0.53	0.62
Norm 3	0.73	0.64	0.64	0.55	0.62
DWT	0.89	0.82	0.78	0.56	0.62
PSO	0.95	0.79	0.83	0.65	0.67

Table 6.6: Comparison of image errors under five circular distributions.

Image Error	C1	C2	C3	C4	C5
Norm 1	19%	23%	24%	24%	25%
Norm 2	13%	17%	20%	19%	22%
Norm 3	25%	30%	33%	28%	30%
DWT	14%	17%	21%	22%	23%
PSO	8%	18%	18%	18%	21%

The pressure distribution extracted by the PSO algorithm is highly consistent with the real distribution in terms of shape and position. Because this method is carried out based on Norm1, the accuracy of its extraction is directly related to the collected voltage. As shown in Figure 6.24 (e), the extracted pressure distribution deviates from the real position due to the image distortion of Norm1. This is because the measurement system used is limited in terms of accuracy and noise immunity. Thus, it is only used for method validation.

The PSO algorithm assumes that the targets are all circular, and so in addition to the circular pressure distribution, the ability to detect polygonal distributions is also discussed. Therefore, the triangular prism and the cuboid are selected as the objects for applying pressure, and the pressure mapping images obtained by the same method are shown in Figure 6.25. Table 6.7 and Table 6.8 are the calculated correlation coefficients and image errors.

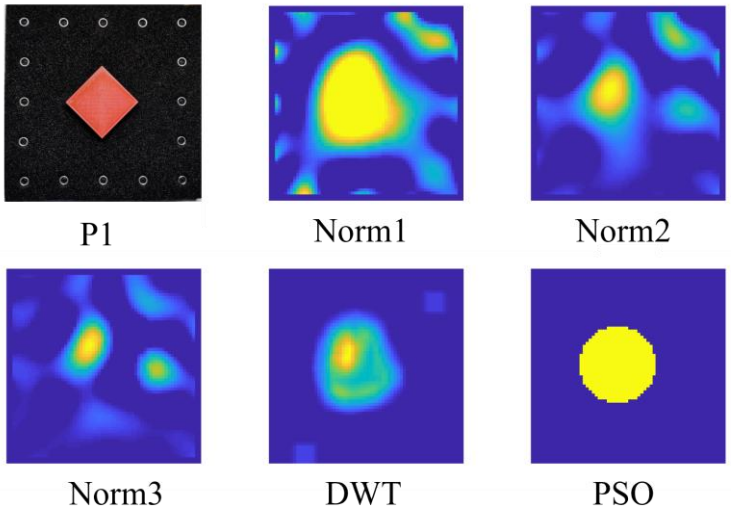
P1
Norm1
Norm2
Norm3
DWT
PSO

(a)

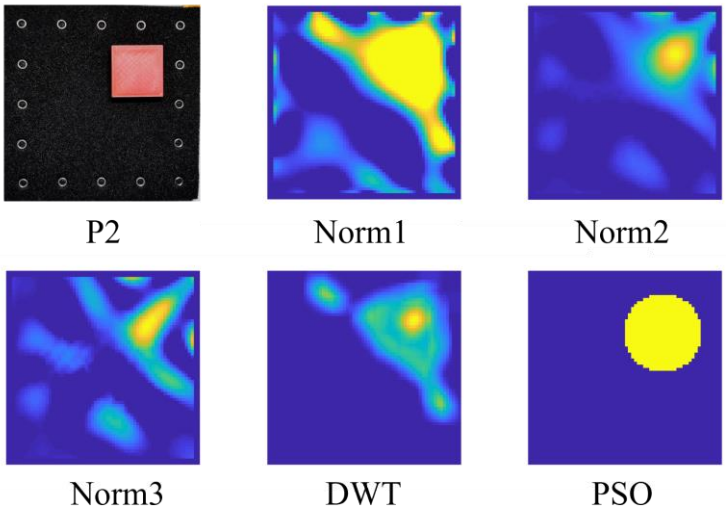
P2
Norm1
Norm2
Norm3
DWT
PSO

(b)

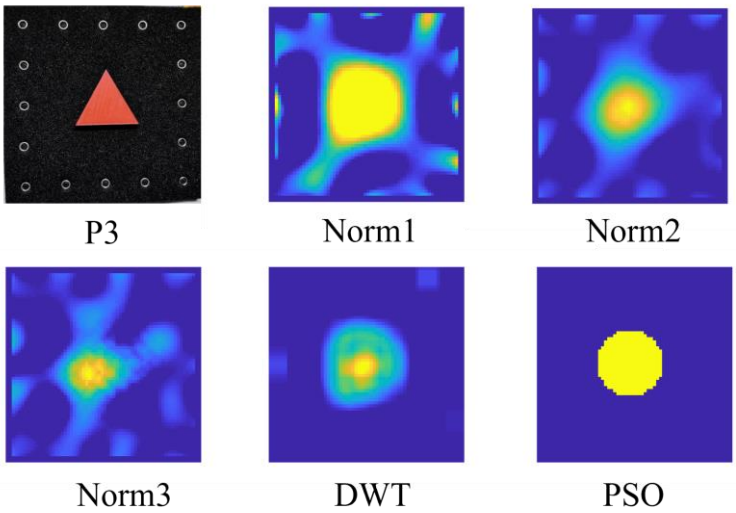
P3
Norm1
Norm2
Norm3
DWT
PSO

(c)

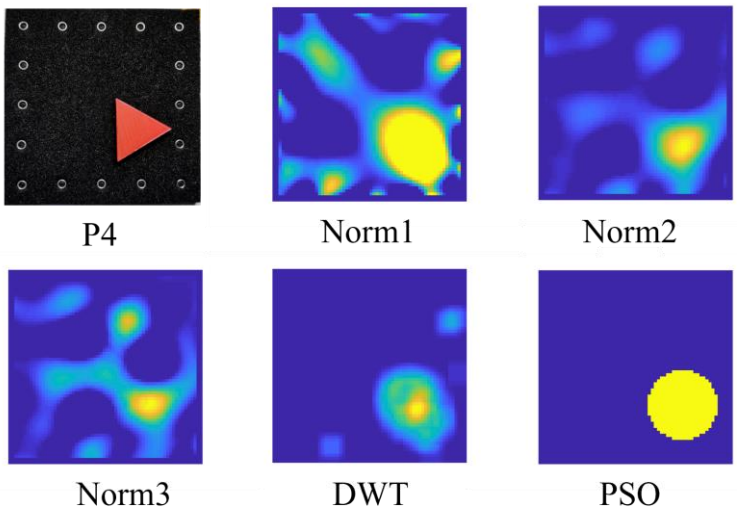

(d)

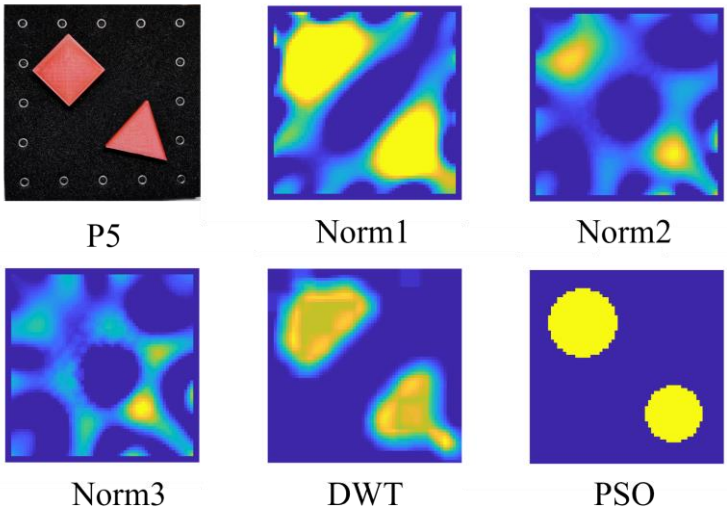

(e)

Figure 6.25: Image reconstruction of polygonal pressure distribution.

Table 6.7: Comparison of correlation coefficients under five polygonal distributions.

Correlation coefficient	P1	P2	P3	P4	P5
Norm 1	0.25	0.27	0.41	0.46	0.25
Norm 2	0.37	0.38	0.62	0.44	0.08
Norm 3	0.72	0.66	0.67	0.65	0.52
DWT	0.65	0.62	0.78	0.70	0.52
PSO	0.77	0.85	0.74	0.67	0.64

Table 6.8: Comparison of image errors under five polygonal distributions.

Image Error	P1	P2	P3	P4	P5
Norm 1	26%	26%	20%	20%	31%
Norm 2	24%	25%	17%	20%	32%
Norm 3	22%	26%	23%	22%	34%
DWT	21%	22%	16%	17%	29%
PSO	19%	15%	18%	22%	26%

The ERT sensor is unable to correctly detect the contours of the triangular and square pressure distributions. The edges and corners of polygons are blurred due to the soft-field nature of ERT, and so far there is no effective way to overcome this problem. However, the images obtained by DWT and PSO can reveal the general size and location of the pressure distribution. This provides a new solution to application scenarios that focus on the location of pressure distribution instead of pursuing high precision and high resolution.

6.6 Summary

The goal of this study is to combine ERT with flexible conductive materials as a potential method for large-area tactile sensing. However, the shortcomings of conventional ERTs in terms of resolution and real-time performance have become the biggest factors limiting their use in tactile sensing.

This chapter aims to improve the image quality of ERT-based tactile sensors. Firstly, the factors that lead to the distortion of the reconstructed image are systematically analysed. Image quality is affected by sensor design, measurement accuracy, and noise. It is verified by simulation that the linear approximation error between the conductivity change and the boundary voltage change is the main cause of the image distortion. In view of the low sensitivity of the central area of the sensor, it is suggested to use sensitivity matrix normalization combined with DWT image fusion to improve the accuracy of reconstructed images. This chapter uses weighted average rule and maximum absolute

value rule for DWT image fusion. Further research is needed on whether other fusion rules and image fusion methods can further improve the final image.

In addition, a target location method based on K-means clustering and a size estimation method based on PSO algorithm are respectively proposed. According to the simulation and experimental results, this method can quickly and accurately extract the location information of the target. The experimental results show that the relative size of the pressure distribution is revealed by the circular distribution, and the profile of the distribution other than the circular cannot be accurately detected. This is due to the consideration of real-time applications, because high-precision algorithms inevitably take a long time.

Compared with tactile sensor arrays, ERT as a non-invasive imaging technology avoids complicated wire connections and improves the overall flexibility of the sensor. In practical applications, ERT tactile sensing is disturbed by many external factors. However, with the improvement of hardware system and sensor manufacturing process, its unique sensing method is still an option for large-area tactile sensing.

Chapter 7 Conclusions and future work

7.1 Conclusions

This thesis is aimed at improving the performance of tactile sensors used in the fields of robots and human-computer interaction. In view of the unavoidable problems of tactile sensors in practical applications, some new optimisation strategies are proposed from the aspects of sensor structure and implementation methods.

Capacitive sensors have been widely used in tactile sensing due to high sensitivity, large dynamic measurement range and good dynamic response. A single-layer electrode capacitive tactile sensor is suggested here. Its structure is simpler than parallel plate capacitive sensor, so it has higher flexibility. Moreover, with flexible PCB as the substrate, it can provide a reliable electrical connection with external circuit. Besides the use of compressible and highly elastic materials, micro-structured dielectric layers are the most common solution to increasing the sensitivity and reducing hysteresis of capacitive tactile sensors. However, sensors with high sensitivity hardly have a large measurement range, which limits their practical applications. The dielectric layer with multi-sized micro-structure not only improves the sensor's sensitivity under low pressure, but also expands the measurement range so that the sensor still has measurable capacitance under high pressure. In addition to the dielectric layer, the influence of the structural parameters of the electrode and contact layers on sensor performance is investigated by simulation and experiment. With the improved dielectric layer structure, the sensor has a hysteresis error as low as 4.2% and a response time of 6.9 ms.

Based on the above optimisation of planar capacitive sensors, another novelty of this thesis is to propose a 3D force sensor design with only three interdigital electrodes. Inspired by the previous work, the microstructure of the dielectric layer was modified

according to the electrode sensitive area. As a result, the sensitivity of shear force is improved by 2-3 times. Although this is a design that can decouple the three-dimensional force using the minimum number of electrodes in theory, the serious nonlinearity of the sensor and the crosstalk between the three sensing units make it impossible to obtain the decoupled three-dimensional force directly. Therefore, it is expected to use neural network to decouple the contact force in the future work.

Considering the performance requirements and manufacturing costs of sensors in different application scenarios, this thesis provides two preparation strategies based on casting method, which are respectively applicable to high-sensitivity tactile sensors and large-scale sensor arrays. Different mould production methods have been adopted according to requirements, including silicon etching, 3D printing, and CNC machining. Unconstraint geometry is a benefit of 3D printed moulds, which also streamlines production and lowers costs. The size of the micro-structures, however, is limited by the precision of the 3D printer. Furthermore, even though the mould's surface has been hydrophobised, a portion of the dielectric layer still breaks when it is separated from the mould, indicating that more material preparation research is required.

For large-area tactile sensing, an 8×8 distributed tactile sensor array is designed, which is fabricated by FPCB. The microstructure of the dielectric layer adopts a truncated pyramid array to obtain sufficient stability. The influence of geometric parameters of the truncated pyramid on the measurement range and sensitivity of the sensor is quantified by simulation. Because the traditional contact layer has high requirements for the alignment of each layer, a universal contact layer with Y-shaped structure is proposed. Compared with other structures, the pressure applied through the Y-shaped contact layer is the most similar to the actual pressure distribution. In addition to tactile sensing, proximity sensing is a unique capability of planar capacitive sensors. Multi-channel capacitance

measurement system is used to evaluate the dual-function characteristics of tactile and proximity sensing of the sensor. By configuring the electrode combination, the dual modes of far-proximity sensing (up to 23mm) and near-proximity sensing (2-4mm) are realised on the same sensor.

Electrical resistance tomography has unique advantages over traditional tactile sensor arrays because there is no internal wire. For the problem of image distortion, the sensitivity distribution is improved by normalising the sensitivity matrix, especially in the central area. With image fusion based on discrete wavelet transform, accurate images are created by combining the features of different images. For the application of multi-contact targets, the feasibility of extracting target positions and estimating distribution sizes based on k-means clustering algorithm and PSO algorithm is validated. Despite not being appropriate for tactile imaging that requires high precision, this method is novel and instructive for implementing tactile sensing.

This thesis reviews the technological evolution of tactile sensors in recent years. In order to solve the problems in practical application and promote the mass production of the sensor, several aspects that need to be improved are put forward. The quantification of the influence of sensor structural parameters on the sensor's performance provides a reference for targeted sensor design. Three-dimensional force detection and dual function sensor arrays demonstrate the practical application of planar capacitive tactile sensors. Additionally, from an application perspective, the improvement and optimisation of image reconstruction algorithms make ERT a potential candidate for tactile sensing. Furthermore, the low-cost preparation method mentioned in this thesis can promote the mass production of sensors and accelerate the marketisation of tactile sensors.

7.2 Future work

Based on the conclusions drawn from this thesis, further research is required in following aspects:

For planar capacitive tactile sensors,

(1) The capacitive sensor assembled with uncured PDMS as an adhesive layer has poor stability and durability. Since the sensor's consistency cannot be guaranteed, it is challenging to use the sensor in delicate applications. Therefore, the preparation process of the sensor needs to be improved.

(2) Despite the use of a micro-structured dielectric layer, the dielectric properties of PDMS need to be improved. It is suggested that conductive particle doping can be used to prepare composite dielectric materials with large dielectric constants and large capacitance changes under pressure.

(3) Reducing the size of the electrodes can improve sensor resolution, but it reduces the initial capacitance of the sensing unit, which present a challenge for the capacitance acquisition system. The capacitance acquisition system developed in this research is only used to evaluate sensor performance. Therefore, the integration, stability, and anti-interference of the system must be improved before it can be used in practical applications.

For ERT-based tactile sensing,

(1) The development of flexible conductive materials with stable conductivity, good durability, and high longitudinal sensitivity needs to be investigated. If the conductivity of the material is anisotropic, then the conductivity of the material changes differently in response to mechanical stimuli in different directions. This

property can be used to determine the direction of mechanical stimuli (pressure or stretch).

(2) The improved imaging algorithm in Chapter 6 is only used for static tactile sensing, and dynamic tactile sensing is limited to the real-time performance of the ERT imaging algorithm. Furthermore, the connection of electrodes to flexible conductive materials should be considered to ensure a stable electrical connection under dynamic applications.

(3) This research is still in the laboratory stage. Applying the proposed sensor to the robot and collaborating with other sensors on the robot to complete complex operations will be of practical importance.

References

Abraira V E, & Ginty D D (2013), The sensory neurons of touch, *Neuron*, 79(4), 618-639.

Adler A, Gaggero P O, & Maimaitijiang Y (2011), Adjacent stimulation and measurement patterns considered harmful, *Physiological Measurement*, 32(7), 731.

Adnan R M, Parmar K S, Heddam S, Shahid S, & Kisi O (2021), Suspended sediment modeling using a heuristic regression method hybridized with kmeans clustering, *Sustainability*, 13 (9), 4648.

Abido M A (2002), Optimal design of power-system stabilizers using particle swarm optimization, *IEEE Trans. on Energy Conversion*, 17 (3), 406-413.

Alfadhel A, & Kosel J (2015), Magnetic nanocomposite cilia tactile sensor, *Advanced Materials*, 27(47), 7888-7892.

Alirezaei H, Nagakubo A, & Kuniyoshi Y (2009), A tactile distribution sensor which enables stable measurement under high and dynamic stretch, In *2009 IEEE Symposium on 3D User Interfaces*, Lafayette, LA, USA, 87-93.

Analog Devices (2007), Ultra-low power, 2-channel, capacitance converter for proximity sensing, *AD7150 Datasheet (Rev. A)*.

Bao P, Zhang L, & Wu X (2005), Canny edge detection enhancement by scale multiplication, *IEEE Trans. on Pattern Analysis and Machine Intelligence*, 27 (9), 1485-1490.

Barber D C, & Seagar A D (1987), Fast reconstruction of resistance images, *Clinical Physics and Physiological Measurement*, 8(4A), 47.

Bartolozzi C, Natale L, Nori F, & Metta G (2016), Robots with a sense of touch, *Nature materials*, 15(9), 921-925.

Bauer S, Bauer-Gogonea S, Graz I, Kaltenbrunner M, Keplinger C, & Schwödiauer R (2014), 25th anniversary article: a soft future: from robots and sensor skin to energy harvesters, *Advanced Materials*, 26(1), 149-162.

Begej S (1988), Fingertip-shaped optical tactile sensor for robotic applications, In *Proc. 1988 IEEE International Conference on Robotics and Automation*, Philadelphia, PA, USA, 1752-1757.

Bergström J S, & Boyce M C (2001), Constitutive modeling of the time-dependent and cyclic loading of elastomers and application to soft biological tissues, *Mechanics of Materials*, 33(9), 523-530.

Billard A, & Kragic D (2019), Trends and challenges in robot manipulation, *Science*, 364(6446).

Cai J H, Li J, Chen X D, & Wang M (2020), Multifunctional polydimethylsiloxane foam with multi-walled carbon nanotube and thermo-expandable microsphere for temperature

sensing, microwave shielding and piezoresistive sensor, *Chem. Eng. J.*, 393, 124805.

Cairone F, Gagliano S, Carbone D C, Recca G, & Bucolo M (2016), Micro-optofluidic switch realized by 3D printing technology, *Microfluidics and Nanofluidics*, 20(4), 1-10.

Chandra M, Ke S Y, Chen R, & Lo C Y (2017), Vertically stacked capacitive tactile sensor with more than quadrupled spatial resolution enhancement from planar arrangement, *Sensors and Actuators A: Physical*, 263, 386-390.

Chaple G N, Daruwala R D, & Gofane M S (2015), Comparisions of Robert, Prewitt, Sobel operator based edge detection methods for real time uses on FPGA, *Proc. of 2015 International Conference on Technologies for Sustainable Development*, Mumbai, India, 1-4.

Chen D, Cai Y, & Huang M C (2018), Customizable pressure sensor array: Design and evaluation, *IEEE Sensors J.*, 18(15), 6337-6344.

Chen T, Shi Q, Zhu M, He T, Sun L, Yang L, & Lee C (2018), Triboelectric self-powered wearable flexible patch as 3D motion control interface for robotic manipulator, *ACS Nano*, 12(11), 11561-11571.

Chen T Y, Wang Y C, Lo C Y, & Chen R (2013), Friction-assisted pulling force detection mechanism for tactile sensors, *J. of microelectromechanical systems*, 23(2), 471-481.

Chen X, Rogers J A, Lacour S P, Hu W, & Kim D H (2019), Materials chemistry in flexible electronics, *Chemical Society Reviews*, 48(6), 1431-1433.

Chen Y, Han Y, Yang W, & Li K (2019), A New Iterative Algorithm Based on Correction of Sensitivity Matrix for Electrical Resistance Tomography, *Mathematical Problems in Engineering*, Hindawi,1-15.

Chen Z, Li X, Wang J, Tao L, Long M, Liang S J, Ang L K, Shu C, Tsang H K, & Xu J B (2017), Synergistic effects of plasmonics and electron trapping in graphene short-wave infrared photodetectors with ultrahigh responsivity, *ACS Nano*, 11(1), 430-437.

Cheng W, Wang J, Ma Z, Yan K, Wang Y, Wang H, Li S, Li Y, Pan L, & Shi Y (2017), Flexible Pressure Sensor with High Sensitivity and Low Hysteresis based on a Hierarchically Micro-structured Electrode. *IEEE Electron Device Letter*, 39(2), 288-291.

Chi C, Sun X, Xue N, Li T, & Liu C (2018), Recent progress in technologies for tactile sensors, *Sensors*, 18(4), 948.

Chortos A, & Bao Z (2014), Skin-inspired electronic devices, *Materials Today*, 17(7), 321-331.

Chossat J B, Shin H S, Park Y L, & Duchaine V (2015), Soft tactile skin using an embedded ionic liquid and tomographic imaging, *J. of Mechanisms and Robotics*, 7(2), 021008.

Chuang S T, Chandra M, Chen R, & Lo C Y (2016), Capacitive tactile sensor with asymmetric electrodes for angle-detection-error alleviation, *Sensors and Actuators A: Physical*, 250, 159-169.

Cui Z Q, Wang Q, Xue Q, Fan W R, Zhang L L, Cao Z, Sun B Y, Wang H X, and Yang W Q (2016), A review on image reconstruction algorithms for electrical capacitance/resistance tomography, *Sensor Review*, 36 (4), 429-445.

Dahiya R S, Metta G, Valle M, & Sandini G (2009), Tactile sensing—from humans to humanoids, *IEEE Trans. on Robotics*, 26(1), 1-20.

de Lima C R, Mello L A, Lima R G, & Silva E C (2007), Electrical impedance tomography through constrained sequential linear programming: a topology optimization approach, *Meas. Sci. Technol.*, 18 (9), 2847.

Dobrzynska J A, & Gijs M A (2012), Flexible polyimide-based force sensor, *Sensors and Actuators A: Physical*, 173(1), 127-135.

Fan F R, Lin L, Zhu G, Wu W, Zhang R, & Wang Z L (2012), Transparent triboelectric nanogenerators and self-powered pressure sensors based on micropatterned plastic films, *Nano Letters*, 12(6), 3109-3114.

Fan F R, Luo J, Tang W, Li C, Zhang C, Tian Z, & Wang Z L (2014), Highly transparent and flexible triboelectric nanogenerators: performance improvements and fundamental mechanisms, *J. of Materials Chemistry A*, 2(33), 13219-13225.

Fang B, Chen Y, Sun F, Yang D, Zhang X, Xia Z, & Liu H (2020), A petal-array capacitive tactile sensor with micro-pin for robotic fingertip sensing, In *2020 3rd IEEE International Conference on Soft Robotics (RoboSoft)*, New Haven, CT, USA, 452-457.

Fulton W S, & Lipczynski R T (1993), Body-support pressure measurement using electrical impedance tomography, In Proceedings of *the 15th Annual International Conference of the IEEE Eng. in Medicine and Biology Societ*, San Diego, CA, USA, 98-99.

Gao Y, Ota H, Schaler E W, Chen K, Zhao A, Gao W, Fahad H M, Leng Y, Zheng A, Xiong F, Zhang C, Tai L C, Zhao P, Fearing R S, & Javey A (2017), Wearable microfluidic diaphragm pressure sensor for health and tactile touch monitoring, *Advanced Materials*, 29(39), 1701985.

Guo S Z, Qiu K, Meng F, Park S H, & McAlpine M C (2017), 3D printed stretchable tactile sensors, *Advanced Materials*, 29(27), 1701218.

Ha M, Lim S, Park J, Um D S, Lee Y, & Ko H (2015), Bioinspired interlocked and hierarchical design of ZnO nanowire arrays for static and dynamic pressure-sensitive electronic skins, *Advanced Functional Materials*, 25(19), 2841-2849.

Hammock M L, Chortos A, Tee B C K, Tok J B H, & Bao Z (2013), 25th anniversary article: the evolution of electronic skin (e-skin): a brief history, design considerations, and recent progress, *Advanced Materials*, 25(42), 5997-6038.

Han T, Kundu S, Nag A, & Xu Y (2019), 3D printed sensors for biomedical applications: a review, *Sensors*, 19(7), 1706.

Harmon L D (1982), Automated tactile sensing, *The International J. of Robotics Research*, 1(2), 3-32.

Hillis W D (1982), A high-resolution imaging touch sensor, *The International J. of Robotics Research*, 1(2), 33-44.

Howe R D (1993), Tactile sensing and control of robotic manipulation, *Advanced Robotics*, 8(3), 245-261.

Hu X, & Yang W (2010), Planar capacitive sensors–designs and applications, *Sensor Review*, 30(1), 24-39.

Huang C N, Yu F M, & Chung H Y (2007), Rotational electrical impedance tomography, *Meas. Sci. Technol.*, 18(9), 2958.

Huang Y, Fan X, Chen S C, & Zhao N (2019), Emerging technologies of flexible pressure sensors: materials, modeling, devices, and manufacturing, *Advanced Functional Materials*, 29(12), 1808509.

Huang Y, Yuan H, Kan W, Guo X, Liu C, & Liu P (2017), A flexible three-axial capacitive tactile sensor with multilayered dielectric for artificial skin applications, *Microsystem Technologies*, 23(6), 1847-1852.

Igreja R, & Dias C J (2004), Analytical evaluation of the interdigital electrodes capacitance for a multi-layered structure, *Sensors and Actuators A: Physical*, 112(2-3), 291-301.

Jamali N, & Sammut C (2010), Material classification by tactile sensing using surface textures, In *2010 IEEE International Conference on Robotics and Automation*, Anchorage, AK, USA, 2336-2341.

Jason N N, Ho M D, & Cheng W (2017), Resistive electronic skin, *J. of Materials Chemistry C*, 5(24), 5845-5866.

Jiang J, Tu S, Fu R, Li J, Hu F, Yan B, Gu Y, & Chen S (2020), Flexible piezoelectric pressure tactile sensor based on electrospun BaTiO3/poly (vinylidene fluoride) nanocomposite membrane, *ACS Applied Materials & Interfaces*, 12(30), 33989-33998.

Kato Y, Mukai T, Hayakawa T, & Shibata T (2007), Tactile sensor without wire and sensing element in the tactile region based on EIT method, In *Sensors, 2007 IEEE*, Atlanta, GA, USA, 792-795.

Kennedy J, & Eberhart R (1995), Particle swarm optimization, In *Proc. of ICNN'95-International Conference on Neural Networks*, Perth, WA, Australia, 4, 1942-1948.

Khosravani M R, & Reinicke T (2020), 3D-printed sensors: Current progress and future challenges, *Sensors and Actuators A: Physical*, 305, 111916.

Kim T K, Kim J K, & Jeong O C (2011), Measurement of nonlinear mechanical properties of PDMS elastomer, *Microelectronic Eng.*, 88(8), 1982-1985.

Kumar V S, & Krishnamoorthi C (2021), Development of electrical transduction based wearable tactile sensors for human vital signs monitor: Fundamentals, methodologies and applications, *Sensors and Actuators A: Physical*, 321, 112582.

Kwon D, Lee T I, Shim J, Ryu S, Kim M S, Kim S, Kim T S, & Park I (2016), Highly

sensitive, flexible, and wearable pressure sensor based on a giant piezocapacitive effect of three-dimensional microporous elastomeric dielectric layer, *ACS Applied Materials & Interfaces*, 8(26), 16922-16931.

Lee H K, Chung J, Chang S I, & Yoon E (2008), Normal and shear force measurement using a flexible polymer tactile sensor with embedded multiple capacitors, *J. of Microelectromechanical Systems*, 17(4), 934-942.

Lee H K, Chung J, Chang S I, & Yoon E (2011), Real-time measurement of the three-axis contact force distribution using a flexible capacitive polymer tactile sensor, *J. of Micromechanics and Microengineering*, 21(3), 035010.

Lee J, Kwon H, Seo J, Shin S, Koo J H, Pang C, Son S, Kim J H, Jang Y H, Kim D E, & Lee T (2015), Conductive fiber-based ultrasensitive textile pressure sensor for wearable electronics, *Advanced Materials*, 27(15), 2433-2439.

Lee Y, Park J, Cho S, Shin Y E, Lee H, Kim J, Myoung J, Cho S, Kang S, Baig C, & Ko H (2018), Flexible ferroelectric sensors with ultrahigh pressure sensitivity and linear response over exceptionally broad pressure range, *ACS Nano*, 12(4), 4045-4054.

Li T, Luo H, Qin L, Wang X, Xiong Z, Ding H, Gu Y, Liu Z, & Zhang T (2016), Flexible capacitive tactile sensor based on micropatterned dielectric layer, *Small*, 12(36), 5042-5048.

Li X, Xu C, Wang C, Shao J, Chen X, Wang C, Tian H, Wang Y, Yang Q, Wang L, Lu B (2017), Improved triboelectrification effect by bendable and slidable fish-scale-like microstructures, *Nano Energy*, 40, 646-654.

Li X B, Larson S D, Zyuzin A S, & Mamishev A V (2006), Design principles for multichannel fringing electric field sensors, *IEEE Sensors J.*, 6(2), 434-440.

Li X B, Larson S D, Zyuzin A S, & Mamishev A V (2004), Design of multichannel fringing electric field sensors for imaging. Part I. General design principles, In *Conference Record of the 2004 IEEE International Symposium on Electrical Insulation*, Indianapolis, USA, 406-409.

Li Y, Wang B, Li Y, Zhang B, Weng L, Huang W, & Liu H (2018), Design and output characteristics of magnetostrictive tactile sensor for detecting force and stiffness of manipulated objects, *IEEE Trans. on Industrial Informatics*, 15(2), 1219-1225.

Liang G, Wang Y, Mei D, Xi K, & Chen Z (2015), Flexible capacitive tactile sensor array with truncated pyramids as dielectric layer for three-axis force measurement, *J. of Microelectromechanical Systems*, 24(5), 1510-1519.

Lin L, Xie Y, Wang S, Wu W, Niu S, Wen X, & Wang Z L (2013), Triboelectric active sensor array for self-powered static and dynamic pressure detection and tactile imaging, *ACS Nano*, 7(9), 8266-8274.

Liu C, Huang N, Xu F, Tong J, Chen Z, Gui X, Fu Y, & Lao C (2018), 3D printing technologies for flexible tactile sensors toward wearable electronics and electronic skin, *Polymers*, 10(6), 629.

Liu W, Liu N, Yue Y, Rao J, Cheng F, Su J, Liu Z & Gao Y (2018), Piezoresistive pressure

sensor based on synergistical innerconnect polyvinyl alcohol nanowires/wrinkled graphene film, *Small*, 14(15), 1704149.

Liu W, Yu P, Gu C, Cheng X, & Fu X (2017), *Fingertip piezoelectric tactile sensor array for roughness encoding under varying scanning velocity*, *IEEE Sensors J*., 17(21), 6867-6879.

Liu X, Tang C, Du X, Xiong S, Xi S, Liu Y, Shen X, Zheng Q, Wang Z, Wu Y, Horner A, & Kim J K (2017), A highly sensitive graphene woven fabric strain sensor for wearable wireless musical instruments, *Materials Horizons*, 4(3), 477-486.

Luo N, Dai W, Li C, Zhou Z, Lu L, Poon C C, Chen S, Zhang Y, & Zhao N (2016), Flexible piezoresistive sensor patch enabling ultralow power cuffless blood pressure measurement, *Advanced Functional Materials*, 26(8), 1178-1187.

Luo S, Bimbo J, Dahiya R, & Liu H (2017), Robotic tactile perception of object properties: A review, *Mechatronics*, 48, 54-67.

Luo S, Yang J, Song X, Zhou X, Yu L, Sun T, Yu C, Huang D, Du C, & Wei D (2018), Tunable-sensitivity flexible pressure sensor based on graphene transparent electrode, *Solid-State Electronics*, 145, 29-33.

Luo Y, Shao J, Chen S, Chen X, Tian H, Li X, Wang L, Wang D, & Lu B (2019), Flexible capacitive pressure sensor enhanced by tilted micropillar arrays, *ACS Applied Materials & Interfaces*, 11(19), 17796-17803.

Lü X, Bao W, Wang S, Tao Y, Yang J, Jiang L, Jiang J, Li X, Xie X, & Chen R (2017), Three-dimensional interfacial stress decoupling method for rehabilitation therapy robot, *IEEE Trans. on Industrial Electronics*, 64(5), 3970-3977.

Ly H H, Tanaka Y, Fukuda T, & Sano A (2017), Grasper having tactile sensing function using acoustic reflection for laparoscopic surgery, *International J. of Computer Assisted Radiology and Surgery*, 12(8), 1333-1343.

Mannsfeld S C, Tee B C, Stoltenberg R M, Chen C V, Barman S, Muir B V, Sokolov A N, Reese C, & Bao Z (2010), Highly sensitive flexible pressure sensors with microstructured rubber dielectric layers, *Nature Materials*, 9(10), 859-864.

Mazlan N S, Ramli M M, Abdullah M M A B, Halin D C, Isa S M, Talip L F A, Dania N S, & Murad S A Z (2017), Interdigitated electrodes as impedance and capacitance biosensors: A review, In *AIP Conference Proceedings* ,1885(1), 1-8.

Nagakubo A, Alirezaei H, & Kuniyoshi Y (2007), A deformable and deformation sensitive tactile distribution sensor, In *2007 IEEE International Conference on Robotics and Biomimetics (ROBIO)*, Sanya, China, 1301-1308.

Nelson T, Jin S, Hackwood S, & Beni G (1986), Shear-sensitive magnetoresistive robotic tactile sensor, *IEEE Trans. on Magnetics*, 22(5), 394-396.

Nghiem B T, Sando I C, Gillespie R B, McLaughlin B L, Gerling G J, Langhals N B, Urbanchek M G, & Cederna P S (2015), Providing a sense of touch to prosthetic hands, *Plastic and Reconstructive Surgery*, 135(6), 1652-1663.

Osullivan S, Nagle R, McEwen J A, & Casey V (2003), Elastomer rubbers as deflection elements in pressure sensors: investigation of properties using a custom designed programmable elastomer test rig, *J. of Physics D: Applied Physics*, 36(15), 1910.

Pajares G, & De La Cruz J M (2004), A wavelet-based image fusion tutorial, *Pattern Recognition*, 37 (9), 1855-1872.

Park J, Lee Y, Hong J, Ha M, Jung Y D, Lim H, Kim S, & Ko H (2014), Giant tunneling piezoresistance of composite elastomers with interlocked microdome arrays for ultrasensitive and multimodal electronic skins, *ACS Nano*, 8(5), 4689-4697.

Pierre Claver U, & Zhao G (2021), Recent progress in flexible pressure sensors based electronic skin, *Advanced Engineering Materials*, 23(5), 2001187.

Psarski M, Marczak J, Celichowski G, Sobieraj G B, Gumowski K, Zhou F, & Liu W (2012), Hydrophobization of epoxy nanocomposite surface with 1H, 1H, 2H, 2H-perfluorooctyltrichlorosilane for superhydrophobic properties, *Central European J. of Physics*, 10(5), 1197-1201.

Qiu J, Guo X, Chu R, Wang S, Zeng W, Qu L, Zhao Y, Yan F, & Xing G (2019), Rapid-response, low detection limit, and high-sensitivity capacitive flexible tactile sensor based on three-dimensional porous dielectric layer for wearable electronic skin, *ACS Applied Materials & Interfaces*, 11(43), 40716-40725.

Qiu Z, Wan Y, Zhou W, Yang J, Yang J, Huang J, Zhang J, Liu Q, Huang S, Bai N, Wu Z, Hong W, Wang H, & Guo C F (2018), Ionic skin with biomimetic dielectric layer templated from calathea zebrine leaf, *Advanced Functional Materials*, 28(37), 1802343.

Ramadan K S, Sameoto D, & Evoy S (2014), A review of piezoelectric polymers as functional materials for electromechanical transducers, *Smart Materials and Structures*, 23(3), 033001.

Ramalingame R, Hu Z, Gerlach C, Rajendran D, Zubkova T, Baumann R, & Kanoun O (2019), Flexible piezoresistive sensor matrix based on a carbon nanotube PDMS composite for dynamic pressure distribution measurement, *J. of Sensors and Sensor Systems*, 8(1), 1-7.

Ren Z, Nie J, Shao J, Lai Q, Wang L, Chen J, Chen X, & Wang Z L (2018), Fully elastic and metal-free tactile sensors for detecting both normal and tangential forces based on triboelectric nanogenerators, *Advanced Functional Materials*, 28(31), 1802989.

Rodriguez-Frias M A and Yang W (2020), Dual-Modality 4-Terminal Electrical Capacitance and Resistance Tomography for Multiphase Flow Monitoring, *IEEE Sensors J.*, 20(6),3217–3225.

Ruth S R A, Feig V R, Tran H, & Bao Z (2020), Microengineering pressure sensor active layers for improved performance, *Advanced Functional Materials*, 30(39), 2003491.

Saccomandi P, Schena E, Oddo C M, Zollo L, Silvestri S, & Guglielmelli E (2014), Microfabricated tactile sensors for biomedical applications: a review, *Biosensors*, 4(4), 422-448.

Sferrazza C, & D'Andrea R (2022), Sim-to-real for high-resolution optical tactile sensing: From images to three-dimensional contact force distributions, *Soft Robotics*, 9(5), 926-937.

Shi R, Lou Z, Chen S, & Shen G (2018), Flexible and transparent capacitive pressure sensor with patterned microstructured composite rubber dielectric for wearable touch keyboard application, *Science China Materials*, 61(12), 1587-1595.

Shi Y (2004), Particle swarm optimization, *IEEE Connections*, 2 (1), 8-13.

Shirafuji S, & Hosoda K (2014), Detection and prevention of slip using sensors with different properties embedded in elastic artificial skin on the basis of previous experience, *Robotics and Autonomous Systems*, 62(1), 46-52.

Shuai X, Zhu P, Zeng W, Hu Y, Liang X, Zhang Y, Sun R, & Wong C P (2017), Highly sensitive flexible pressure sensor based on silver nanowires-embedded polydimethylsiloxane electrode with microarray structure, *ACS Applied Materials & Interfaces*, 9(31), 26314-26324.

Silvera Tawil D, Rye D, & Velonaki M (2012), Interpretation of the modality of touch on an artificial arm covered with an EIT-based sensitive skin, *The International J. of Robotics Research*, 31(13), 1627-1641.

Silvera-Tawil D, Rye D, & Velonaki M (2015), Artificial skin and tactile sensing for socially interactive robots: A review, *Robotics and Autonomous Systems*, 63, 230-243.

Smith J, White T, Dodge C, Paradiso J, Gershenfeld N, & Allport D (1998), Electric field sensing for graphical interfaces, *IEEE Computer Graphics and Applications*, 18(3), 54-60.

Sundaram S, Kellnhofer P, Li Y, Zhu J Y, Torralba A, & Matusik W (2019), Learning the signatures of the human grasp using a scalable tactile glove, *Nature*, 569, 698-702.

Surapaneni R, Park K, Suster M A, Young D J, & Mastrangelo C H (2011), A highly sensitive flexible pressure and shear sensor array for measurement of ground reactions in pedestrian navigation, In *2011 16th IEEE International Solid-State Sensors, Actuators and Microsystems Conference*, Beijing, China, 906-909.

Tang M, Wang W, Wheeler J, McCormick M, & Dong X (2002), The number of electrodes and basis functions in EIT image reconstruction, *Physiological Measurement*, 23(1), 129.

Tawil D S, Rye D, & Velonaki M (2011), Improved image reconstruction for an EIT-based sensitive skin with multiple internal electrodes, *IEEE Trans. on Robotics*, 27(3), 425-435.

Tee B C K, Chortos A, Dunn R R, Schwartz G, Eason E, & Bao Z (2014), Tunable flexible pressure sensors using microstructured elastomer geometries for intuitive electronics, *Advanced Functional Materials*, 24(34), 5427-5434.

Tee B C K, Chortos A, Berndt A, Nguyen A K, Tom A, McGuire A, Lin Z C, Tien K, Bae W G, Wang H, Mei P, Chou H H, Cui B, Deisseroth K, NG T N, & Bao Z (2015), A skin-inspired organic digital mechanoreceptor, *Science*, 350(6258), 313-316.

Texas Instruments (2003), Single-Pole Double-Throw Analog Switch, *SN74LVC1G3157 Datasheet (Rev. M)*.

Tofail S A, Koumoulos E P, Bandyopadhyay A, Bose S, O'Donoghue L, & Charitidis C (2018), Additive manufacturing: scientific and technological challenges, market uptake and opportunities, *Materials Today*, 21(1), 22-37.

Wajman R, Mazurkiewicz L, & Sankowski D (2004), The sensitivity map in the image reconstruction process for electrical capacitance tomography, *Proc. of the 3rd International Symposium on Process Tomography in Poland*, 165.

Wan Y, Qiu Z, Huang J, Yang J, Wang Q, Lu P, Yang J, Zhang J, Huang S, Wu Z, & Guo C F (2018), Natural plant materials as dielectric layer for highly sensitive flexible electronic skin, *Small*, 14(35), 1801657.

Wang J, Jiu J, Nogi M, Sugahara T, Nagao S, Koga H, He P, & Suganuma K (2015), A highly sensitive and flexible pressure sensor with electrodes and elastomeric interlayer containing silver nanowires, *Nanoscale*, 7(7), 2926-2932.

Wang S, Oh J Y, Xu J, Tran H, & Bao Z (2018), Skin-inspired electronics: an emerging paradigm, *Accounts of Chemical Research*, 51(5), 1033-1045.

Wang S, Xu J, Wang W, Wang G J N, Rastak R, Molina-Lopez F, Chung J W, Niu S, Feig V R, Lopez J, Lei T, Kwon S K, Kim Y, Foudeh A M, Ehrlich A, Gasperini A, Yun Y, Murmann B, Tok J B H, & Bao Z (2018), Skin electronics from scalable fabrication of an intrinsically stretchable transistor array, *Nature*, 555, 83-88.

Wang X, Dong L, Zhang H, Yu R, Pan C, & Wang Z L (2015), Recent progress in electronic skin, *Advanced Science*, 2(10), 1500169.

Wang X, Gu Y, Xiong Z, Cui Z, & Zhang T (2014), Silk-molded flexible, ultrasensitive, and highly stable electronic skin for monitoring human physiological signals, *Advanced Materials*, 26(9), 1336-1342.

Wang Y, Chen J, & Mei D (2019), Flexible tactile sensor array for slippage and grooved surface recognition in sliding movement, *Micromachines*, 10(9), 579.

Wang Z, Volinsky A A, & Gallant N D (2015), Nanoindentation study of polydimethylsiloxane elastic modulus using B erkovich and flat punch tips, *J. of Applied Polymer Science*, 132(5).

Wang Z L (2020), Triboelectric nanogenerator (TENG)—sparking an energy and sensor revolution, *Advanced Energy Materials*, 10(17), 2000137.

Weiss K, & Worn H (2005), The working principle of resistive tactile sensor cells, *IEEE International Conference Mechatronics and Automation*, Niagara Falls, Canada, 471-476

Wu C, Wang A C, Ding W, Guo H, & Wang Z L (2019), Triboelectric nanogenerator: a foundation of the energy for the new era, *Advanced Energy Materials*, 9(1), 1802906.

Xia F, Campi F, & Bahreyni B (2018), Tri-mode capacitive proximity detection towards improved safety in industrial robotics, *IEEE Sensors J.*, 18(12), 5058-5066.

Xiang K, Huang G, Zheng J, Wang X, & Huang J (2012), Accelerated thermal ageing studies of polydimethylsiloxane (PDMS) rubber, *J. of Polymer Research*, 19(5), 1-7.

Yamazaki H, Nishiyama M, Watanabe K, & Sokolov M (2016), Tactile sensing for object identification based on hetero-core fiber optics, *Sensors and Actuators A: Physical*, 247, 98-104.

Yang C, Jing X, Wang F, Ehmann K F, Tian Y, & Pu Z (2019), Fabrication of controllable wettability of crystalline silicon surfaces by laser surface texturing and silanization, *Applied Surface Science*, 497, 143805.

Yang G Z, Bellingham J, Dupont P E, Fischer P, Floridi L, Full R, Jacobstein N, Kumar V, Mcnutt M, Merrifield R, Nelson B J, Scassellati B, Taddeo M, Taylor R, Veloso M, Wang Z L & Wood R (2018), The grand challenges of Science Robotics, *Science robotics*, 3(14).

Yang J C, Kim J O, Oh J, Kwon S Y, Sim J Y, Kim D W, Choi H B, & Park S (2019), Microstructured porous pyramid-based ultrahigh sensitive pressure sensor insensitive to strain and temperature, *ACS Applied Materials & Interfaces*, 11(21), 19472-19480.

Yang J C, Mun J, Kwon S Y, Park S, Bao Z, & Park S (2019), Electronic skin: recent progress and future prospects for skin-attachable devices for health monitoring, robotics, and prosthetics, *Advanced Materials*, 31(48), 1904765.

Yang T, Xie D, Li Z, & Zhu H (2017), Recent advances in wearable tactile sensors: Materials, sensing mechanisms, and device performance, *Materials Science and Engineering: R: Reports*, 115, 1-37.

Yang W Q, & Peng L (2002), Image reconstruction algorithms for electrical capacitance tomography, *Measurement science and technology*, 14(1).

Yao G, Xu L, Cheng X, Li Y, Huang X, Guo W, Liu S, Wang Z L, & Wu H (2020), Bioinspired triboelectric nanogenerators as self-powered electronic skin for robotic tactile sensing, *Advanced Functional Materials*, 30(6), 1907312.

Yao T, Guo X, Li C, Qi H, Lin H, Liu L, Dai Y, Qu L, Huang Z, Liu P, Liu C, Huang Y, & Xing G (2020), Highly sensitive capacitive flexible 3D-force tactile sensors for robotic grasping and manipulation, *J. of Physics D: Applied Physics*, 53(44), 445109.

Yu P, Liu W, Gu C, Cheng X, & Fu X (2016), Flexible piezoelectric tactile sensor array for dynamic three-axis force measurement, *Sensors*, 16(6), 819.

Zhai Y, Yu Y, Zhou K, Yun Z, Huang W, Liu H, Xia Q, Dai K, Zheng G, Liu C, & Shen C (2020), Flexible and wearable carbon black/thermoplastic polyurethane foam with a pinnate-veined aligned porous structure for multifunctional piezoresistive sensors, *Chem. Eng. J.*, 382, 122985.

Zhang L (2013), A modified landweber iteration algorithm using updated sensitivity matrix for electrical impedance tomography, *International J. of Advanced Pervasive and Ubiquitous Computing*, 5 (1), 17-29.

Zhang Q, Jia W, Ji C, Pei Z, Jing Z, Cheng Y, Zhang W, Zhuo K, Ji J, Yuan Z, Sang S (2019), Flexible wide-range capacitive pressure sensor using micropore PE tape as template, *Smart Materials and Structures*, 28(11), 115040.

Zhang T, Jiang L, Wu X, Feng W, Zhou D, & Liu H (2014), Fingertip three-axis tactile

sensor for multifingered grasping, *IEEE/ASME Trans. on Mechatronics*, 20(4), 1875-1885.

Zhou Q, Ji B, Wei Y, Hu B, Gao Y, Xu Q, Zhou J, & Zhou B (2019), A bio-inspired cilia array as the dielectric layer for flexible capacitive pressure sensors with high sensitivity and a broad detection range, *J. of Materials Chemistry A*, 7(48), 27334-27346.

Zhu M, Lou M, Yu J, Li Z, & Ding B (2020), Energy autonomous hybrid electronic skin with multi-modal sensing capabilities, *Nano Energy*, 78, 105208.

Zhu Y, Jiang S, Xiao Y, Yu J, Sun L, & Zhang W (2018), A flexible three-dimensional force sensor based on PI piezoresistive film, *J. of Materials Science: Materials in Electronics*, 29(23), 19830-19839.

Zhuo B, Chen S, Zhao M, & Guo X (2017), High sensitivity flexible capacitive pressure sensor using polydimethylsiloxane elastomer dielectric layer micro-structured by 3-D printed mould, *IEEE J. of the Electron Devices Society*, 5(3), 219-223.